Faculté des bioingénieurs

Impact Assessment of Land Cover, Urban Morphology, and Roofing Materials on Surface Urban Heat Island Estimation Using Multi-Temporal Landsat Imagery in Tegal City, Indonesia

Author : Azrina Farania

Promoteur(s) : Prof. Pierre Defourny (UCLouvain)
Dr. Julien Radoux (UCLouvain)

Lecteur(s) : Dr. Sophie Bontemps (UCLouvain)
Dr. Mait Lang (University of Tartu)

Année académique 2025-2026

Mémoire de fin d'études présenté en vue de l'obtention du diplôme de Master: SAIV - MSc Erasmus+ GEM : Geo-Information Science and Earth Observation for Environmental Modelling and Management

Acknowledgements

First and foremost, I would like to thank Dr. Julien Radoux and Prof. Pierre Defourny for their excellent guidance and support throughout this thesis. Thanks for pushing me to do better work. I am grateful to the Tegal City Government for providing valuable data, as well as a place to learn and contribute to my community. Big thanks to all the professors and lecturers at UCLouvain and University of Tartu who built my foundation in GIS and Remote Sensing. I am also grateful to my GEM colleagues for making this journey enjoyable and to my family for their unwavering support. Finally, thanks to the European Education and Culture Executive Agency for funding the GEM program and making this opportunity possible.

The student's contribution to this work

Stage	**Azrina Farania**	**Prof. Pierre Defourny & Dr. Julien Radoux**	**Artificial Intelligence (AI)**
Conceptualisation	X	X (suggesting research direction)	
Methodology	X	X (suggesting analysis method)	
Investigation	X		
Formal analysis	X	X (correcting analysis technique and result)	X (Claude Sonnet 4.6 and Gemini 2.0 (Python code structure and debugging))
Validation	X		
Writing – original draft	X		
Writing – review & editing	X	X (reviewing)	X (Claude Sonnet 4.6 and Grammarly (paragraph restructuring, and grammar checking)
Visualisation	X		
Supervision	X		

In the conceptualization stage, the main research idea for estimating SUHI in Tegal City was developed by the student, with the professors suggesting the overall research direction and the theoretical background to be checked. In methodology, the student designed the full research workflow, while the land cover updating method, the PSF approach, and the impact assessment analysis were suggested by the professors. Additionally, in the formal analysis stage, professors corrected the analysis technique and reviewed the results. AI content provided advice on corrections. No text or image generation was used. All content was reviewed by the author and assumes full responsibility for the content of this thesis.

Table of Contents

Table of Figures

Table of Tables

List of Acronyms

AcATaMa: Accuracy Assessment for Thematic Maps
API: Application Programming Interface
ASTER: Advanced Spaceborne Thermal
AUHI: Atmospheric Urban Heat Island
Emission and Reflection Radiometer
BSF: Building Surface Fraction
BSI: Bare Soil Index
ECMWF: European Centre for Medium-Range Weather Forecasts
ISF: Impervious Surface Fraction
LANDARTs: Landsat Automatic Retrieval of Ts (Surface Temperature)
LCZs: Local Climate Zones
LSE: Land Surface Emissivity
LST: Land Surface Temperature
MODTRAN: Moderate Resolution Atmospheric Transmission
NB: Normalized Brightness Index
NDBI: Normalized Difference Built-up Index
NDVI: Normalized Difference Vegetation Index
NDWI: Normalized Difference Water Index
NIR: Near-Infrared
OLI: Operational Land Imager
PA: Producer's Accuracy
PSF: Point Spread Function
PvSF: Pervious Surface Fraction
QGIS: Quantum Geographic Information System
RMSE: Root Mean Square Error
RTTOV: Radiative Transfer for TOVS
SUHI: Surface Urban Heat Island
SVF: Sky View Factor
SWIR: Short-Wave Infrared
TIRS: Thermal Infrared Sensor
TOA: Top-of-Atmosphere
UA: User's Accuracy
UHI: Urban Heat Island
USGS: United States Geological Survey

1. Introduction

The global average temperature during the first two decades of the 21st century (2001–2020) was 0.99 [0.84 to 1.10] °C higher compared to the period from 1850 to 1900. Notably, the rate of increase in global surface temperature since 1970 has been unprecedented over any 50-year time frame in the past 2,000 years (Intergovernmental Panel on Climate Change, 2023). Additionally, human activities have likely heightened the likelihood of extreme compound events since the 1950s, such as more frequent simultaneous heatwaves and droughts (Intergovernmental Panel on Climate Change, 2023). Rising global temperatures and heatwave events are further intensified in urban areas, due to Surface Urban Heat Island (SUHI) effects, creating compounded thermal stress. Heatwaves are generally described as a sequence of consecutive days with temperatures surpassing normal levels, including extreme seasonal occurrences (such as summer heat) as well as unusual warm spells during other seasons (Perkins et al., 2012). In Indonesia's context, a heatwave is defined as a period of 3 or more consecutive days where the daily temperature exceeds the long-term 95th percentile of the daily mean temperature (World Bank Group & Asian Development Bank, 2021).

Urban populations face heightened vulnerability to heatwaves. As urbanization accelerates globally, cities have become the primary habitat for most of the world's population. Cities characterized by built environments that consist of a specific form contribute to the global effect of an increasing temperature in the city, called Urban Heat Island (UHI). The UHI refers to increased air temperatures in urban areas compared to their surrounding rural areas (Masson et al., 2020). UHI poses a serious risk to public health and will diminish the quality of life in numerous urban areas (Bulatov et al., 2020; Manoli et al., 2020; Wang et al., 2025) and affects increased energy usage, leading to significant economic inefficiencies (Feng et al., 2019; Andriambololonaharisoamalala et al., 2025; Stewart & Oke, 2012). The increase in urban temperature results from the intensification of urban built environment characteristics.

Urban heat absorption and release patterns are determined by the built-up environment's components, such as land cover composition, urban morphology, and material properties. These elements collectively regulate the movement of thermal energy through cities and are closely linked to the subset of UHI known as the SUHI. Several studies have shown that urban form metrics such as building density, green space distribution or height influence the rise of surface temperature (Yin et al., 2018; Sun et al., 2019; Yan et al., 2023). This finding emphasizes the need to understand how those surface representations can influence the estimation of the SUHI effect. Understanding the influences will provide key factors for urban planners to mitigate the impact of increasing SUHI intensity.

This thesis will be organized as follows. The next chapter presents a literature review summarizing SUHI concepts and measurement, urban surface representation influencing SUHI, examining methods for assessing SUHI intensity, and exploring Landsat 8-9 fundamentals and techniques for retrieving Land Surface Temperature (LST). It also outlines the study's research questions and objectives. The following chapter describes the study area and the datasets used. Subsequent sections detail the research methodology, present the results and discussion, and conclude with recommendations for urban policy and future research.

2. Literature Review

2.1. Surface Urban Heat Island: Concepts and Measurement

As mentioned in the introduction regarding the context of Urban Heat Islands (UHI), there are two types of UHIs: surface UHI (SUHI) and atmospheric UHI (AUHI). SUHI is measured based on land surface temperature (LST), while AUHI is measured based on air temperature. AUHI is further classified into canopy layer UHIs (CLHI) and boundary layer UHIs (BLHI) (Zhang et al., 2023). Masson et al. (2020) define SUHI as the temperature differences observed in surfaces such as roofs, roads, and grass between urban neighborhoods and rural areas, whereas UHI is linked to differences in air temperature. The atmospheric Urban Heat Island (UHI) is defined by variations in air temperature (AT) that are recorded with standard thermometers positioned at heights of 1 to 2 meters within the urban canopy layer (Zhang et al., 2023). Compared to the AUHI, the SUHI is influenced by other factors like wind and turbulence, as ambient air temperature is significantly correlated to such parameters and surface temperature is mainly driven by radiation (Hassan et al., 2021), as well as LST has a weak correlation with air temperature and moisture-induced thermal stress (Wang et al., 2025).

Li et al. (2017) found a statistically significant positive log-linear relationship between SUHI and urban area extent in the contiguous United States, noting that SUHI may increase by up to 0.7 °C with a doubling of urban area extent. Regarding the global trend in SUHI intensity from 2003 to 2018, Yuan et al. (2025) reported that the globally averaged SUHI intensity increased at an annual rate of 0.021 °C. Although high-income countries, for instance, the US and China, showed extensive growth in SUHI intensity, the intensification of the urban heat is faster in low-income countries. In terms of proportional changes in SUHI intensity over all the urban areas, daytime SUHI intensity had the highest net proportional rise (27% of urban grids) in low-income countries, while nighttime SUHI intensity net rise was the largest (19% of urban grids) in lower-middle-income countries. Since surfaces heat and cool more rapidly than air, SUHI intensity tends to be strongest during midday or daytime (Estoque et al., 2017).

Numerous studies utilize various techniques to quantify SUHI intensity and analyze spatial patterns (distribution). SUHI is measured using LST, which is primarily derived from thermal infrared (TIR) remote sensing. This method characterizes the thermal behaviors of underlying surfaces and is more sensitive to urban form and human activities (Yao et al., 2018). It allows for spatially continuous LST observations across wide areas. LST data are the primary data sources for LST-based SUHI studies, such as MODIS (Moderate Resolution Imaging Spectroradiometer) data, which are commonly used for global and large-area studies because of their broad spatial coverage and good temporal resolution (4 overpasses per day), while the Landsat series data (e.g., TM and ETM+) with finer spatial resolution (30 m) are suitable for urban-scale LST variations studies (Masson et al., 2020). Furthermore, the following sections will introduce specific features related to the research on the spatial distribution and intensity of SUHI. Additionally, this section covers the characteristics of SUHI in tropical climates, such as Indonesia, which may differ from those in other regions.

2.1.1. Spatial Distribution of SUHI

Analyzing the spatial distribution of SUHI is crucial for identifying areas where heat challenges are most severe and where mitigation efforts will be most effective. This analysis also helps link SUHI patterns to specific environments. The spatial patterns of SUHI are significantly influenced by the physical characteristics of the built environment, such as the amount and arrangement of impervious surfaces and green spaces. The distribution of SUHI is largely regulated by the spatial configuration of urban elements, including urban morphology (both two-dimensional and three-dimensional patterns). Highly aggregated or dense impervious patches can significantly intensify SUHI (Shao et al., 2023).

To analyze the spatial distribution of SUHI, several methods commonly used in geospatial studies employ Landsat or MODIS data. These methods include Urban-Rural Gradient Analysis, Spatial Metrics-based Analysis, and Local Climate Zone (LCZ). Urban-Rural Gradient Analysis determines the spatial variability of LST and land cover (impervious surfaces/green spaces) by defining multiple concentric buffer zones extending outward from the city center (Estoque et al., 2017). Second method such as Spatial Metrics-based Analysis will assess how spatial characteristics—such as size, shape complexity, and clumping of impervious surfaces and green spaces—affect LST variability. The research showed that aggregation had the most consistent and strong correlation with mean LST across different cities (Estoque et al., 2017). The most recognized method, proposed by Stewart and Oke (2012), is LCZ. This classification system standardizes the description of urban and rural landscapes for temperature studies. The LCZ facilitate consistent documentation of site metadata and classify landscapes based on their surface structures and cover properties at local scales, ranging from hundreds of meters to several kilometers.

2.1.2. SUHI Intensity

The accurate measurement of the SUHI intensity is crucial for developing effective adaptation measures and mitigation strategies (Li et al., 2017). SUHI intensity is the most used metric for studying the urban thermal environment and quantifying the UHI effect (Deilami et al., 2018; Meng et al., 2023). SUHI intensity is directly proportional to land use. A widely recognized approach to calculate SUHI intensity, known as the Temperature Dichotomy Method, is the difference of average LST between urban pixels (LSTurban) and suburban/non-urban pixels (LSTnon-urban) (Zhang et al., 2023). Moreover, a study also calculated the SUHI intensity by the differences of average surface temperature in urban (Tu) and suburban/non-urban (Ts) areas (Meng et al., 2023).

Measuring SUHI intensity presents several challenges, primarily due to the lack of an objective and universal definition for "rural" reference areas. This ambiguity creates uncertainty in SUHI intensity results, as rural characteristics can vary significantly across different cities (Stewart and Oke, 2012). Furthermore, variations in the phenological stage of rural vegetation, such as harvested versus green crop fields, can also influence SUHI intensity calculations, while forests can exaggerate SUHI values simply because trees are cooler even when the urban area remains hot (Radoux et al., 2025). Therefore, Radoux et al. (2025) suggest redefining SUHI using a stable land cover reference such as broadleaf trees or permanent grassland, instead of comparing cities to an arbitrarily defined rural area.

The subjectivity involved in defining urban and rural boundaries can result in significant inconsistencies, as evidenced by the 42% relative difference found in global studies. Thus, there is a need for more standardized approaches, such as LCZ (Yang et al., 2023). Stewart and Oke (2012) propose a climate-based framework that defines LCZ using 17 standard classes. This system helps mitigate bias and uncertainty in SUHI measurements by allowing for the calculation of specific landscape types, such as LCZ D (low plants) or LCZ A (dense trees). This comparability of UHI intensities across different cities is particularly valuable, regardless of their unique geographical contexts.

Another approach, as discussed in research by Radoux et al. (2025), involves reconstructing LST as a linear mixture of thermal effects from different land cover types. In this method, the temperature of a pixel is calculated by taking the average temperature of the study area and adding the weighted contributions of each land cover type within that pixel. This approach is particularly effective when dealing with mixed pixels and allows for the quantification of land cover-specific heat contributions.

Various aspects, including urban form and ecological circumstances, might influence the strength of the SUHI effect. The increase in urban patch size and the density of buildings strengthens the SUHI effect considerably. This is especially true for areas with three-dimensional (3D) morphology, where high-rise buildings can create a cooling effect during the day by providing shade. However, at night, these buildings can exacerbate warming by trapping heat and reducing wind speed (Shao et al., 2023). In terms of land cover, Impervious

Surface Area (ISA) is the primary driver of the increase of LST due to the material characteristics like concrete and asphalt absorb significant solar radiation and store heat, leading to higher temperature (Imhoff et al., 2010; Shao et al., 2023)

2.1.3. SUHI in Tropical Cities

The SUHI phenomenon in tropical cities has distinct characteristics that are heavily influenced by high humidity and consistently warm temperatures. This leads to unique diurnal patterns and specific vulnerabilities. Equatorial and tropical countries experience high levels of solar radiation and persistent warmth throughout the year (Shao et al., 2023). In equatorial cities, strong daytime solar radiation drives surface heating, while frequent precipitation maintains cooler rural vegetation, resulting in a pronounced daytime SUHI intensity due to the contrast between the hot, impervious urban surface and the surrounding vegetated rural area (Sismanidis et al., 2022).

This pattern often follows the "inverse spoon" diurnal cycle, commonly observed in subtropical and tropical cities, where wet, vegetated rural areas remain cooler than urban areas, especially near solar noon. As a result, the SUHI can persist throughout the 24-hour cycle because urban surfaces retain and slowly release heat, while rural surfaces remain cooler due to moisture-driven evaporative cooling (Stewart et al., 2021). A study conducted in tropical East Africa revealed that the highest mean urban area average of Tropical SUHI is attributed to the presence of surface moisture (such as soil moisture and water) and high evapotranspiration in the surrounding areas, which act as a strong cooling mechanism during the day, rather than relying solely on the ratios of impervious surfaces to vegetation (Garuma, 2023).

Similarly, the high humidity in tropical cities maximizes the temperature difference between urban and rural areas, as well as the ratio of surface sensible heat flux to latent heat flux (Gu and Li, 2018). Research conducted by Estoque et al. (2017) focusing on Southeast Asian megacities, which serve as highly relevant tropical settings, confirms these trends. Results shown in Greater Jakarta indicate that the UHI effect is noticeable in both SUHI and AUHI, with intensities measured at approximately 3°C–6°C for LST and 1°C–2.5°C for air temperature differences (Siswanto et al., 2023). Furthermore, Siswanto et al. (2023) measure that the SUHI intensity in Greater Jakarta is highest during the monsoonal transition period (September–December), and a long-term assessment (2001–2020) showed an upward trend in the nighttime SUHI area across all seasons.

2.2. Urban Surface Representation Influencing SUHI

2.2.1. Land Use/Land Cover

The relationship between Land Use/Land Cover (LULC) and the UHI effect is extensively analyzed in urban climate research globally. Evidence suggests that changes in LULC, particularly the transformation of natural landscapes into urban settlements, significantly impact the thermal environment (Jamei et al., 2019). Researchers utilize remote sensing techniques to quantify this relationship by measuring LST and comparing it with metrics such as the Normalized Difference Built-up Index (NDBI) and the Normalized Difference Vegetation Index (NDVI) (Jamei et al., 2019).

In various cities, LST is heavily influenced by surface properties. A strong correlation has been found between mean LST and the density of impervious surfaces, such as roads, pavements, and construction materials, which replace natural cooling surfaces and contribute to a warmer urban environment (Santamouris, 2013; Jamei et al., 2016; Estoque et al., 2017). Materials like asphalt and concrete increase thermal sensitivity, reduce evapotranspiration, and promote heat absorption and re-radiation, particularly at night (Dissanayake et al., 2019). For example, Imhoff et al. (2010) identified Impervious Surface Area (ISA) as a key driver, noting that ISA accounted for about 70% of the total LST variance in the continental U.S.

In contrast, natural land covers, such as green spaces, have a negative correlation with LST (Estoque et al., 2017). Vegetation helps mitigate heat through processes such as evapotranspiration and shading, which convert surface heat flux into latent heat and thereby reduce air temperature (Zhao et al., 2023). In Chinese cities, the Urban Green Space Index (UGI) has been found to make the largest relative contribution to reducing UHI intensities (Zhou et al., 2022).

2.2.2. Urban Morphology

Urban morphology plays a critical role in shaping the thermal environment of cities, as the physical characteristics of urban surfaces directly influence LST and the SUHI. This thermal behaviour is further explained by Stewart and Oke (2012), who defined the sky view factor (SVF) as the ratio of the amount of sky hemisphere visible from ground level to that of an unobstructed hemisphere. This can be associated with taller and more compact buildings, which leads to greater retention of infrared radiation in street canyons due to restricted view of the radiatively cold sky hemisphere, thereby elevating surface temperatures (Stewart and Oke, 2012).

The composition of urban surfaces in terms of their built coverage further determines how cities absorb, store, and release heat, making surface fraction metrics essential variables in understanding SUHI dynamics. Stewart and Oke (2012) characterized these surface properties through three key metrics:

1. Building Surface Fraction (BSF), defined as the proportion of ground surface with building cover, which affects surface reflectivity, flow regimes, and heat dispersion above ground;
2. Impervious Surface Fraction (ISF), referring to the proportion of ground surface with impervious cover such as paved or rock surfaces, which affects surface reflectivity, moisture availability, and heating and cooling potential; and
3. Pervious Surface Fraction (PvSF), representing the proportion of ground surface with pervious cover including bare soil, vegetation, and water, which similarly influences surface reflectivity, moisture availability, and heating and cooling potential.

The above three indicators are also verified to play an important role in inducing LST variation in empirical data. BSF was found to cause a stable and significant positive warming effect on LST, and it has an even stronger influence on LST in dense and open low-rise building types under compact and open LCZs, respectively (Zhou et al., 2024). Similarly, BSF and building height showed a moderate positive relationship with LST, indicating that building area coverage and building height are associated with higher surface temperatures (Ge et al., 2025). Expanding ISF due to urbanization was shown to positively affect thermal storage and latent heat flux, thereby increasing the SUHI effect (Li et al., 2025). For PvSF, it was negatively correlated with LST across nearly all building types and LCZs, acting as a thermal regulator (Li et al., 2025; Ge et al., 2025). All the above results indicated that BSF and ISF positively regulated LST and contributed to intensifying SUHI, whereas PvSF showed a negative correlation with LST, demonstrating the significance of three morphological factors for studying the urban thermal environment (Li et al., 2025; Zhou et al., 2024; Ge et al., 2025).

2.2.3. Local Climate Zone (LCZ)

The LCZ classification system, formally proposed by Stewart and Oke in 2012, was developed to provide a universal research framework for UHI studies and to standardize the description of urban and rural measurement sites. LCZs are defined as areas characterized by consistent surface cover, structure, materials, and human activities, ranging from hundreds of meters to several kilometers in horizontal extent (Stewart and Oke, 2012). Additionally, Stewart and Oke (2012) also described that each LCZ is uniquely named and categorized based on one or more defining surface characteristics, typically related to the height or arrangement of roughness elements or the primary land cover type. This study examines the physical properties of different zones, focusing on the building surface fraction, which is the percentage of the building's footprint area compared to the total footprint area. It also assesses the PvSF, determined by the ratio of pervious plan area such as bare soil, vegetation, water) to the total footprint area, presented as a percentage (Stewart and Oke, 2012).

The LCZ classification system consists of 17 distinct zones (see Figure 1), including 10 built types that are graded based on the compactness and building height, ranging from LCZ 1, compact high-rise, to 10 heavy industry, as well as 7 natural land cover types. For detailed descriptions of LCZ type and surface properties essential for identifying each LCZ used in this study, specified Table 1, taken from Stewart and Oke (2012).

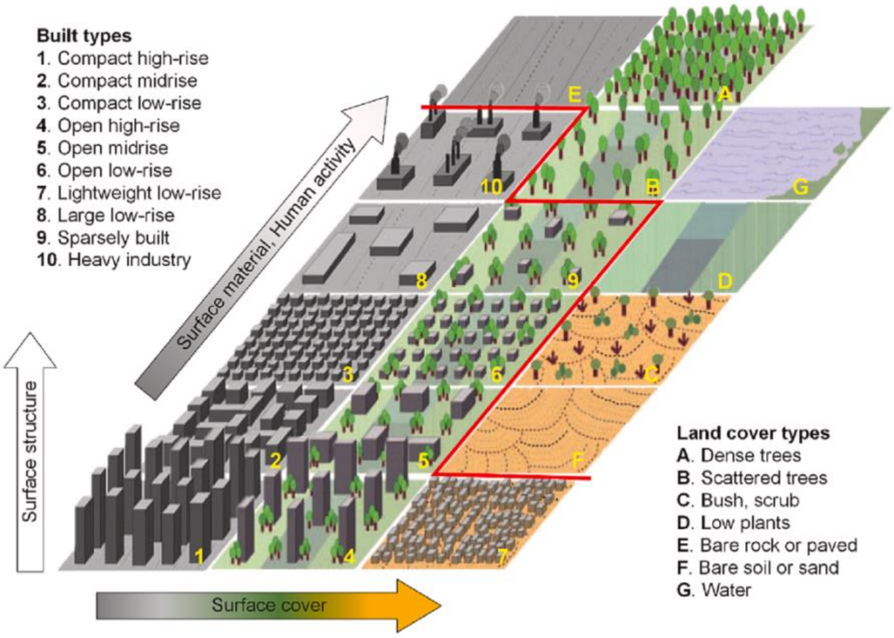

Figure 1: The 17 standard LCZs: 10 built types (LCZs 1–10) and 7 land cover types (LCZs A–G), illustrated by Huang et al. (2023), modified from Stewart and Oke (2012).

Table 1 LCZ Type and Threshold Classification

LCZ type	Definition	BSF value	PvSF value
LCZ 2 - Compact midrise 	A densely packed group of midrise buildings (3–9 stories) with few or no trees, primarily featuring paved surfaces. Construction materials include stone, brick, tile, and concrete	40-70	<20
LCZ 3 - Compact low-rise 	A close arrangement of low-rise buildings (1–3 stories) that also has few or no trees and is mostly paved, using materials like stone, brick, tile, and concrete.	40-70	30-40

LCZ type	Definition	BSF value	PvSF value
LCZ 6 - Open low-rise 	An open layout of low-rise buildings (1–3 stories) that contains a lot of pervious land cover, such as low plants and scattered trees. Common materials include wood, brick, stone, tile, and concrete.	60-90	<30
LCZ 8 - Large low-rise 	An open layout of large low-rise buildings (1–3 stories) with few or no trees, primarily paved. The main construction materials are steel, concrete, metal, and stone.	10-20	<20
LCZ 9 - Sparsely built 	A sparsely located set of small or medium buildings within a natural environment, featuring abundant pervious land cover with low plants and scattered trees.	20-30	60-80
LCZ A - Dense trees 	A heavily forested area predominantly comprising deciduous and/or evergreen trees, with mostly pervious land cover (low plants). This zone functions as a natural forest, tree plantation, or urban park.	<10	>90
LCZ D - Low plants 	A flat landscape dominated by grass or herbaceous plants and crops, containing few or no trees. It serves as natural grassland, agricultural land, or an urban park.	<10	>90
LCZ E - Bare rock or paved 	A plain landscape characterized by rock or paved surfaces, featuring few or no trees or plants. This zone includes natural desert (rock) or urban transportation areas.	<10	<10
LCZ F - Bare soil or sand 	A simple landscape of soil or sand with minimal tree or plant cover, functioning as natural desert or agricultural space.	<10	>90
LCZ G - Water 	Extensive open water bodies, such as seas and lakes, as well as smaller water bodies like rivers, reservoirs, and lagoons	<10	>90

Several studies across the world has examined the relationship between LCZ and SUHI intensity, resulting that the warmest zones are Compact built types (LCZs 1–3), for example in LCZ 2 reach approximately 5°C in Budapest (Dian et al., 2020) and are significantly high in Jiangmen (Yang et al., 2020). Compact low-rise (LCZ 3) was also found to be a warm area in Nagpur, India (Kotharkar and Bagade, 2018). Natural zones like Dense Trees (LCZ A) and Water (LCZ G) act as cooling zones. Forested areas (LCZ A) often show negative SUHI intensity values, indicating they are cooler than rural averages (Dian et al., 2020).

In terms of contextuality, the surrounding landscape of LCZ affects its thermal signature. For example, in Budapest, areas classified as Open Midrise (LCZ 5) showed varying temperatures depending on whether they were adjacent to industrial districts or residential low-rise areas (Dian et al., 2020).

2.2.4. Roofing Material

Specific building and roofing materials significantly affect SUHI estimation based on their albedo (solar reflectance), thermal emittance, and heat storage capacity. A study in Bahrain examined commonly materials that correlate with Solar Reflectance Index (SRI). Metal roofs, such as Aluminium-zinc panels has a high Solar Reflectance Index (SRI) of 60–70%, reflecting large amounts of heat (Radhi et al., 2014). Clay tiles in terracotta are the most efficient (67% SRI), while fiber-cement tiles in black have a much lower SRI of 37% (Alchapar et al., 2014). Furthermore, Radhi et al. (2014) study also resulted in the conclusion that the color features behave differently, such as White ceramic tiles and beige porcelain were the top performers due to high SRI values. Conversely, black and red granite were the worst performers, developing the highest surface temperatures.

In terms of energy balance, a study by Stache et al. (2022) demonstrates that albedo (solar reflectance) is a primary determinant of heat absorption, with values varying widely based on a material's specific type and color. The study highlights the following thermal characteristics: Darker materials exhibit the lowest reflectance, with bitumen (dark grey) at 0.02 and black High Pressure Laminate (HPL) at 0.03. These materials absorb nearly all incoming radiation—up to 98% for bitumen and 97% for black HPL. Materials like grey concrete tiles (0.13), red masonry brick (0.26), and Western Red Cedar (0.31) show moderate albedo levels. Pinewood and white HPL achieved the highest albedo in the study (0.35), reflecting significantly more solar energy than their darker counterparts

2.3. Landsat 8-9 Fundamentals for Retrieving Land Surface Temperature

Landsat data are strongly suitable for SUHI research because the thermal sensors enable the effective identification of urban heat. One of its major strengths is its high spatial resolution, which facilitates analyzing the relationship between the changes in land surface temperature (LST) and the surface features such as impervious surface, vegetated surface, etc. (Xu et al., 2023; Zhou et al., 2014; Cetin et al., 2024). However, there are significant issues and limitations associated with the 16-day revisit interval of the Landsat satellites (Xu et al., 2023). This limitation necessitates the use of multisource Landsat images, which can show inconsistencies in the retrieved LST products due to differences between sensors (Xu et al., 2023). Additionally, Landsat 8's Thermal Infrared Sensor (TIRS) is known to have a historical problem with stray light artifacts (Montanaro et al., 2014). Furthermore, the following section provides a detailed explanation of sensors and the retrieval of Land Surface Temperature (LST).

2.3.1. Sensors Specification

The Landsat mission, originating in 1972, is fundamentally a multispectral Earth observation program that systematically provides multi-band measurements across the electromagnetic spectrum. It is a cooperative program between NASA and the U.S. Geological Survey (USGS) designed to collect and archive a globally comprehensive, moderate-resolution image data record, ensuring continuity for multi-decadal studies of land cover change (Irons et al., 2012; Roy et al., 2016; Wulder et al., 2019). The earlier Landsat satellites (Landsat 1-3) contained a Multispectral Scanner (MSS) which sensed radiation within four different spectral bands (two visible and two near-infrared or NIR) (Young et al., 2017). Subsequent Landsat missions had a Thematic Mapper (TM) (Landsat 4-5) or an enhanced thematic mapper plus (ETM+) (Landsat 7), with an increased number of sensing bands to seven. These extended the detection to the middle-infrared (now often referred to as SWIR or shortwave IR) and the thermal infrared (TIR) regions of the spectrum (Young et al., 2017).

The latest Landsat mission, Operational Land Imager (OLI), was launched in 2013. Landsat 8 continues the advancement of satellite sensors, offering improved spectral band passes and a more enhanced radiometric resolution of 12 bits, with nine multispectral bands alongside TIRS (Roy et al., 2016; Wulder et al., 2018). Landsat 9 was launched in 2021 as its successor. Together, these satellites reduce the revisit period of previous Landsats (Landsat 4-8 revisit 16 days) to roughly 8 days. Both Landsat 8 and 9 are equipped with the OLI and the TIRS Band 10 (10.60–11.19 μm) (Irons et al., 2012; Li & Chen, 2020; Wulder et al., 2022).

A key feature of the Landsat 8 and 9 sensors is their improved radiometric resolution (12 bits for the OLI on Landsat 8) and high geometric precision (Irons et al., 2012; Roy et al., 2014). The TIRS collects data in two thermal bands, with Landsat 8's TIRS frequently used for thermal applications, initially derived at a resolution of 100 meters (Irons et al., 2012; Elmes et al., 2020; Cetin et al., 2024).

2.3.2. Land Surface Temperature (LST) Algorithms

LST is primarily retrieved from space using three main categories of algorithms, provided the LSEs are known: single-channel methods (SCM), multi-channel methods (such as split-window algorithms or SWA), and multi-angle methods (Li et al., 2013):

1. Single-Channel Method (SCM)
   LST (Land Surface Temperature) is typically retrieved using a single-channel algorithm applied to TIRS Band 10. This process often incorporates atmospheric functions calculated from in-situ or modeled atmospheric data (Elmes et al., 2020; Cetin et al., 2024). The main procedure involves converting the radiance into LST by inverting the Radiative Transfer Equation (RTE) after correcting for residual atmospheric attenuation and emission. This conversion requires input on atmospheric profiles, as noted by Li et al. (2013), referencing Chédin et al. (1985), Hook et al. (1992), and Li et al. (2004a). The generalized Simplified Climate Model (SCM), developed by Jiménez-Muñoz and Sobrino (2003), only requires LSE and the total atmospheric water vapor content. When applied to Landsat 8 data, the SCM has demonstrated high accuracy, with a root mean square error (RMSE) of 0.83°C (Jiménez-Muñoz et al., 2014).

2. Multi-Channel Method (Split-Window Algorithm - SW)
   The SW algorithm utilize the differential atmospheric absorption observed in two adjacent thermal channels (typically centred around 11 μm and 12 μm) to estimate LST, as introduced by McMillin (1975, as cited in Li et al., 2013). This method is dependent on knowing the mean surface emissivity (ϵ) and the difference in emissivities (Δϵ) between the two channels, as the coefficients are often parameterized as functions of these variables (Wan & Dozier, 1996; Madeira, 2002; Trigo et al., 2008, as cited in Li et al., 2013). Li et al. (2013) further described that the accuracy of the Split-Window Algorithm (SWA) can be compromised when there is a high amount of total column water vapor (WV) or at large viewing zenith angles (VZA). Implementing SWA on Landsat 8 data requires utilizing the TIRS Bands 10 and 11, which fulfill the two-band prerequisite at wavelengths of approximately 11 μm and 12 μm, respectively. However, applying SWA

presents distinct technical challenges, as SW algorithms face a trade-off where including more input parameters can reduce retrieval error but simultaneously introduces additional uncertainties that compromise accuracy (Sòria & Sobrino, 2007, as cited in Li et al., 2013), and the selection of the best algorithm depends on prior knowledge of water vapor content and LSE (Kerr et al., 2000, as cited in Li et al., 2013).

3. Simultaneous Retrieval/Hyperspectral Methods
   Stepwise Retrieval Method first estimates LSE (e.g., using NDVI-based methods or temperature-independent spectral indices) and then applies a single or multi-channel method for LST retrieval (Li et al., 2013). More complex methods, typically requiring hyperspectral data (sensors with hundreds of narrow channels), simultaneously retrieve LST, LSE, and atmospheric profiles or quantities as cited by Li et al. (2012), who reference Ma et al. (2002) and Borel (2008). This includes Linear Emissivity Constraint Temperature Emissivity Separation (LECTES) (Wang et al., 2011)

Many studies have confirmed that acquiring LST requires robust atmospheric correction, as the radiance measured by sensors at the Top-of-Atmosphere (TOA) depends on surface parameters (temperature and emissivity) as well as atmospheric effects, including attenuation and emission (Li et al., 2013; Sobrino et al., 2013). For Landsat data, atmospheric correction converts TOA radiance to surface radiance, which is particularly critical for consistent multi-temporal comparisons and when developing empirical models that must be transferable beyond the development data (Young et al., 2017).

The presence of cloud cover, particularly in tropical regions, poses a major challenge to acquiring sufficient clear-sky thermal observations necessary for continuous land monitoring. Areas characterized by tropical rainforests near the equator experience frequent high cloud cover and are thus severely contaminated by clouds (Li and Chen, 2020). This increased observation frequency helps address data scarcity, although the global mean average cloud-weighted number of observations for the three available sensors in 2018 was still only 81.9 (Li & Chen, 2020). All satellite-based LST determination requires initial cloud screening or cloud masking and products like the Landsat-8 Level 2 data include a spatially explicit 30 m Quality Assessment (QA) band with cloud and cirrus cloud masks (USGS, 2015). For data analysis, raw Digital Numbers (DNs) must undergo radiometric correction. This absolute correction process converts the DNs into comparable physical units, such as radiance or reflectance, which is essential for multi-temporal comparisons (Young et al., 2017).

2.3.3. Retrieval of Land Surface Temperature (LST)

Retrieval of Land Surface Temperature (LST) is crucial for understanding surface energy balance and turbulent heat fluxes (Li et al., 2013; Trigo et al., 2008). To retrieve the LST, a tool called LANDARTs (Landsat Automatic Retrieval of Ts or Surface Temperature), developed by Tardy et al. (2016) using Python, is employed. LANDARTs automatically estimates LST by calculating surface emissivity and performing atmospheric corrections, integrating the European Centre for Medium-Range Weather Forecasts (ECMWF) Application Programming Interface (API) to retrieve vertical atmospheric fields across 37 pressure levels. For this study, the LANDARTs tool was configured using its available options to ensure compatibility with the current ECMWF API, with the Radiative Transfer for TOVS (RTTOV) selected as the radiative transfer model in place of the Moderate Resolution Atmospheric Transmission (MODTRAN), and to apply the NDVI threshold method (NDVI_THM) for surface emissivity estimation. The detailed workflow is illustrated in Figure 2 below.

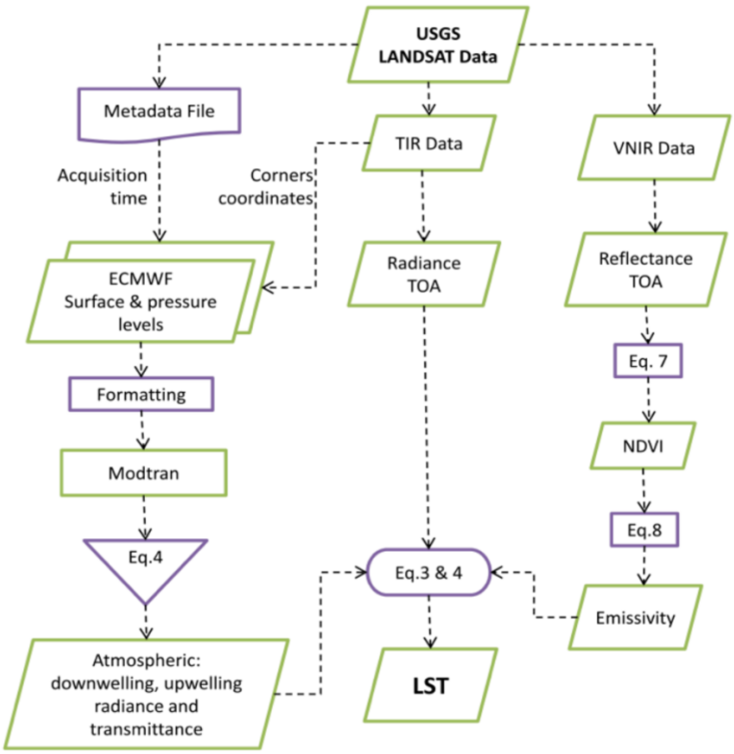

Figure 2: Flowchart of the LANDARTs algorithm to generate LST images at a resolution of 30 m (Tardy et al., 2016)

The first stage of the LANDARTs process involves the calculation of atmospheric correction parameters using a physical approach based on radiative transfer modeling. This is fundamentally rooted in Planck's law, which describes the spectral distribution of radiation from a blackbody:

$$B\lambda(T) = \frac{C_1}{\lambda^5[\exp\left(\frac{C_2}{\lambda T}\right) - 1]}$$

In this equation, $B\lambda(T)$ represents the spectral radiance ($W \cdot m^{-2} \cdot sr^{-1} \cdot \mu m^{-1}$) emitted by a perfect blackbody at temperature T (K) and wavelength λ (μm^{-1}), while C1 and C2 are physical constants ($C1 = 1.191 \times 10^8\ W \cdot \mu m^{-4} \cdot sr^{-1} \cdot m^{-2}$, $C2 = 1.439 \times 10^4\ \mu m \cdot K$). In practice, however, land surfaces detected by remote sensing behave as gray bodies rather than perfect blackbodies, meaning their surface emissivity is less than one ($\epsilon s < 1$).

To account for atmospheric interference, Tardy et al. (2016) explain that the tool must solve the radiative transfer equation to determine atmospheric transmittance ($\tau\lambda$), upwelling radiance (Lu,λ,atmo), and downwelling radiance (Ld,λ,atmo) specified as Equation 3:

$$L\lambda, sen(T) = \tau\lambda\epsilon s, \lambda B\lambda(T) + Lu, \lambda, atmo + \tau\lambda(1 - \epsilon s, \lambda)Ld, \lambda, atmo$$

The variables in the radiative transfer equation are defined as follows: Lλ,sen is the spectral radiance recorded at the sensor level at the top of the atmosphere ($W \cdot m^{-2} \cdot sr^{-1} \cdot \mu m^{-1}$); Bλ denotes the blackbody radiance at a given kinetic surface temperature T (K); τλ is the atmospheric transmittance at wavelength λ (μm); Lu,λ,atmo and Ld,λ,atmo refer to the upwelling and downwelling atmospheric radiance within the wavelength window ($W \cdot m^{-2} \cdot sr^{-1} \cdot \mu m^{-1}$), respectively; and ϵs,λ is the surface spectral emissivity.

LANDARTs automates this by retrieving vertical atmospheric fields from the ECMWF database and processing them through RTTOV to produce a spatialized grid of correction parameters for the entire Landsat scene, mitigating LST errors of up to 2°C (Tardy et al., 2016). The second stage of the process is the estimation of Land Surface Emissivity (LSE), which is critical because land surfaces are "grey bodies" with an emissivity less than one. In this study, the NDVI threshold method (NDVI_THM) is applied, using NDVI to characterise surface properties (Equation 7):

$$NDVI = \frac{\text{NIR} - \text{RED}}{\text{NIR} + \text{RED}}$$

Unlike the mixed pixel emissivity formula used in the original tool, NDVI_THM assigns emissivity values based on threshold classifications of NDVI, distinguishing bare soil, mixed, and fully vegetated pixels without requiring the empirical shape parameter k. In the final stage, the tool retrieves the kinetic land surface temperature by inverting the radiative transfer equation and applying a simplified version of Planck's law in Equation 4 below, adapted to the specific spectral window of the Landsat sensor:

$$LST = \frac{K_2}{In\left(1 + \frac{K_1}{B\ (T)}\right)}$$

Where $B\ (T)$ is the corrected surface radiance, and K_1 and K_2 are pre-launch calibration constants provided by the USGS. This synthesis of automated atmospheric profiling and pixel-by-pixel emissivity correction allows LANDARTs to produce spatially coherent LST maps that Tardy et al. (2016) validated against in situ measurements and Advanced Spaceborne Thermal Emission (ASTER) data, showing a significant improvement in accuracy over single-point correction methods.

3. Research Question and Objectives

The overarching objective of the research is to generate empirically grounded planning-relevant thresholds for land cover composition and built intensity that can support SUHI mitigation and inform urban development policies in Indonesia. More specifically, the study investigates how the spatial distribution of land cover composition, urban form/LCZ, and surface material shapes the estimation of SUHI in Tegal, Indonesia. By combining land cover data, LCZ reflecting neighbourhood-scale urban form, and roofing material representing surface material, this study aims to provide a more comprehensive understanding of how urban surface representation contributes to SUHI formation.

The research question can be expressed as follows:

How does urban surface representation, including land cover, urban form, and roof materials, affect the estimation and interpretation of the Surface Urban Heat Island?

Three specific objectives are defined to answer the research question:

Objective 1: Mapping and Characterization of Urban Surface Representation and SUHI
The first objective is to map and characterize the urban surface representation and SUHI in Tegal City. This is achieved by identifying and quantifying land cover, LCZs, and roofing materials within the study area. Specifically, the land cover map is updated using Sentinel-2 spectral indices, the study area is classified into LCZs to characterize the urban form structure, and multi-temporal Landsat imagery is processed to retrieve LST data.

Objective 2: Analyze the Influence of Urban Surface Representation on SUHI Estimation
The second objective is to assess how variations in land cover, urban form, and materials affect LST spatial variability and SUHI patterns. This involves analyzing the thermal contributions of urban surfaces and their roles in surface temperature patterns. The relationship between urban morphology and thermal response is measured using the Pearson correlation coefficient (r), aligning multi-date satellite observations with static indicators to study localized heat accumulation.

Objective 3: Evaluate the Combined Effects of Composition, Form, and Materials
The third objective is to evaluate and compare the explanatory power of land cover composition, LCZ-based urban form, and roofing material properties on LST spatial variability. This involves comparing the performance of land cover and LCZ-based regression models and examining whether roofing material characteristics explain residual thermal patterns not captured by either model.

4. Materials

The materials section will describe the dataset used in this study, including the study area, the Landsat 8-9 dataset with its specifications and limitations.

4.1. Study Area

The research study focuses on Tegal City, located in Central Java Province, Indonesia, as shown in Figure 1. Tegal was chosen as a representative example of small coastal cities that are characteristic of many locations along Java Island, the most populous island in Indonesia. According to the Tegal City Central Bureau of Statistics (2023), Tegal City covers an area of 39.68 km² and has a population of 282,781 people. It consists of 5 districts and 27 subdistricts. Over the past five years, Tegal has experienced several heatwaves. One factor that may contribute to this issue is the conversion of agricultural land to built-up areas, with an average annual rate of 2.07% observed from 1993 to 2017 (Innayatuhibbah et al., 2019).

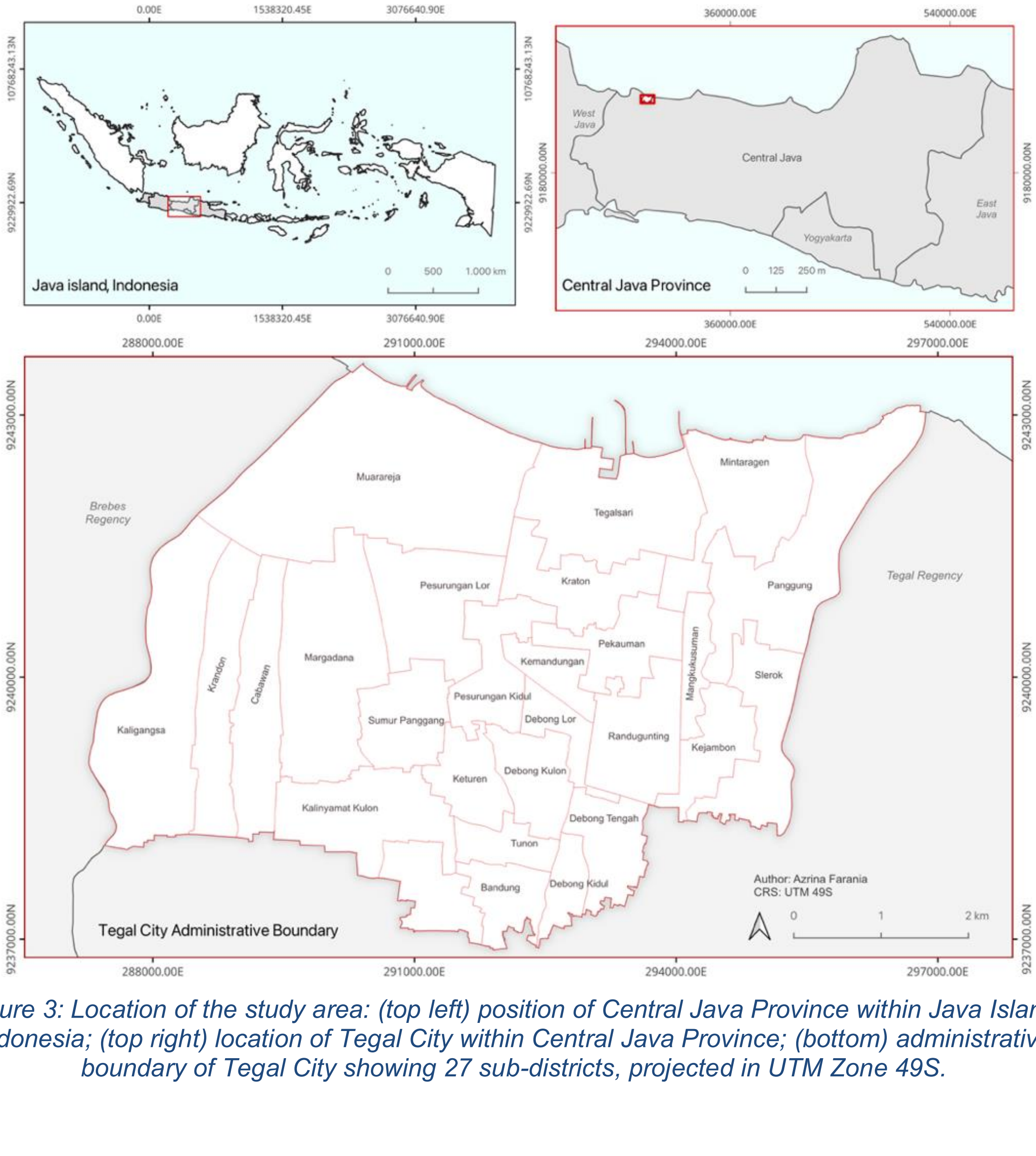

Figure 3: Location of the study area: (top left) position of Central Java Province within Java Island, Indonesia; (top right) location of Tegal City within Central Java Province; (bottom) administrative boundary of Tegal City showing 27 sub-districts, projected in UTM Zone 49S.

According to data from the reanalysis ERA5 dataset in 0.25° × 0.25° grid (Copernicus Climate Change Service, 2023), there were seven recorded heatwave events from 2020 to 2024. Heatwave is defined as an event that lasts for at least 3 consecutive days in which the temperature exceeds the long-term daily mean temperature at the 95th percentile (31.48 o C) by the World Bank and the Asian Development Bank (2021). A heatwave occurred from 25 September 2023 to 24 December 2023, with an average duration of 3 to 8 days in Tegal City. There was a rare heatwave that lasted for 14 consecutive days and ended on 24 December 2023. Table 2 and the visualizations in Figure 4 below illustrate the heatwave events in Tegal City from 2020 to 2024.

Table 2: Heatwave Events in Tegal City (2020-2024)

Number	Start Date	End Date	Average Temperature (°C)	Duration (days)
1	2023-09-25	2023-09-30	31.97	6
2	2023-10-06	2023-10-09	32.18	4
3	2023-10-15	2023-10-18	32.36	4
4	2023-10-26	2023-11-02	32.42	8
5	2023-11-06	2023-11-08	31.99	3
6	2023-11-18	2023-11-22	32.39	5
7	2023-12-11	2023-12-24	32.22	14

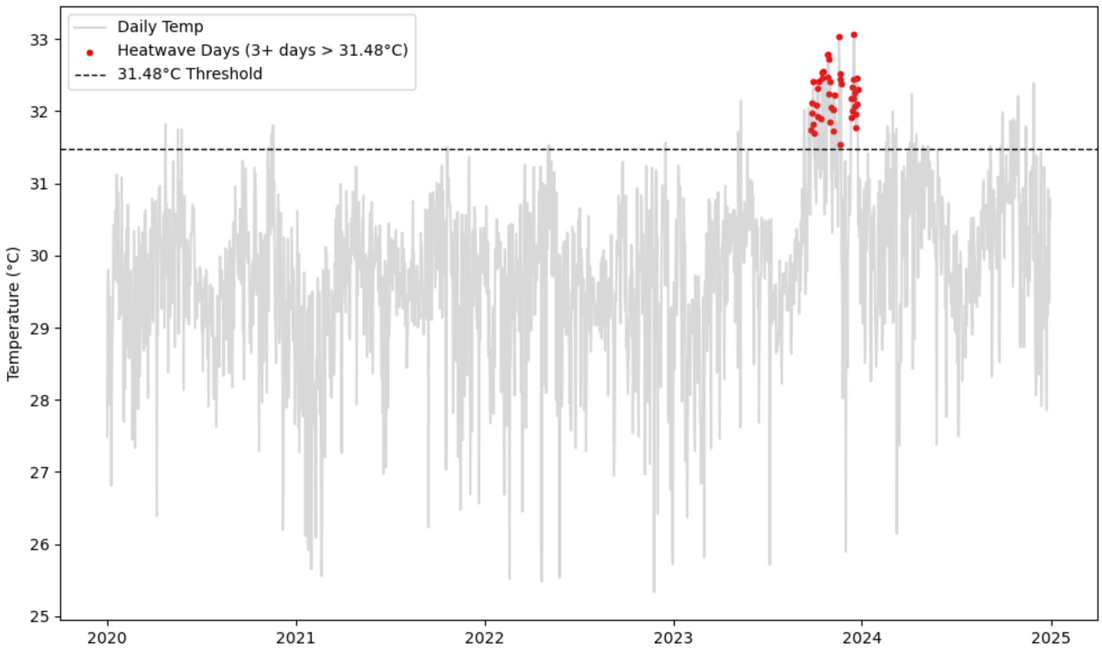

Figure 4: Daily mean air temperature in Tegal City (January 2020 - December 2024) from ERA5 data (0.25° grid). The dashed line marks a heatwave threshold of 31.48°C (95th percentile). Red bars indicate heatwave events (three or more consecutive days above this threshold). Seven events were identified, with six in 2023–2024 selected for LST.

4.2. Landsat 8-9 Images

Landsat 8-9 images were from the U.S. Geological Survey, Earth Explorer. This study used two different processing levels from the Landsat Collection 2 archive: Level-1 data from the OLI and TIRS, alongside Level-2 Surface Temperature (ST) products. This approach will allow a rigorous comparison of models by accounting for surface emissivity. Band specification for Level-1 OLI/TIRS data is specified in Table 3 below.

Table 3: Band Specification of Landsat 8/9 Level-1

Band	Name	Wavelength (μm)	Resolution (m)
Band 1	Coastal aerosol	0.43 – 0.45	30
Band 2	Blue	0.45 – 0.51	30
Band 3	Green	0.53 – 0.59	30
Band 4	Red	0.64 – 0.67	30
Band 5	NIR	0.85 – 0.88	30
Band 6	SWIR 1	1.57 – 1.65	30
Band 7	SWIR 2	2.11 – 2.29	30
Band 8	Panchromatic	0.50 – 0.68	15
Band 9	Cirrus	1.36 – 1.38	30
Band 10	TIRS 1	10.60 – 11.19	100 (resampled to 30)
Band 11	TIRS 2	11.50 – 12.51	100 (resampled to 30)

The U.S. Geological Survey (2004) reports that the Landsat Collection 2 Level-2 ST product is derived from Level-1 thermal infrared bands, TOA reflectance, and TOA brightness temperature. These are combined with ASTER Global Emissivity Database (GED), ASTER NDVI, and reanalysis atmospheric profile data (geopotential height, specific humidity, and air temperature). The use of Band 10 and ASTER GED in particular is required for emissivity correction. Additionally, the ST product is generated via a Single-Channel algorithm developed collaboratively by the Rochester Institute of Technology (RIT) and the NASA Jet Propulsion Laboratory (JPL).

During the heatwave period, Landsat images were selected based on these specific events to more accurately assess the SUHI estimation at consistent temperatures over several days, as detailed in the Table 4 below. The images chosen for Tegal City had to meet the criterion of having less than 10% cloud cover. Tegal City is covered by 185 x 185 km Landsat 8/9 scene. To enhance the variability of the analysis, we also included conditions similar to a heatwave definition, but adjusted the duration of the increasing temperature to 2 days.

Table 4: Landsat 8/9 Images Dates Used

Heatwave Start Date	Heatwave End Date	Landsat Image Date
≥ 3 Days with ≥ 31.48 °C		
2023-09-25	2023-09-30	2023-09-23
2023-10-06	2023-10-09	2023-10-09
2023-10-15	2023-10-18	2023-10-17
2023-12-11	2023-12-24	2023-12-12
≥ 2 Days with ≥ 31.48 °C		
2024-09-29	2024-09-30	2024-09-25
2024-10-29	2024-10-30	2024-10-27

4.3. Sentinel-2 Image

The Sentinel-2 MSI Level-2A (L2A) was used to update the land cover class. The product provides orthorectified, Bottom-of-Atmosphere (BOA) reflectance. This means the data has been atmospherically corrected using the Sen2Cor algorithm. According to the official Sentinel-2 Level-2A product specification by the European Space Agency (2023), the Multi-Spectral Instrument (MSI) provides a comprehensive spectral range that supports diverse land monitoring applications through 13 distinct bands. These are organized into three spatial resolutions: four bands at 10m (Blue, Green, Red, and NIR), six bands at 20m (including the specialized "Red Edge" series for vegetation phenology and two Short-Wave Infrared/SWIR bands for moisture and built-up detection), and three bands at 60m dedicated to atmospheric characterization (coastal aerosol, water vapor, and cirrus detection). The Sentinel-2 band specification in this study is specified in Table 5 below.

Table 5: Sentinel-2 Band Specification

Band	Logic Name	Resolution	Primary application in this study
B1	Coastal Aerosol	60m	-
B2	Blue	10m	Bare Soil Index (BSI)
B3	Green	10m	Normalized Difference Water Index (NDWI)
B4	Red	10m	NDVI
B5	Red Edge 1	20m	-
B6	Red Edge 2	20m	-
B7	Red Edge 3	20m	-
B8	NIR (Broad)	10m	NDVI
B8A	NIR (Narrow)	20m	-
B9	Water Vapor	60m	-
B10	Cirrus	60m	Cloud Masking
B11	SWIR 1	20m	NDBI
B12	SWIR 2	20m	BSI

4.4. Land cover map

Land cover map from Tegal City Government was chosen due to its being the most updated one and derived from field observation with a mapping scale of 1:5,000. Orthorectified high-resolution Pleiades imagery with a resolution of 30 cm in 2022 was used as input and as a georeference. The creation of the land cover layer was strictly supervised by the National Geospatial Agency in Indonesia and the Ministry of Agrarian Affairs and Spatial Planning/National Land Agency, and it was used as an important input for the Detailed Spatial Plan of Tegal City. The original dataset was a land use/land cover with an attribute table in Indonesian and then translated into English. The dataset is one vector layer in a *shapefile* and consists of fields such as Theme, Type, Toponym, Source, and Area. The original 'type' field is more detailed, but it was grouped into more general land cover categories for this study.

The classification of land covers was categorized based on the nature of their characteristics: Building types such as Industrial Building, Healthcare Building, Sport Building, Tourism and Entertainment Building, Education Building, Trade and Service Building, Worship Building, Office Building, Residential Building, Defense and Security Building, Social Building, Transport Building, and Utility Building were included as built-up class. Water bodies such as rivers, ponds, and retention basins were categorized as waterbodies. Infrastructures such as Jetties, roads, and paved surfaces were categorized as artificial sealed surfaces. Initially, arable land, sand, and empty plots were categorized as bare soil. Shrubland, Soccer Field, and Cemetery are initially classified as herbaceous cover, which shall be modified into the respective land covers based on their vegetation cover, and the land covered with no vegetation shall be classified as bare soil. Croplands, such as mixed crops, paddy fields, etc., are classified under the crop category. Broadleaved trees came from mangrove areas, gardens, and plantations. Railways, fishponds, and swamps are retained in their original classes due to their specific purposes. This approach helps provide a clearer picture of land cover and environmental conditions.

4.5. Building height

Data on average building heights from the World Settlement Footprint 3D were used to create the LCZ. This dataset was produced using a modified human settlements mask from the World Settlement Footprint, which incorporates Sentinel-1 and Sentinel-2 satellite imagery, digital elevation data, and radar information from the TanDEM-X mission (Esch et al., 2022). The data is originally formatted as GeoTiff and has a geometric resolution of 2.8 arcseconds, equivalent to about 90 meters at the equator. Average building height values were then processed for the built-up land cover class and exported as a raster file once more.

5. Methodology

This section outlines the comprehensive workflow for estimating the SUHI effect in Tegal City. The methodology is divided into four distinct phases: 1) Data Pre-processing, 2) Data Creation, 3) Modeling, and 4) Validation. The general workflow is illustrated in Figure 5.

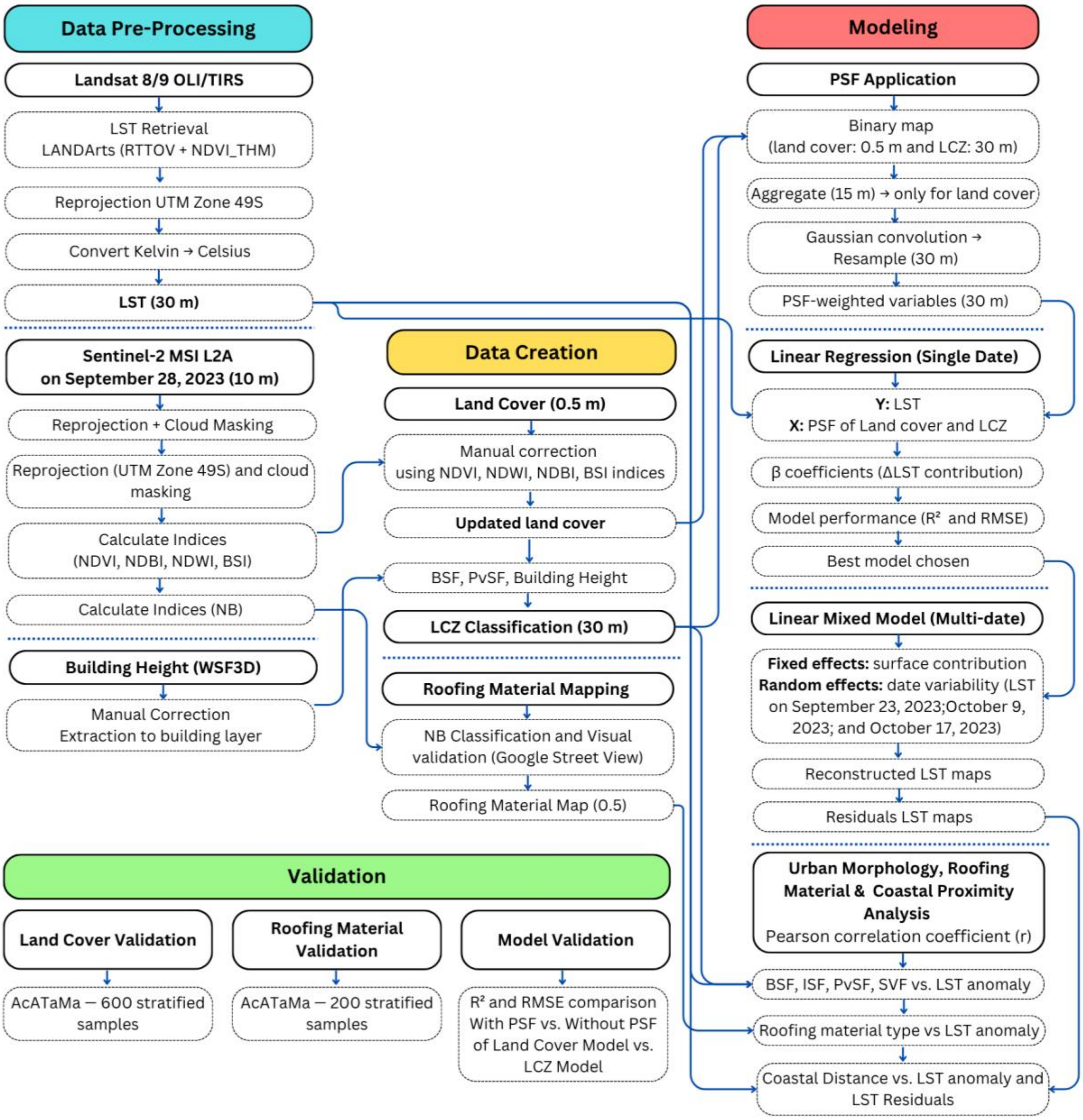

Figure 5: Flowchart of the Overall Methodology

Data creation and analysis were conducted using a combination of specialized geospatial software and programming environments. Primary 2D spatial processing and visualization were performed in Quantum Geographic Information System (QGIS) (QGIS Development Team, 2024). Core analytical tasks were implemented in Python within the Visual Studio Code desktop environment. The technical implementation used several key libraries: NumPy (Harris et al., 2020) for numerical array operations, Rasterio (Gillies et al., 2013) and rioxarray (Snow et al., 2023) for raster data management, and GeoPandas (Jordahl et al., 2020) for vector data processing. The main library used for retrieving LST was LANDARTs (Tardy et al. (2016).

Statistical modeling of regression was carried out using the linear model from the scikit-learn package (Pedregosa et al. 2011), and the graphic visualization was produced using Matplotlib (Hunter 2007). Other statistical modeling was developed in order to create predictive LST using Linear Mixed-Effects Models (LMM) with the statsmodels library (Seabold & Perktold, 2010), in which fixed effects and random effects were incorporated. This was performed in order to improve prediction reliability using multi-temporal variation and sensor-specific physical characteristics. The landscape metrics were calculated using R and RStudio (Posit Team 2024) to support the spatial-metrics perspective.

5.1 Landsat Processing

The processing of Landsat data focuses specifically on the Landsat 8/9 OLI/TIRS Level-1 products. This Level-1 product is selected based on the geographic context of Tegal City, which is a coastal area with high humidity levels, so that the LST retrieved will properly take into account emissivity and water vapor correction.

After downloading the Landsat dataset (Earth Resources Observation and Science Center, 2020), processing is performed using LANDARTs, which is an automated Python tool developed by Tardy et al. (2016) for LST retrieval, combining ERA-Interim global atmospheric data with the MODTRAN radiative transfer model to apply a spatialized grid of correction parameters so that corrections can be performed over entire images rather than over local points only. The process involves emissivity estimation per pixel using NDVI and application of Plank's law inversion for LST derivation, producing 30 m resolution maps within ~5.5 min, with the derived LST output in GeoTIFF format in Kelvin, which then is converted to degrees Celsius. Moreover, re-projection is done to align it with the rest of the data, using WGS 84 coordinate system with UTM Zone 49S (EPSG:32749).

5.2 Land Cover Updating

The output of updating land cover is a raster layer at a resolution of 0.5 m. This updated land cover was derived from the original Land Use/Land Cover of Tegal City 2022, presented in the previous chapter. For higher resolution, highly accurate LULC data were produced by updating from the condition, which was very close to the time of the heatwave occurrence on September 23, 2023. A reasonable match date, Sentinel-2 has been chosen on September

28, 2023. Multispectral images at a resolution of 10 m of Sentinel-2 were acquired on the chosen date.

The vector layer was updated using several thresholding indices for each class (built-up area, vegetation, water), so that the condition is very close to the actual and can effectively measure LST change. Some indices applied for updating land cover are NDBI, NDVI, NDWI, and BSI. The equations and thresholds of the indices applied for updating land cover were listed in Table 6.

Table 6: Indices Threshold for Land Cover Updating

Updated Class	Indices Used and Data Used	Value Threshold
Midrise Built-up and Lowrise Built-up	$NDBI = \frac{\text{SWIR} - \text{NIR}}{\text{SWIR} + \text{NIR}}$	>0
Herbaceous Cover	$NDVI = \frac{\text{NIR} - \text{RED}}{\text{NIR} + \text{RED}}$	0.2 – 0.44
Broadleaved Trees		0.45 – 0.67
Crop with Vegetation		0.2 – 0.44
Crop without Vegetation		-0.19 – 0.19
Fish Pond with Water	$NDWI = \frac{\text{Green} - \text{NIR}}{\text{Green} + \text{NIR}}$	>0.27
Fish Pond without Water		<0.27
Swamp	$BSI = \frac{(\text{SWIR} + \text{Red}) - (\text{NIR} + \text{Blue})}{(\text{SWIR} + \text{Red}) + (\text{NIR} + \text{Blue})}$	>0.08

5.3 Rule-based Local Climate Zone Classification

The rule-based classification method has been selected due to the availability of a high-resolution land cover map, as well as findings from research conducted by Gál et al. (2016), alongside Wicki and Parlow (2017). These studies evaluated and compared different LCZs mapping approaches and concluded that integrated classification, which utilizes multi-source data such as land cover classification, achieves greater accuracy than methods relying solely on high-resolution imagery, such as those employed in the World Urban Database and Access Portal Tools (WUDAPT).

The LCZ classification is based on a set of rules referring to the LCZ framework specified in the previous chapter explaining LCZ by Stewart and Oke (2012), but adapted to reflect the urban form of Tegal, Indonesia. Instead of directly adopting the threshold, this method integrates high-resolution land cover (50 cm), building height data, and vector-based building footprints, which are resampled to a consistent 30 m grid. Some urban indicators, such as BSF, PvSF, and building height, are computed and spatially smoothed to capture neighborhood-scale characteristics (90–180 m), ensuring that the classification reflects realistic urban patterns rather than pixel-level noise.

Afterward, a hierarchy of rule-based classification is implemented, in which LCZ classes are assigned levels of priority. The more distinct classes (for example, compact mid-rise and large industrial) are assigned first to reduce the possibility of them being mistaken for less distinct classes. For example, LCZ 2-Compact mid-rise is defined prior to other categories as a relatively not too tall building height (10m) plus a relatively dense built-up fraction (>35%), which could already be highly considerable to the context of Tegal, which is less prone to having high-rise building structures. Similarly, LCZ 8 (large low-rise) is identified using building footprint size (>800 m²) and area fraction thresholds, capturing industrial or warehouse-type structures typical in Indonesian secondary cities. Other thresholds are also adjusted, such as height (10 m instead of higher values), and vegetation fraction (more relaxed PvSF limits) are modified to better represent Tegal's urban environments. Table 7 below is the classification priority and thresholds used in this study.

Table 7: Priority Classification and Threshold for LCZs Mapping

Priority	LCZ Class	Criteria (Thresholds)	Reason for Priority
1	LCZ 2 – Compact Mid-Rise	Height ≥ 10 m and BSF > 0.35	Captures the most thermally significant dense urban areas and must not be misclassified as low-rise
2	LCZ 8 – Large Low-Rise	BSF > 0.25 and Height < 10 m AND PvSF < 0.45	Identifies industrial/warehouse zones using large footprints typical in Tegal
3	LCZ 3 – Compact Low-Rise	BSF > 0.40 and Height < 10 m	Represents dense residential kampung areas
4	LCZ 6 – Open Low-Rise	BSF > 0.15 and PvSF > 0.30	Mixed built and vegetation typical of suburban areas
5	LCZ 9 – Sparsely built	BSF > 0.05 and PvSF > 0.60	Low-density settlements with dominant vegetation
6	Natural Classes	Based on land cover mode (trees, low plants, water, bare soil, paved)	Assigned last to remaining pixels

5.4 Roofing Materials Data Creation

The roof material layer was developed based on prior research on roofing material preferences in Indonesia by Ginting and Novrial et al. (2024). According to the research, the most common roofing materials in Indonesia include clay tile, metal tile, concrete tile, shingle, tin, reinforced concrete (dak), polycarbonate, and PVC (polyvinyl chloride), as also referenced in earlier work by Sudarmadj (2014). To validate the roof type in Tegal, an interview was carried out with Teguh Sugiartono, Head of Human Settlement, Department of Public Works and Spatial Planning of Tegal City Government, who stated that all of these materials except shingle roofs are present in Tegal City according to building permit records.

Using the building layer, the roof materials are then filled with roof material type based on spectral characteristics derived from remote sensing data. Specifically, a Brightness Index (BI) was used to represent the overall reflectance of surfaces from the red (R), green (G), and blue (B) bands, which is commonly applied to identify high-reflectance features (Kior et al., 2024). To improve discrimination of highly reflective materials such as metal roofs, the index was modified into a Normalized Brightness Index (NB). This modification increases the separability of roofing materials by accounting for differences in spectral response between visible and near-infrared wavelengths. The NB is defined as:

$$NB = \frac{\mathrm{R} + \mathrm{G} + \mathrm{B}}{\mathrm{NIR}}$$

In addition, the visual interpretation using high-resolution orthophotography satellite imagery in 2022 is used, and classification results were validated through cross-checking Google Street View.

For classification purposes, similar materials were grouped into broader categories. Metal and tin roofs are grouped into metal, while concrete tile roofs and dak concrete roofs are grouped into concrete roofs. A threshold of NB value between 2.39 and 3.78 was applied to classify metal roofing materials. This threshold is carefully adjusted to local conditions because some metal roofs may have lower reflectance due to weathering, dirt accumulation, or coating, which can reduce their spectral brightness. Other types of roof materials were classified based on the color and visual representation.

5.5 SUHI Intensity Pattern Analysis

To identify persistent Surface Urban Heat Island (SUHI) patterns in Tegal City, the raw Landsat land surface temperature (LST) values were standardized using Z-score normalization. By normalizing the data for each date independently, we can isolate the consistent urban thermal signature caused by surface characteristics. This method allows for comparison of thermal anomalies across different dates. For each Landsat acquisition date, individual LST pixel values were converted to Z-scores (standard normal variates) according to:

$$Standardized\ LST\ (Zi) = \frac{LSTi - \ LST\ Mean}{Standard\ Deviation\ LSTi}$$

In this context, $LSTi$ is the LST on single date, $LST\ Mean$ is the average LST of 6 heatwaves date (09 October 2023, 12 December 2023, 17 October 2023, 23 September 2023, 25 September 2024, 27 October 2024) and $Standard\ Deviation\ LSTi$ is the standard deviation of LST for that date, representing how much LST varies around the mean. To account for LST variability across multiple acquisition dates and identify persistent thermal anomalies, the standardized LST values were averaged across all six acquisition dates

$$Average\ Standardized\ LST\ = \frac{(Z_1\ +\ Z_2\ +\ Z_3\ +\ Z_4\ +\ Z_5\ +\ Z_6)}{6}$$

This normalization centres the LST distribution for each date at zero. The result is classified as follows: strong cool islands (Z ≤ -2°C); moderate cool islands (Z = -2 to -1°C); thermally neutral areas (Z = -1 to +1°C) with mixed land cover; moderate heat islands (Z = +1 to +2°C); and strong heat islands (Z ≥ +2°C).

5.6 Linear Regression

Linear Regression was used in this study to determine how the features of the urban surface affect LST. LST is used as the dependent variable, and then derived either from land cover fractions or LCZ classes as independent variables to find out the influence of each type of surface on temperature. Based on these results, it was used as an input for the Linear Mixed Model to predict LST for multiple dates.

In this framework, LST is expressed as a function of the contributions of different land cover or LCZ classes, weighted by their spatial proportions and adjusted for the Point Spread Function (PSF). The model can be written as:

$$LST_{pixel} = \Delta LST + \sum_{i=1}^{n} (PS\,F_i \cdot \beta_i)$$

where ΔLST represents the mean LST for the study area, PSF_i is the proportion of surface type (land cover or LCZ) i within the pixel, and β_i is the regression coefficient representing the contribution of each surface type to LST.

To implement this, a linear regression function in Python was used from the scikit-learn library, specifically the LinearRegression model. The observed LST from Landsat is first processed and centered by subtracting the mean, allowing the model to focus on temperature deviation rather than absolute values. Therefore the output formula expresses the LST in relation to the average temperature, plus the amount related to each surface type.

In the Land Cover model, 0.5-meter resolution high data was aggregated to 15 meters, then resampled to 30-meter resolution to match the Landsat data. PSF was applied during the aggregation. The detailed process is further explained in the PSF sub-section. In the LCZ model, the process is slightly different. Since LCZ data is already at 30-meter resolution, it directly matches the Landsat LST. Therefore, no spatial aggregation is required, and only the PSF is applied to account for spatial mixing between neighboring pixels. After preparing the data, all PSF-weighted variables are stacked into a matrix and used as input for the regression model. The regression then estimates coefficients that represent the temperature contribution of each surface type or LCZ class.

5.7 Linear Mixed Models

The regression approach is limited to individual dates and does not explicitly account for temporal variability caused by changing atmospheric conditions. To address this limitation, a linear mixed model is employed to generalize the relationship across multiple heatwave events. In the linear mixed model framework, the effects of land cover or LCZ classes are treated as fixed effects, while the variability between dates is represented as a random effect through the mean LST for each date. The model is expressed as:

$$LST_{pixel,d} = \Delta LST_d \times \sum_{i=1}^{n} \left(\Delta LST_i \cdot PSF_{i,pixel}\right) + \epsilon_{pixel,d}$$

where $\Delta \mathrm{LST}_d$is the mean LST for date d, ΔLST_i represents the normalized contribution of surface type i, $PSF_{i,pixel}$is the proportion of that surface within the pixel, and $\epsilon$is the residual error term.

This formulation allows the model to maintain stable surface-specific effects across time, while accounting for date-specific temperature variability, resulting in a more robust reconstruction of LST across multiple heatwave events.

5.8 Application of Point Spread Function (PSF)

The PSF was applied to match with the LST derived from satellite imagery, such as Landsat 8/9, which is shown blurred. Each pixel does not represent a purely local measurement, but it incorporates thermal radiation contributions from surrounding areas, as illustrated in the Landsat pixel representation in Figure 6 (Radoux et al., 2025). This sensor-induced mixing effect means that the recorded temperature at a given location is spatially diffuse, potentially obscuring the true relationship between land cover and temperature. Such blurring has long been recognized as a major source of uncertainty in remote sensing analysis (Huang et al., 2002). More recently, Radoux et al. (2025) demonstrated that explicitly accounting for the PSF significantly improves model performance, increasing the coefficient of determination (R^2) from 0.57 to 0.81 and reducing the Root Mean Square Error (RMSE) from 2.35 °C to 1.6 °C. Their findings confirm that, once this spatial diffusion is properly accounted for, land cover becomes a much clearer driver of LST variability.

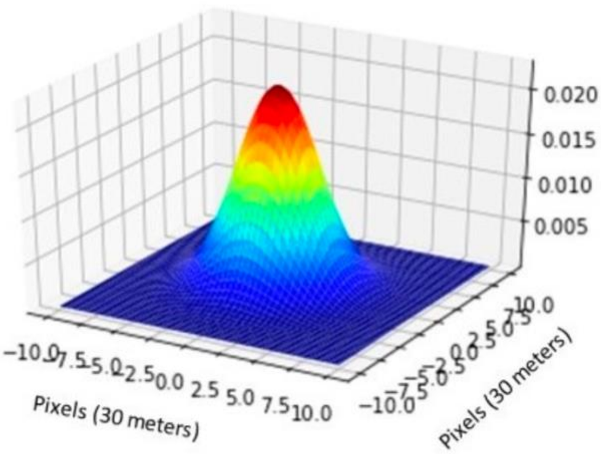

Figure 6: Landsat PSF 3D Illustration (Radoux et al., 2025).

In this study, the PSF is used to represent this spatial diffusion process, which in this case is performed through a Gaussian-based convolution of the land cover data. The Gaussian kernel is used because it produces a smooth, distance-based decay, mimicking the way heat from surrounding pixels influences the center pixel. The choice of sigma (79.5 m) dictates the scale of spatial influence, whereas the kernel size (2121, which at a 30m pixel resolution equates to 630m 630m in spatial coverage) insures most of the Gaussian distribution is encompassed. A 300m buffer is then imposed around the edges of the grid to avoid edge effects, and a normalization procedure with a blurred mask removes the bias near the no-data regions, and this border is subsequently trimmed off. Prior to applying the PSF, the land cover data must be up-sampled to 15m (mean function) and then resampled back to 30m (nearest neighbor). This step serves to appropriately scale the land cover data to better correspond with the LST data. The 15m mean aggregation averages out noise and represents small sub-pixel features that would not be captured otherwise. The nearest-neighbor resampling of this averaged surface back to 30m resolution preserves these values without introducing extra smoothing. This entire process is graphically represented below in Figure 7.

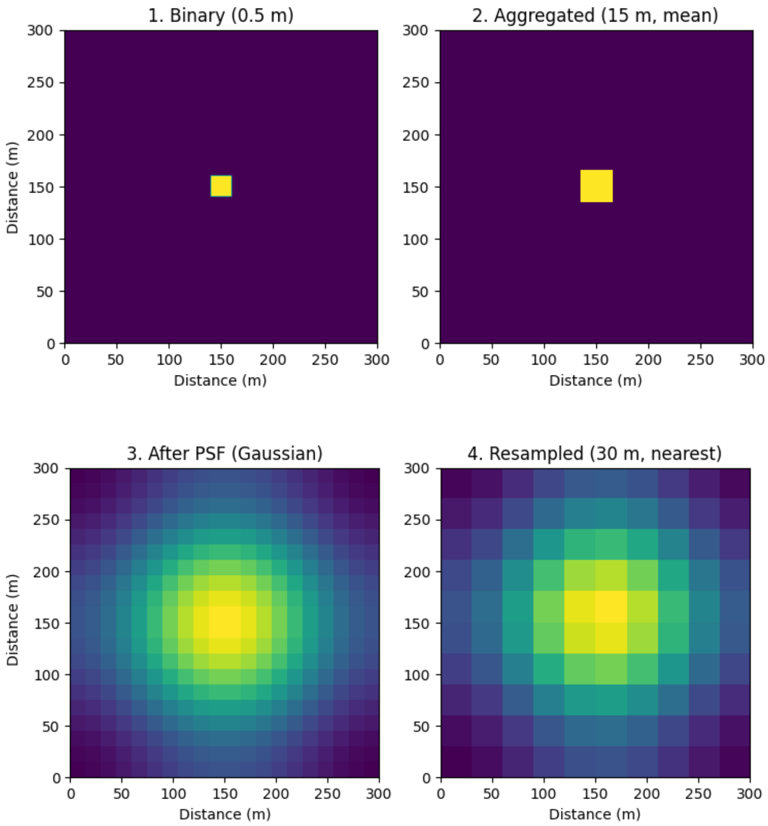

Figure 7: Schematic of the Point Spread Function (PSF) spatial resolution at 30 m resolution. (a) A 0.5 m binary land cover map shows each surface type (b) A Gaussian PSF kernel (σ = 79.5 m; 21 × 21 pixels at 30 m; coverage ≈ 630 × 630 m) (c) PSF-convolved land cover fractions at 15 m, showing the weighted surface contribution of each cover type (d) Final aggregated fraction map resampled to 30 m.

5.9 Impact Assessment of Urban Morphology, Material Properties and Coastal Proximity

This study performed a retrospective multi-temporal spatial analysis to investigate urban spatial structure on SUHI intensity for Tegal City. In the main methodology, time series LST data acquired from 6 Landsat-8/9 TIRS data acquisitions over Tegal City from 2023 to 2024 were analyzed with the high-resolution urban morphological variable.

LST values were extracted using a zonal sampling technique across diverse urban contexts characterized by varying BSF, ISF, PvSF, and SVF, along with roofing material fractions. SVF was determined using 8-m-resolution Digital Elevation Model (DEM) data for Tegal City, using the SAGA GIS plugin. Using 16 directional sectors (with a step of 22.5 degrees) and the multi-cell method in the estimation of the obstructing angle to increase the accuracy. The relationship between morphological drivers (x) and the resulting thermal response (y) was measured using the Pearson correlation coefficient (r), calculated as follows:

$$r = \frac{\sum(x_i - \bar{x})\,(y_i - \bar{y})}{\sqrt{\sum(x_i - \bar{x})^2 \sum(y_i - \bar{y})^2}}$$

Here, x_i and $y_i$represent the individual sample values for urban fractions and mean LST, respectively, while $\bar{x}$ and $\bar{y}$ are their corresponding averages. By aligning multi-date satellite observations with fixed morphological indicators, this method can effectively capture the changing thermal response of the urban environment. It also helps identify the main spatial patterns that cause localized heat buildup. The thermal metric used in the correlation analysis was the LST Anomaly. This anomaly is the difference between each sample's LST and the mean LST of the study area for each acquisition date, calculated as:

$$LST\ Anomaly = LST\ sample\ -\ Mean\ LST\ study\ area$$

This normalization accounts for day-to-day changes in absolute temperature. It allows for consistent comparisons of thermal sensitivity across various acquisition dates and atmospheric conditions.

6. Results

This chapter presents the results of the analysis and is organized into seven sections: LST distribution; SUHI intensity patterns; the influence of land cover and LCZ on surface temperature; model validation; and the fine-scale impact assessment of urban morphology, roofing materials, and coastal proximity on LST anomalies.

6.1 LST Distribution

The results of LST for September 23, 2023, displayed in Figure 8, were selected as the baseline for the linear regression model since this date closely aligns with the original government land cover data used as input. Overall, the LST distribution through visual observation from the map indicates the presence of "cooling sinks" in the western part of Tegal City, specifically in the Sub-district of Muarareja, Margadana, Cabawan, Krandon and Kaligangsa, where the areas are characterized by fish ponds, crops, and swamps. While the eastern part is characterized by hotspots showcasing the urban built-up environment.

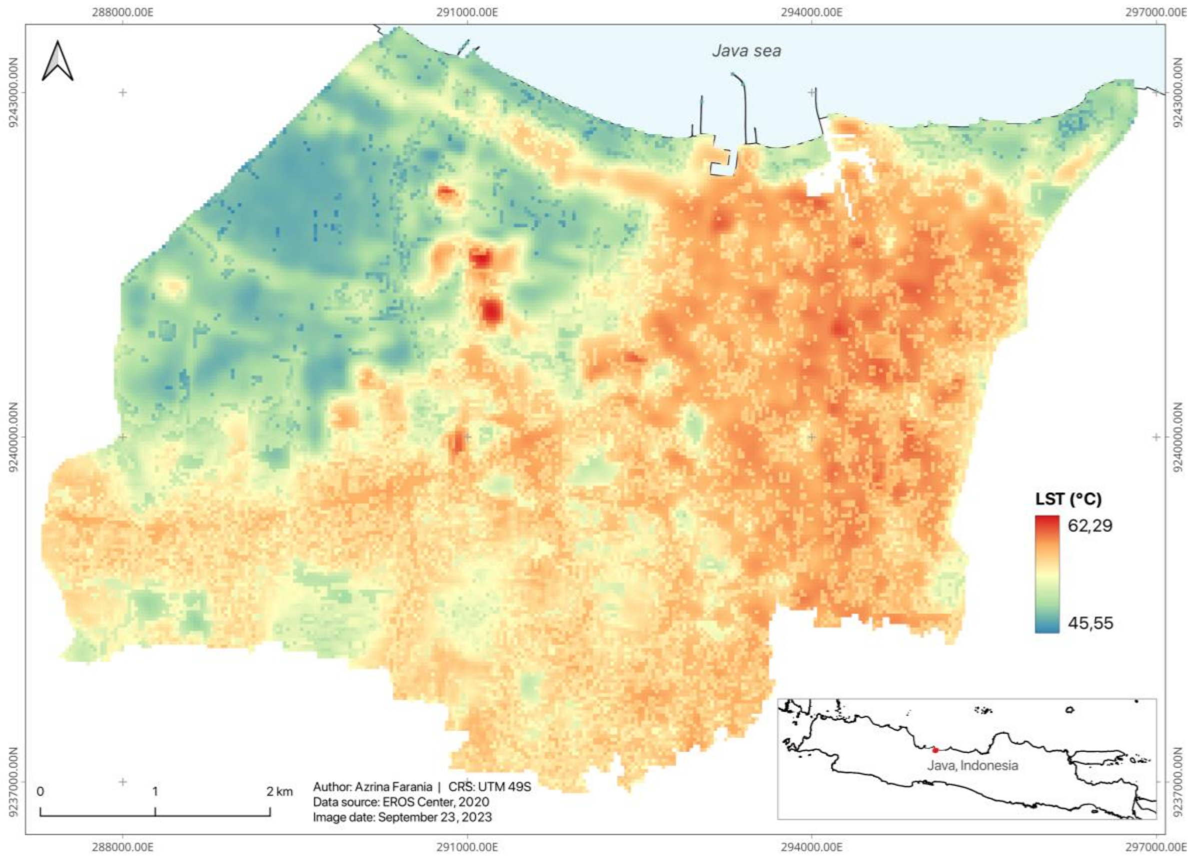

Figure 8: LST distribution in Tegal City on 23 September 2023, retrieved from Landsat 8/9 TIRS using the LANDARTs tool. Higher temperatures (°C) are found in built-up areas. In contrast, vegetation, water bodies, and the coastal zone show much lower values.

Figure 9 shows the LST across several heatwave dates. To help compare these dates, a standard color scale is used. The scale ranges from a high of 62.83 °C, recorded on October 17, 2023, to a low of 41.9 °C, noted on September 25, 2024. The detailed raw LST values in Appendix Figure A.

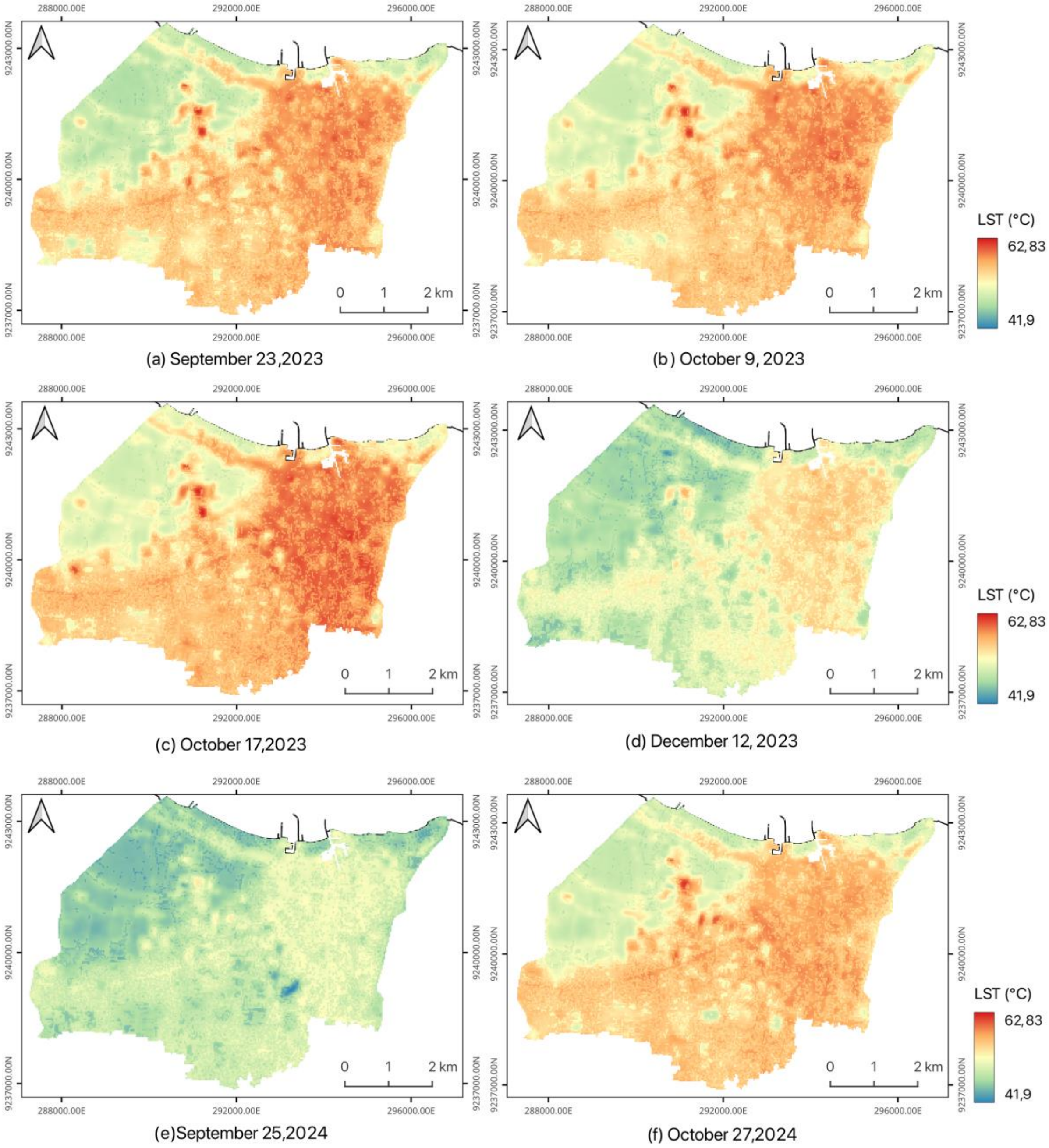

Figure 9: LST Distribution During Multi-Heatwave Periods in Tegal City using standardized color scale ranges on a) September 23, 2023, b) October 9, 2023, c) October 17, 2023, d) December 12, 2023, and e) September 25, 2023, f) October 27, 2024.

Statistical analysis of the processed LST across the whole study area, shown in Figure 10, reveals significant thermal stress during the identified heatwave periods. For each acquisition date, the spatial mean LST ranged from 48.8°C to 55.6°C, representing the warmest pixels recorded across the entire study area on that date. Conversely, spatial minimum temperatures (cooling sinks) ranged from 41.9°C to 49.6°C. The highest recorded pixel value reached 62.28°C on October 17, 2023. The temperature differential (ΔT = Max − Min) reveals the magnitude of urban thermal heterogeneity, ranging from 12.2°C to 16.7°C, with the largest thermal variation (+16.7°C) observed on September 23, 2023. The standard deviation of LST, computed spatially per date, ranged from 2.0°C to 3.3°C, reflecting a fragmented thermal environment dominated by extreme hotspots.

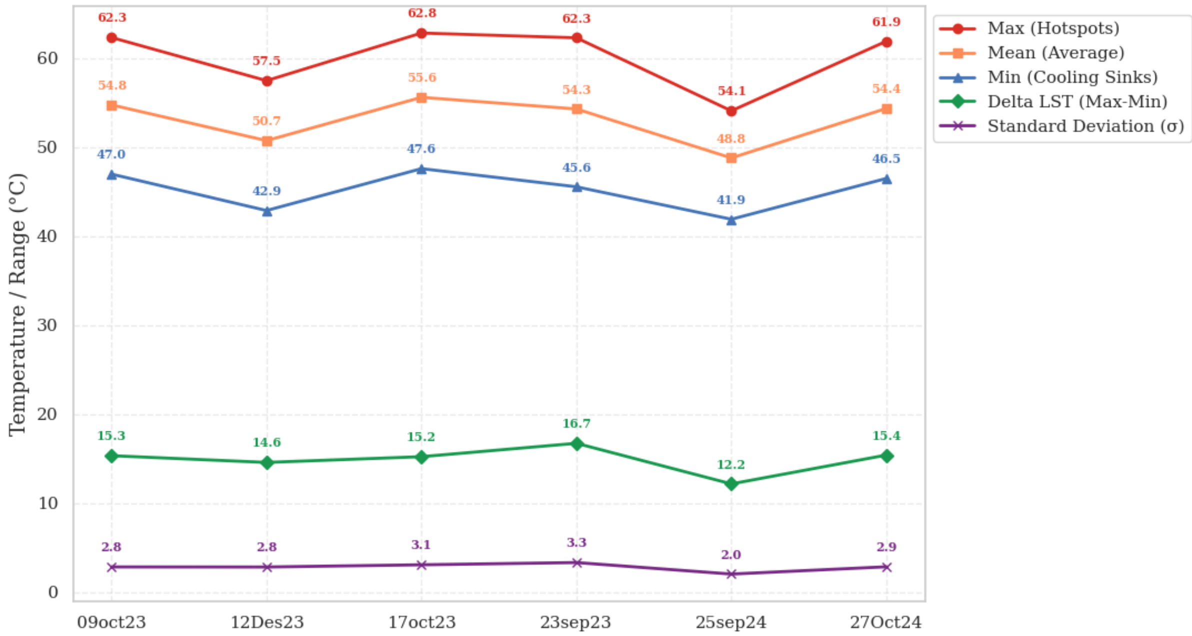

Figure 10: LST statistics across six heatwave dates in Tegal City (2023–2024), derived from Landsat 8/9 TIRS imagery. Lines show maximum (hotspots), mean, minimum (cooling sinks), LST range (Max−Min), and standard deviation (σ) in °C.

6.2 SUHI Intensity Patterns

In order to identify ongoing patterns of SUHI, LST data from various Landsat acquisitions were compiled. The 6 input images of LST shown in Figure 9 were normalized by the average and standard deviation of each image date to account for differing weather conditions at different times and to enable comparison of thermal intensity across dates. Average normalized Land Surface Temperature values were compiled, and the ongoing urban warm and cool zones in Tegal City are mapped in Figure 11 below.

The distribution of SUHI intensity in Tegal City revealed a wide spread of thermal differences; several large warm zone areas of urban heat islands were apparent in the central and eastern part of Tegal City. Moderate heat islands, marked by orange areas (z = +1 to +2), make up 15.5% of the study area and are mainly found in the urban core, particularly in the Sub-districts of Tegal Sari, Mintaragen, Kraton, Pangung, and Kejambon. In contrast, the peripheral and western districts, which include Muarareja, Pesarungan Lor, Margadana, and Kaligangsa, show moderate to strong cooling patterns, indicated by light to dark blue areas (z ≤ -1). This cooling is likely linked to more vegetation and lower building density. The coastal districts and western fringes exhibit cooler surface temperatures (20.4%), with strong cool islands (Z ≤ −2) representing a negligible fraction and combined with moderate cool islands (Z = −2 to −1). The remaining 63.8% of the city is thermally neutral, and less than 1% exhibits strong heat signatures (Z > +2), indicating moderate rather than severe urban thermal divergence.

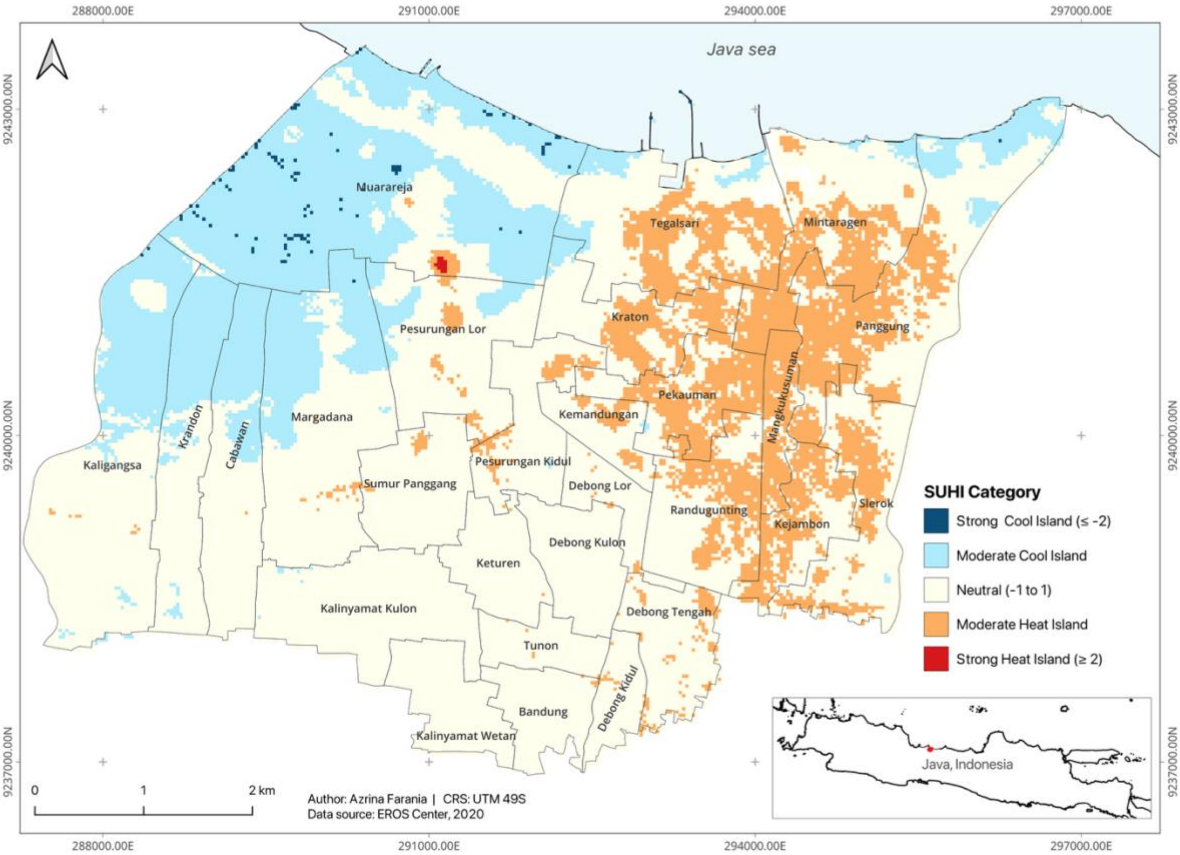

Figure 11: Spatial distribution of SUHI intensity in Tegal City derived from 6 LST images on heatwave dates, classified into five categories from Strong Cool Island (<-2°C) to Strong Heat Island (≥ 2°C).

6.3 Land Cover and SUHI

The updated land cover (see Figure 12) reveals that Tegal City's land cover is characterized by a balance between agricultural-aquacultural activities and urban development. The land cover type proportions in Table 8 showed that herbaceous cover and built-up areas dominate the landscape at 29.10% and 21.94% respectively, while aquaculture features (fish ponds) comprise 15.14% of the total area, reflecting the city's agricultural heritage. Vegetation cover, including herbaceous areas, broadleaved trees, and crops, accounts for approximately 48.00% of the city, whereas urban infrastructure (low-rise, midrise, and sealed surfaces) represents 25.86%, with remaining areas comprising bare soil (2.58%), rail networks (0.44%), and non-vegetated cropland (1.97%). This composition indicates that Tegal City maintains significant agricultural and aquacultural activities integrated with moderate urban expansion, characteristic of a small secondary Indonesian city transitioning between rural and urban land uses.

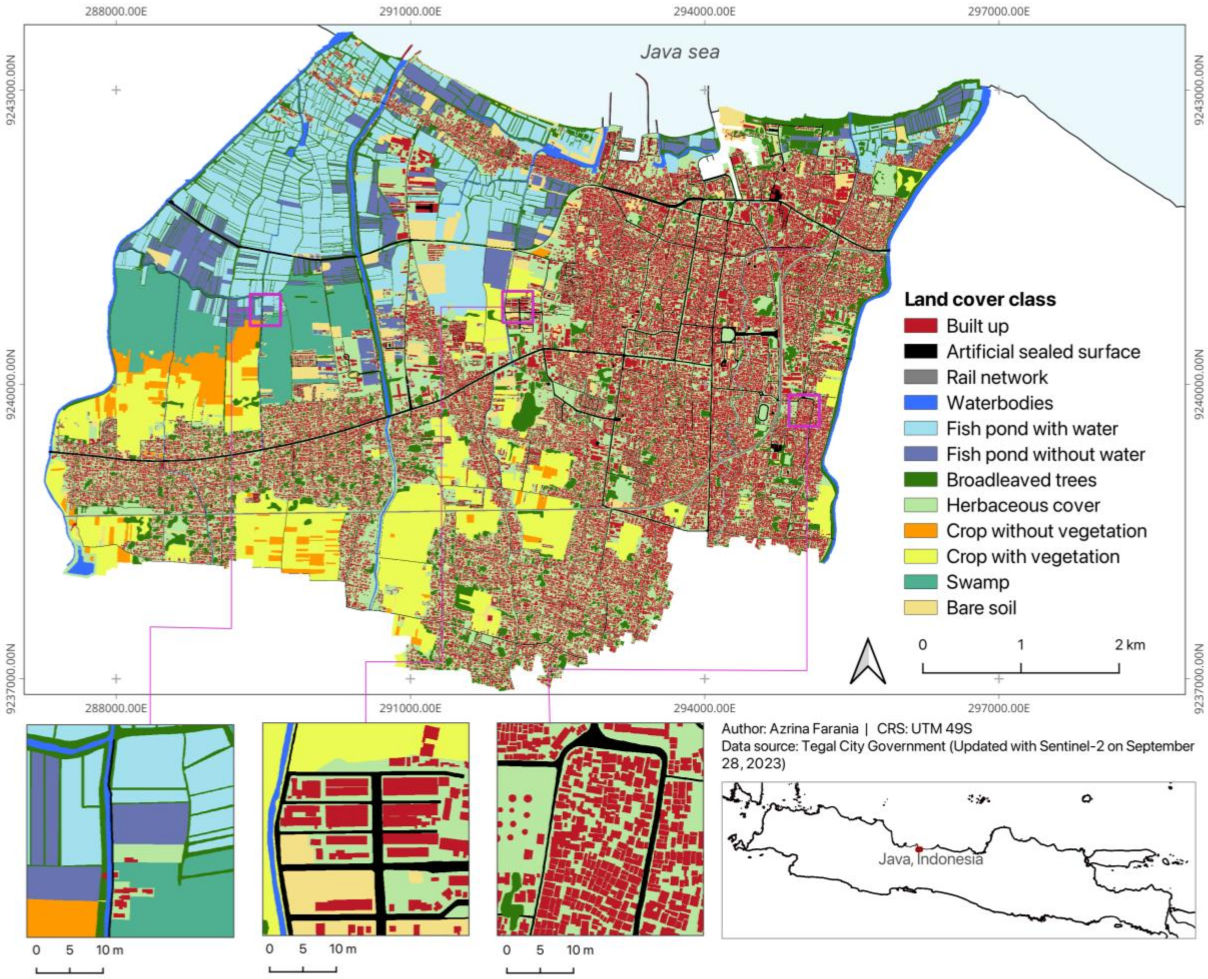

Figure 12: Land cover map of Tegal City at 0.5 m resolution comprising 12 classes mapped from Tegal City Government data and updated using Sentinel-2 (28 September 2023). Insets show classification detail in representative areas: sparse built-up with crops and fish ponds (left), grid-patterned urban blocks (middle), and dense residential (right).

Table 8: Land Cover Type Coverage and Model Performance

Land Cover Class	Coverage (%)
Built up	21.94
Artificial sealed surface	3.92
Rail network	0.44
Waterbodies	2.01
Fish pond with water	10.97
Fish pond without water	4.17
Broadleaved trees	8.76
Herbaceous cover	29.10
Crop without vegetation	1.97
Crop with vegetation	10.09

Land Cover Class	Coverage (%)
Swamp	3.99
Bare soil	2.64

Linear regression analysis was performed to quantify the influence of land cover type on LST. Binary maps for each land cover class, as shown in Appendix Figure B, were used to create PSF layers. All PSF layers were selected as the independent variable and LST as the dependent variable in order to determine the contribution of each land cover class to the thermal properties of the urban environment. R and RMSE of the regression model were 0.84 and 1.345 °C. This means that 83.8% of the variance of LST could be accounted for by the composition of land cover classes, and predictions usually differ from observations by about 1.35 °C. This result shows strong model performance and reliability in linking urban thermal changes to land cover properties.

To calculate the thermal contribution of each land cover class, multiply the standardized regression coefficient (β) by the corresponding PSF layer at the pixel level. This is expressed as: $\Delta T = \beta \times PSF$, where ΔT represents the temperature anomaly contribution and β is the regression coefficient (in °C per unit PSF). The land cover classes that increase SUHI effects, as shown in Figure 13, include rail networks (+10.63°C), artificial sealed surfaces (+8.75°C), built-up areas (+5.79°C), and bare soil (+4.03°C). Rail networks contribute the most to warming due to their metal and stone composition, which effectively absorbs solar radiation. Meanwhile, artificial sealed surfaces reflect the vast road networks and parking areas in the urban center.

Cooling effects are predominantly provided by vegetation and aquatic features, with broadleaved trees showing the strongest cooling at -7.11°C, followed by fish ponds with water (-6.05°C), swamps (-5.50°C), waterbodies (-5.15°C) and fish ponds without water (−4.88°C). Notably, herbaceous cover exhibits minimal cooling (-0.23°C) despite covering 29.10% of the city.

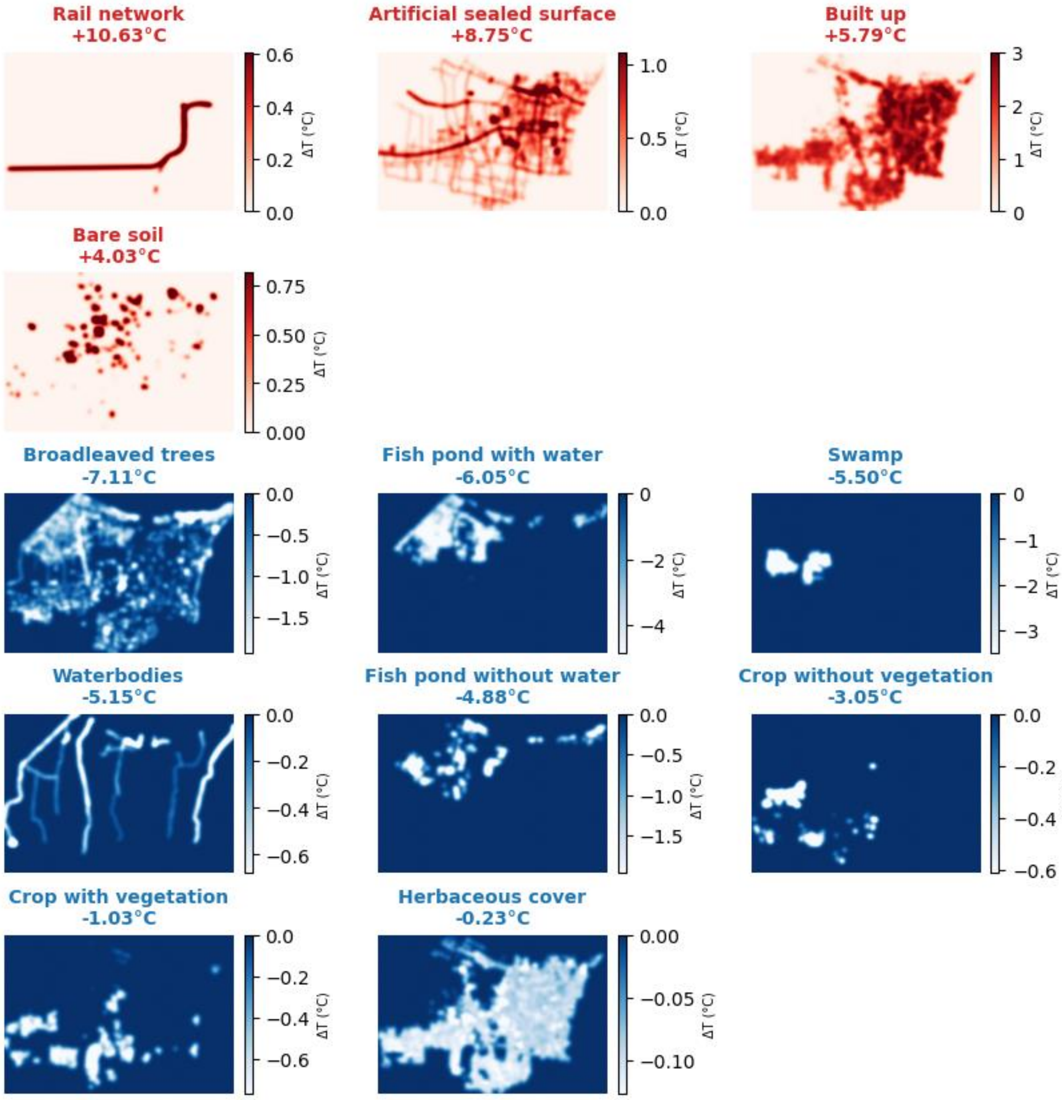

Figure 13: Thermal contribution (ΔT, °C) of each land cover class to LST in Tegal City, derived from the linear regression model. Red tones indicate warming contributions (positive ΔT) and Blue tones indicate cooling contributions (negative ΔT). Each panel shows the spatial distribution of the class contribution across its mapped extent.

6.4 LCZs and SUHI

The LCZ classification shown in Figure 14 was utilizing land cover and building height data (Appendix Figure F), which reveals a distinct urban-rural gradient in surface characteristics across Tegal City. Unlike land cover classification, which identifies individual surface types at pixel resolution, the LCZ system represents a composite classification that groups multiple land cover classes and building characteristics into broader morphological zones. This grouping approach results in larger, more homogeneous zones rather than fine-scale detail, and appears to be coarser than land cover because it aggregates several land cover classes.

Dense mid-rise (LCZ 2, dark red) and dense low-rise (LCZ 3, light red) buildings dominate in the northern coastal region and city center. In these dense areas, there are large patches of large low-rise (LCZ 8, olive) areas, suggesting areas of heavy industry/commercial sites with high density of hard surface area. Moving away from the center, the areas become less dense. These areas consist of open low-rise (LCZ 6, orange) and sparse built-up (LCZ 9, light tan) areas, with a trend of sparse residential development leading into farmland and interspersed natural LCZ types within urban areas.

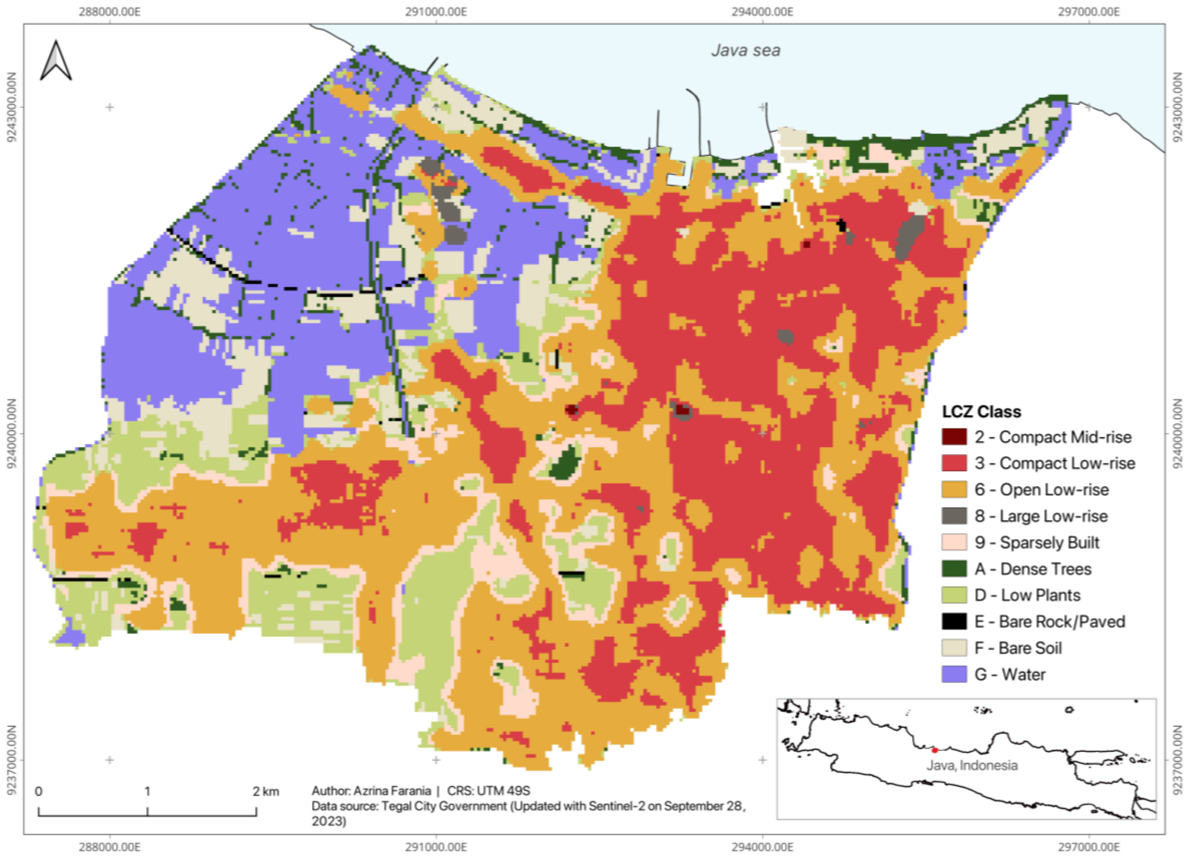

Figure 14: Local Climate Zone (LCZ) map of Tegal City at 30 m resolution, comprising 10 classes classified using a rule-based hierarchical approach based on updated land cover (0.5 m), BSF, PvSF, and building height derived from WSF3D.

The classification of openness or compactness within the built-up classes of the LCZ is primarily driven by the BSF and PvSF. Figure 15 displays a box plot illustrating the distribution of BSF and PvSF across various LCZ built-up classes. Compact mid-rise (LCZ 2) and compact low-rise (LCZ 3) areas typically exhibit high building surface fractions (BSF ≈ 0.47–0.51) with limited vegetation (PvSF < 0.4). In contrast, sparsely built areas (LCZ 9) feature minimal buildings (BSF = 0.10) and extensive pervious surfaces (PvSF = 0.81). Meanwhile, large low-rise zones (LCZ 8), which are characteristic of industrial areas, demonstrate moderate building density and significant impervious paving (PvSF = 0.31), thereby limiting their cooling potential.

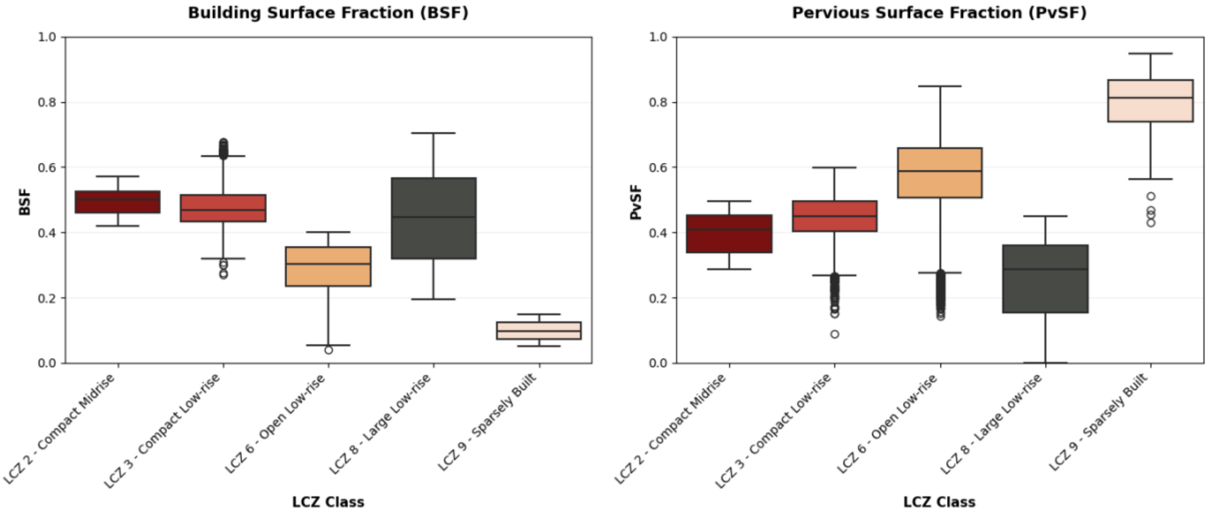

Figure 15: Distribution of BSF (left) and PvSF (right) across urban LCZ classes (LCZ 2, LCZ 3, LCZ 6, LCZ 8, and LCZ 9) in Tegal City. Box plots show the median, interquartile range, and outliers for each class.

The Linear Regression model was used to assess the relationship between LCZs and LST. This analysis followed the same methodology as the Land Cover model by creating a binary map for each LCZ class (see Appendix Figure D) and developing the PSF layer (see Appendix Figure E). The main difference in this process is that it does not need aggregation or resampling, since the LCZ classification matches the 30-meter resolution of the LST data. In this model, the independent variable is the LCZs.

Although land cover and LCZ classifications have the same spatial resolution of 30 m, the LCZ model has slightly lower R and RMSE (0.79 and 1.531 °C, respectively) compared to the Land Cover model and captures approximately 79% of the variation in temperature. The pattern of thermal contributions derived from the LCZ model is similar to the pattern of contributions from the Land Cover model. Among the built-up types in the urban region, the compact type makes the largest contribution to the rise in temperature, with LCZ 2 - Compact Midrise contributing +11.32 °C and LCZ 3 - Compact Low-rise contributing +3.80 °C (see Figure 16). Low-rise open and sparsely built areas cause a much smaller increase in temperature, with contributions of +1.30 and +1.04 C, respectively. Vegetated and water surfaces are significant contributors to cooling. Dense tree area (LCZ A) cools by 8.10 C, and the presence of water (LCZ G) cools by 5.58 C. These results concur with the land cover-derived results and provide evidence for the importance of urban form and vegetation type in the control of land surface temperatures.

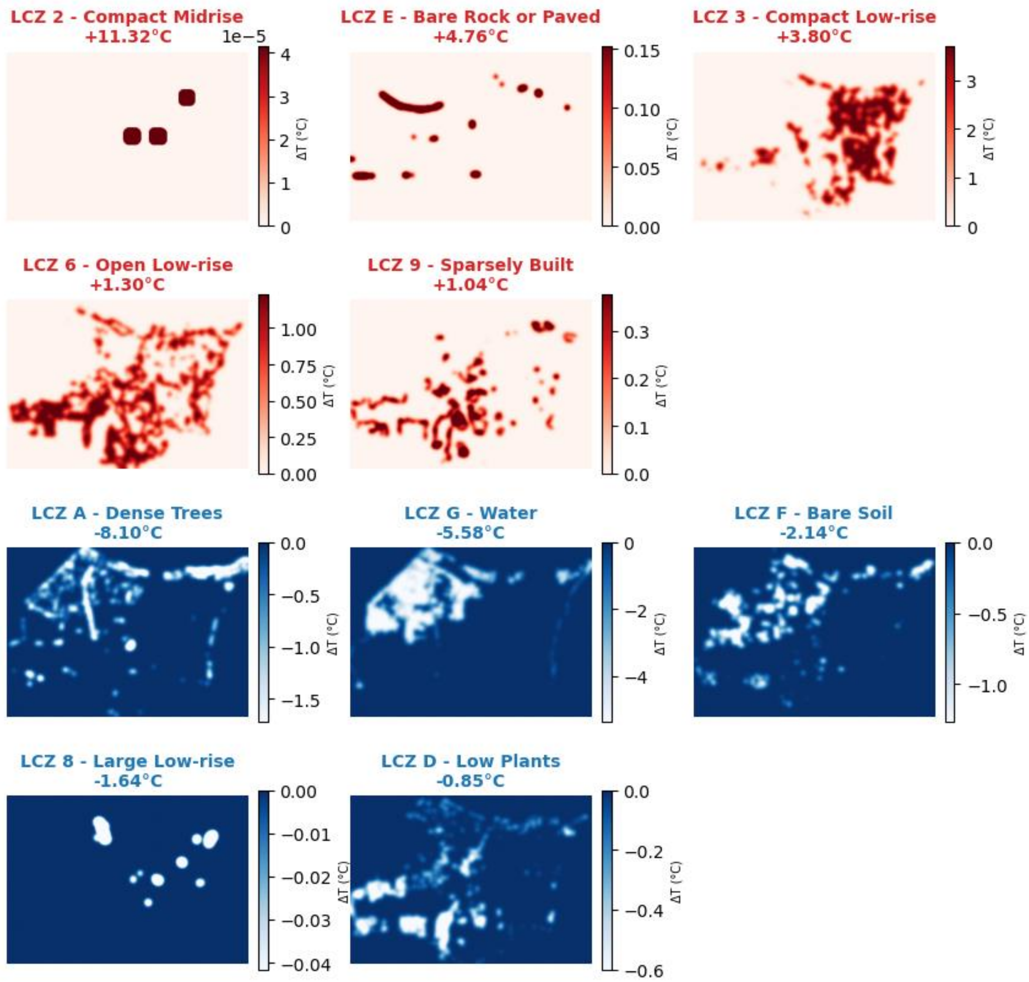

Figure 16: Thermal contribution (ΔT, °C) of each LCZ class to LST in Tegal City, derived from the linear regression model. Red tones indicate warming contributions (positive ΔT) and Blue tones indicate cooling contributions (negative ΔT). Each panel shows the spatial distribution of the class contribution across its mapped extent.

6.5 Linear Mixed Model of Land Cover and SUHI

After obtaining results from both land cover and LCZ regression models, land cover demonstrated superior performance ($R^2 = 0.84$), indicating it is the dominant factor controlling Land Surface Temperature variation in Tegal City. However, the reconstruction produced by the model (Figure 17b) exhibits smoother spatial characteristics because land cover represents a more averaged variable than the land cover zone (LCZ) classification. Therefore, the land cover model effectively reproduces the variations caused by the dominant influencing variables of surface temperature variation. The residuals map (Figure 17c) indicates the accuracy of the model, with estimated errors ranging between 7.33 °C and +9.28 °C. However, the majority of the areas had predictions that lie within ±2C of observed values. Also, the model underpredicts temperature (shown in blue) in some urban centers and overpredicts in some dispersed locations, suggesting some local effects, such as water bodies, specific building material, or atmospheric conditions, cause variations outside land cover influence. It was observed that the patterns of the LST reconstruction across the city look similar for the two acquisition dates of 09 October and 17 October 2023. Land cover-based modeling can provide consistent and reliable estimates of surface temperature variations in Tegal City for the study dates. Results for the other two acquisition dates are shown in Figures G and H (Appendix).

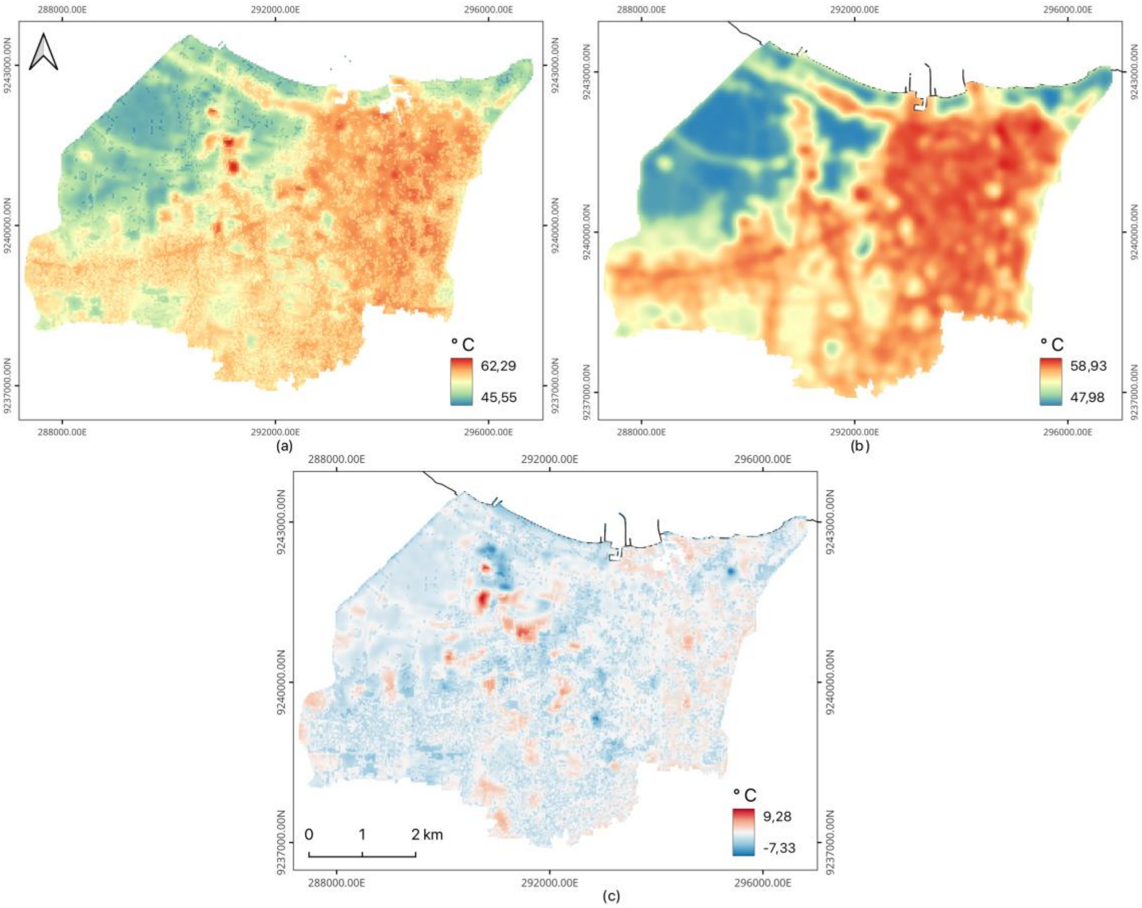

Figure 17: Comparison of (a) observed LST from Landsat 8/9 TIRS (45.55–62.29°C), (b) reconstructed LST from the Land Cover linear mixed model (47.98–58.93°C), and (c) residual LST (observed minus reconstructed, −7.33 to +9.28°C) in Tegal City on 23 September 2023. Positive residuals (red) show areas where the model underestimates LST, while negative residuals (blue) show overestimation.

To better understand where model errors occur and assess whether residuals are influenced by specific surface materials and urban characteristics, the residuals from three acquisition dates (23 September, 9 October, and 17 October 2023) were examined closely (see Figure 18 and Figure 19). The residual maps demonstrate remarkable spatial consistency, with the red-boxed region consistently showing positive residuals (+1 to +9.28°C) where the model underestimates LST, while the blue-boxed region shows negative residuals (−1 to −7.33°C) where it overestimates. This persistent pattern across all three dates suggests systematic biases linked to specific surface properties not fully captured by land cover classification alone. High-resolution satellite imagery from Google Earth acquired on September 23, 2023, georeferenced using Ground Control Points (GCP) from the 2022 orthophoto of Tegal City

(Appendix Figure I), reveals distinct characteristics of the residual temperature patterns. Hot residual spots (red) generally correspond to areas dominated by bare soil (Figure 18), including an open waste dumping site. In contrast, cool residual spots (blue) are associated with open industrial infrastructure and exposed building materials. One of the blue zones (Figure 18a) is located near water bodies and aquaculture areas, while the other (Figure 18b) is surrounded by dense settlement areas. Both locations are characterized by metal roofing and metal-based building materials.

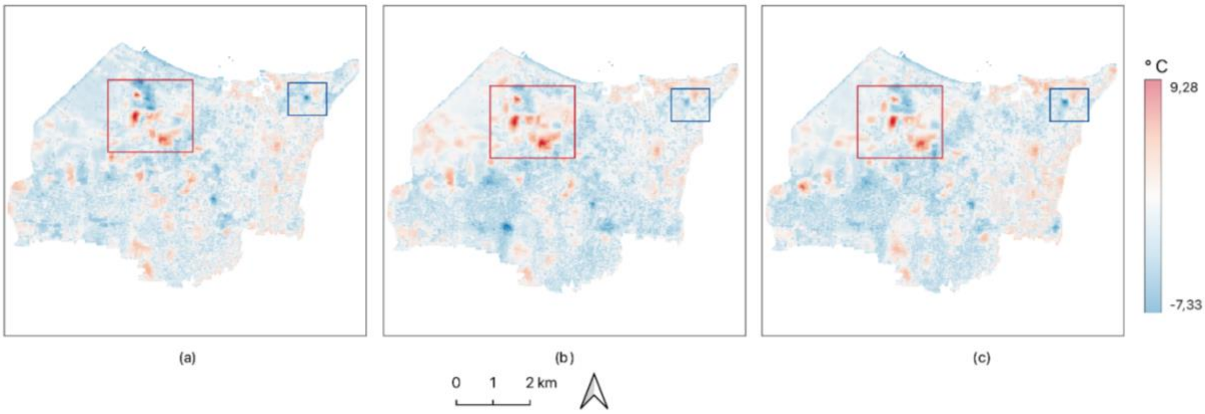

Figure 18: Spatial distribution of LST residuals (observed minus reconstructed) in Tegal City for (a) 23 September 2023, (b) 9 October 2023, and (c) 17 October 2023, using a consistent scale of −7.33 to +9.28°C. Red and blue boxes highlight the areas that consistently show hotspots and cool spots across the dates.

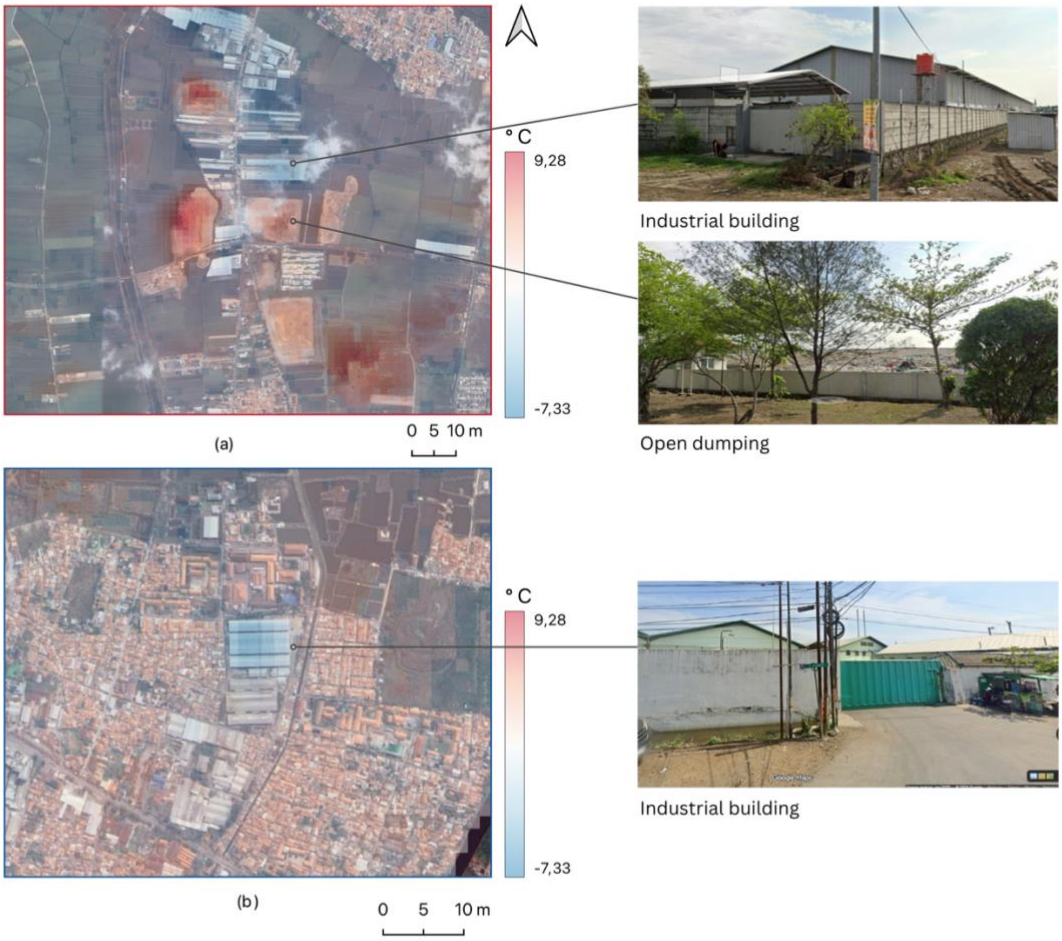

Figure 19: LST residuals are overlaid on Google Earth imagery for 23 September 2023. This shows (a) a hotspot area where large positive residuals, marked in red, align with industrial buildings that have metal roofs and open dumping sites. It also shows (b) a cool spot area where negative residuals, marked in blue, correspond to industrial buildings with metal roofing. Street-level pictures confirm the surface features causing the residual differences.

6.6 Validation and Model Comparison

6.5.1. Land Cover Validation

The accuracy of the land cover map was evaluated using Accuracy Assessment for Thematic Maps (AcATaMa), an open-source QGIS plugin developed by Llano et al. (2024). AcATaMa was selected for its comprehensive and integrated features for accuracy assessment, providing support for sampling design, response design, and estimation within a design-based inference framework, following the fundamental principles outlined by Stehman and Czaplewski (1998) as cited in Llano et al. (2024).

A stratified random sampling design was employed, with a total of 600 samples distributed across 12 land cover classes, where the number of samples per class was allocated proportionally based on the class pixel area percentage (see Appendix Table A), and fully labelled through reference data interpretation. Accuracy metrics were calculated using the stratified estimator, following the methods recommended by Olofsson et al. (2014) as cited in

Llano et al. (2024). The main reference data was an orthophoto image from 2022, derived from Pleiades Imagery (Tegal City Government, 2022) (see Appendix Figure I). This was supplemented by Google Earth satellite imagery obtained on 23 September 2023, which was manually georeferenced with the orthophoto image. The indices used, including NDVI, NDWI, NDBI, and BSI, also served as references. The land cover classification achieved an overall accuracy of 96.85%. This shows a strong agreement between the classified map and the reference data. User accuracy (UA) ranged from 91.67% to 100%. Six classes: Built-up, Rail Network, Fish Pond with Water, Crop without Vegetation, Swamp, and Bare Soil achieved perfect scores. The lowest UA was for Waterbodies at 91.67% and Broadleaved Trees at 92.45%. Producer accuracy (PA) ranged from 88.26% to 100%. The lowest values were for Artificial Sealed Surface at 88.26% and Bare Soil at 88.59%. Detailed accuracy results for all classes are in Appendix Table D.

6.5.2. Roofing Material Validation

The roofing material map accuracy assessment underwent the same tool, method and reference data as mentioned in the land cover validation part. The assessment was also conducted using a stratified random sampling design, with a total of 200 samples distributed across four roofing material classes (see Appendix Table B and fully labelled with reference data interpretation).

The roofing material classification was generally accurate to 94.34%, which means that the classified map was closely related to the reference data. The range of UA was from 81.82% to 100%. Two classes, which were Concrete and uPVC, obtained a full score. However, the Metal category was only 81.82%, due to six samples of Metal being misclassified as Tile/Clay with a spectrum feature similar to Tile/Clay. The PA ranged from 84.59% to 100%, where Metal had the lowest PA 84.59%, and Tile/Clay obtained the highest PA 96.24%. The reason for omission errors was that the two classes were confused with each other. Please see the details for the accuracy values for each class in the Appendix Table E.

6.5.3. Model Validation

In order to validate the model performance, comparisons were carried out between the model without and with PSF correction in terms of whether a significant improvement was achieved. In the results for Land Cover Model, the R values for without and with PSF were 0.72 and 0.84, an improvement of roughly 11.3 percentage points and from 1.7537C to 1.3459C for the RMSE value (as Table 9). Likewise, in the results for the LCZ Model, from 0.71 to 0.79 for R (8.38 percentage points increase) and from 1.8107 °C to 1.5309 °C for RMSE. These results suggest that both models have significant improvements by incorporating PSF correction in estimating land surface temperature, and the Land Cover Model was more sensitive to the application of PSF than the LCZ Model. These consistent improvements for two indexes (R and RMSE) and two models imply that PSF is very important and should not be removed in future studies.

Table 9: Model Comparison Result

	With PSF		Without PSF	
	R^2	RMSE (°C)	R^2	RMSE (°C)
Land Cover Model	0.84	1.3459	0.72	1.7537
LCZ Model	0.79	1.5309	0.71	1.8107

6.7 Impact Assessment of Urban Morphology, Material Properties and Coastal Proximity on Land Surface Temperature Anomalies

To assess the localized influence of urban morphology on land surface temperature during the 2023–2024 heatwave and transitional periods, 50 sample areas were distributed in built-up areas, each approximately 0.058 km², isolating the effects of varying urban morphology and roofing material characteristics on LST variability across multiple acquisition dates (see Figure 20). Within this constrained geographic domain, we examined four key urban morphological indicators, such as BSF, ISF, PvSF and SVF, in relation to heterogeneous roof material compositions and differential proximity to the coastal environment, which collectively influence local thermal conditions. Sample areas were distributed based on the heterogeneity of each indicator, ensuring they met the requirements of statistical tests.

This methodological approach enabled the quantification of the fine-scale relationships between urban morphological complexity and LST responses during heatwave periods, accounting for the spatial heterogeneity in structure heterogeneity, surface materials and coastal influence that characterises the built-up environment. Zonal statistical analysis was conducted across urban morphological categories, roofing material types, and coastal proximity classes, revealing valuable insights into localized thermal variation (see Appendix Table C).

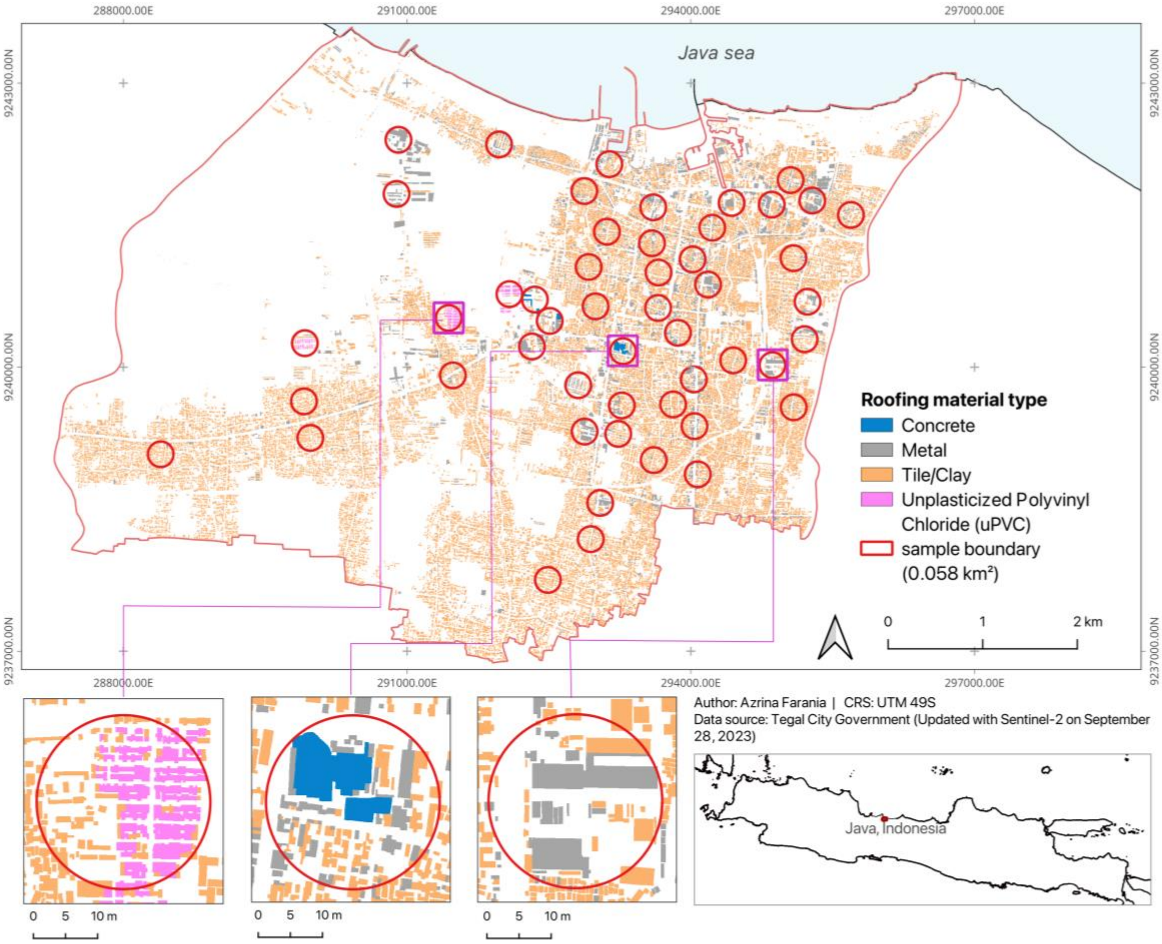

Figure 20: Spatial distribution of 50 sample areas (each 0.058 km²) used for roofing material and urban morphology analysis in Tegal City. Insets show material composition detail in three representative sample areas: uPVC and tile/clay dominated roofs (left), mix of concrete and metal roofs (middle) and metal dominated roofs (right).

The LST anomaly, calculated as the deviation of each sample's LST from the mean LST of all samples per acquisition date, ranged from approximately −6°C to +2.5°C across all dates and samples, with most observations falling between −2°C and +2°C, while extreme negative anomalies reaching below −4°C were observed across multiple dates. These anomaly values were then examined against rooftop material fractions across the 2023–2024 period to identify how material composition influences LST variability, as visualised in Figure 21 and Figure 22. Concrete fraction showed a negligible and statistically non-significant positive relationship with LST anomaly ($r = 0.048$, $p = 0.4078$). uPVC fraction exhibited a weak but statistically significant negative relationship ($r = -0.185$, $p = 0.0013$). Metal roofing demonstrated a significant negative relationship with LST anomaly ($r = -0.322$, $p < 0.001$), with the regression equation $y = -2.01x + 0.64$. Tile/clay fraction showed the strongest positive relationship ($r = 0.406$, $p < 0.001$), with the regression equation $y = 2.40x - 1.48$. Detailed statistics are presented in Appendix Table C.

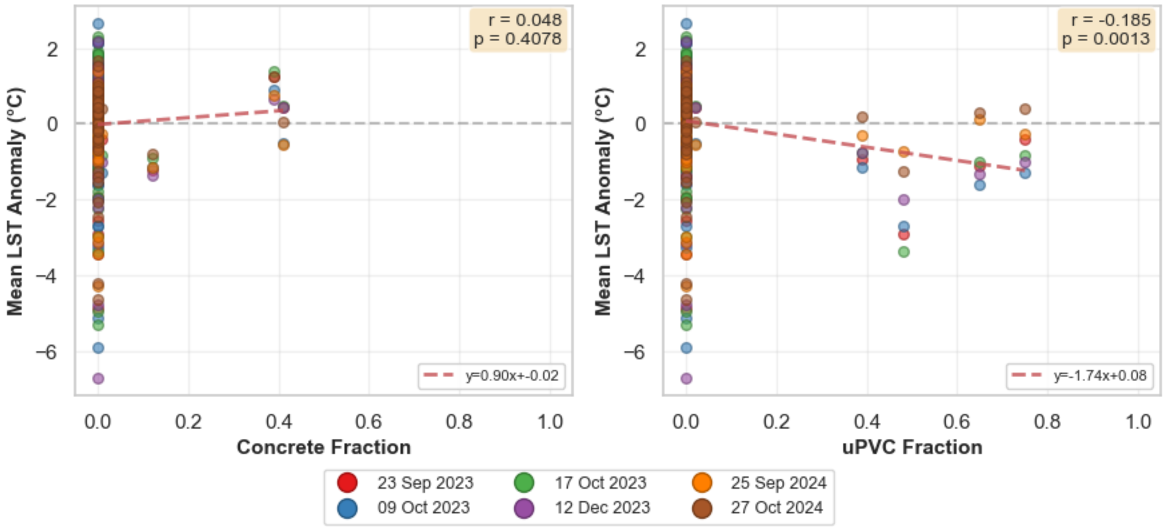

Figure 21: Relationship between mean LST anomaly (°C) and roofing material fraction across 50 sample areas, color-coded by date for six heatwave dates (2023–2024): concrete fraction (left) and uPVC fraction (right). Dashed lines indicate linear regression trends.

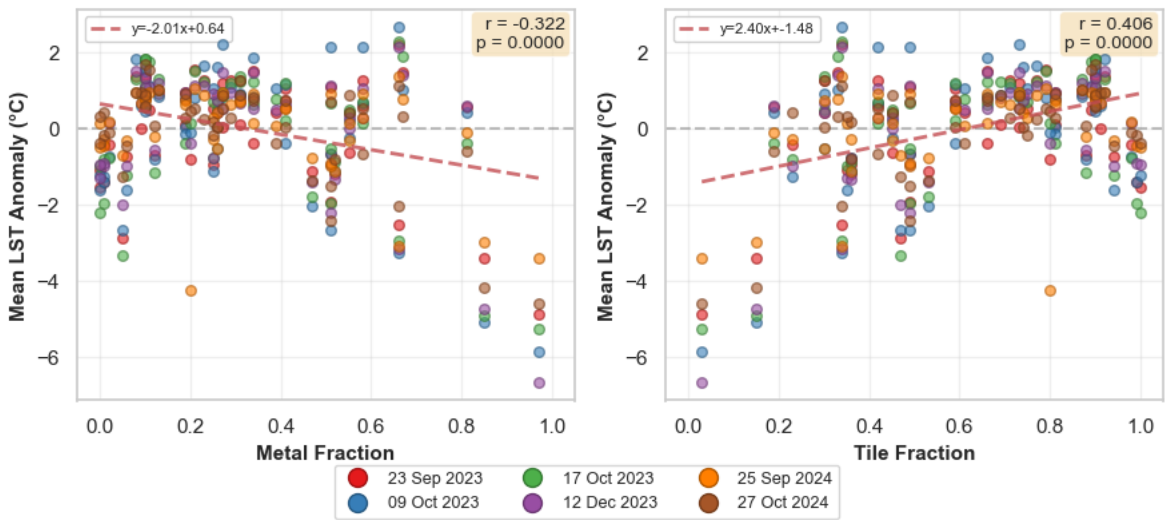

Figure 22: Relationship between mean LST anomaly (°C) and roofing material fraction across 50 sample areas, color-coded by date for six heatwave dates (2023, 2024): metal fraction (left) and tile/clay fraction (right). The lines show linear regression trends.

In terms of urban morphological characteristics, analysis results shown in Figure 23 and Figure 24 reveal differential influences on land surface temperature anomaly across the study period. BSF showed the second strongest positive relationship with LST anomaly ($r = 0.541$, $p < 0.001$), with the regression equation $y = 8.84x - 4.26$, indicating that areas with higher building coverage consistently exhibited elevated surface temperatures above the spatial mean. ISF demonstrated a weak but statistically significant positive relationship ($r = 0.180$, $p = 0.0018$), with the regression equation $y = 6.45x - 0.42$, suggesting a modest contribution of impervious surfaces to thermal enhancement. PvSF exhibited the strongest relationship among all morphological parameters, with a significant negative correlation ($r = -0.647$, $p < 0.001$) and regression equation y = −11.08x + 5.02, confirming that higher vegetation and permeable surface coverage are consistently associated with negative LST anomalies. SVF, despite its narrow observed range (0.996–1.000), showed a negligible and statistically non-significant relationship with LST anomaly ($r = 0.074$, $p = 0.2018$), with the regression equation y = 147.11x − 146.96. Detailed statistics are presented in Appendix Table C.

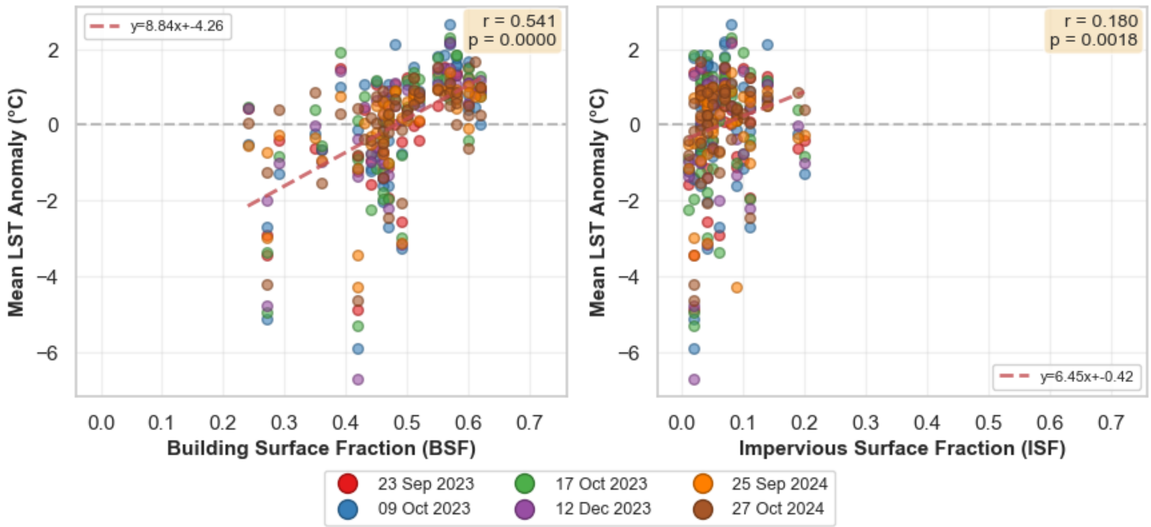

Figure 23: Relationship between mean LST anomaly (°C) and urban morphology fraction across 50 sample areas, color-coded by date for six heatwave dates (2023–2024): BSF (left) and ISF (right). Dashed lines indicate linear regression trends.

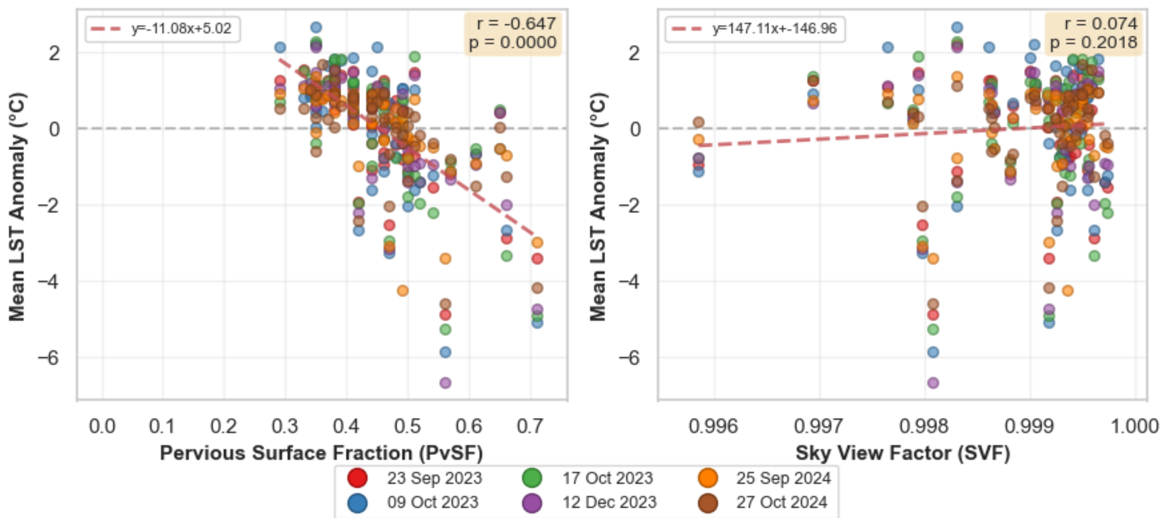

Figure 24: Relationship between mean LST anomaly (°C) and urban morphology fraction across 50 sample areas, color-coded by date for six heatwave dates (2023–2024): PvSF (left) and SVF (right). Dashed lines indicate linear regression trends.

The influence of coastal proximity on LST was examined through two complementary analyses. In the first analysis, LST anomaly values from all six acquisition dates were plotted against distance from the coast for all samples (Figure 25). This revealed a statistically significant negative relationship ($r = −0.192$, $p = 0.0228$), indicating that samples located further inland tend to exhibit lower LST anomaly values relative to the study area mean, with a trend consistent across all acquisition dates.

In the second analysis, residual results obtained from a linear mixed model (Figure 18), which did not account for the influence of urban morphological parameters and rooftop material properties, were used for observation. They were plotted against coastal distance to isolate the independent contribution of coastal proximity (Figure 26). This residual-based analysis similarly yielded a significant negative relationship (r = −0.193, p = 0.0178), with the regression equation y = −0.0002x + 0.30, confirming that the coastal proximity effect persists even after controlling for the variance explained by surface cover composition and morphological structure. The detail LST residuals value are described in Appendix Table C.

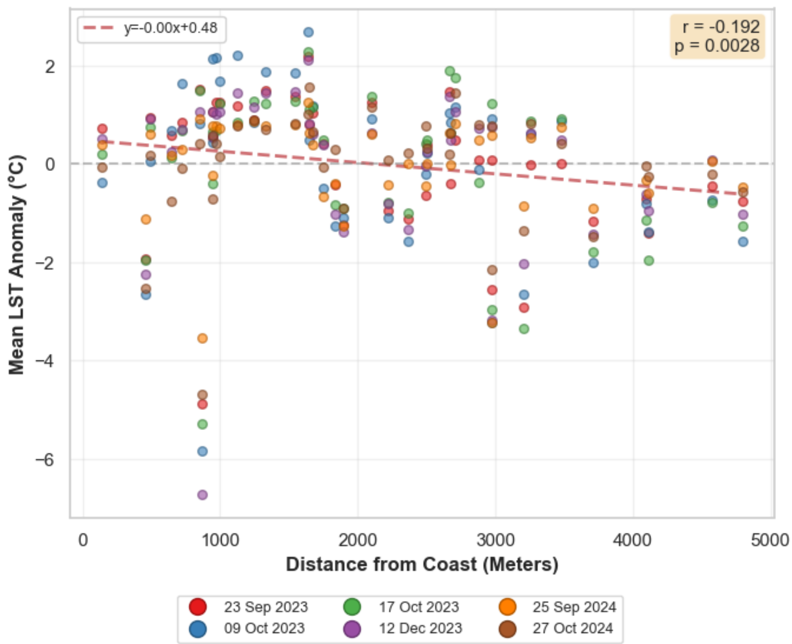

Figure 25: Relationship between mean LST anomaly (°C) and distance from coast across 50 sample areas, color-coded by date for six heatwave dates (2023–2024). Dashed lines indicate linear regression trends.

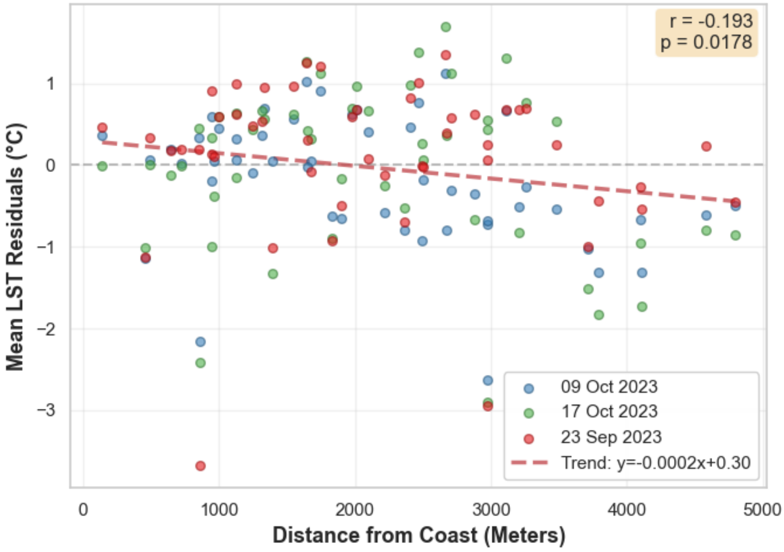

Figure 26: Relationship between mean LST residuals (°C) and distance from the coast across 50 sample areas, color-coded by date for six heatwave dates (2023, 2024). Dashed lines show linear regression trends.

7. Discussion

This discussion will explain how the estimation and interpretation of the SUHI are enhanced by analyzing the spatial distribution of urban surface characteristics, such as land cover, urban form, and roofing materials. It begins with an evaluation of the model used to measure the relationship between land cover and LCZs, as well as identifying factors that might influence model errors. Following this, a summary of the heat drivers and cooling features in Tegal City will be provided, including an assessment of how proximity to the ocean affects the SUHI. Finally, the limitations of the study and future implications will be explored in the concluding section of this discussion.

7.1 Model Performance and Comparative Analysis

This study reveals that land cover composition is the dominant control on Land Surface Temperature variation in Tegal City ($R^2 = 0.84$), explaining the majority of SUHI variability, while at fine scales analysis in built-up areas, roofing material composition and coastal proximity emerge as critical modulating factors.

The land cover-based regression model performs better than the LCZ classification analysis. It explained 4.8% higher variance of LST, it successfully mapped specific types of surface and their thermal effect at the neighborhood level compared to the morphological grouping of surfaces. This suggests that land cover type has greater control over LST variation in Tegal City than land morphology. RMSE analysis also indicated this result, where the land cover model got the 1.3459°C while the LCZ model resulted in 1.5309°C, showing the prediction error reduced by 0.185°C. The difference in model performance is probably due to the fact that the land cover classification can capture precise locations of thermally active surfaces like railways, built environments (e.g., impervious surfaces), vegetation, and explain the proportion. On the other hand, LCZ classification has taken all the components of thermal active surfaces like building height and arrangement as a single entity and has averaged out the thermal components. For example, an LCZ 3 (compact low-rise) zone may have buildings, pervious surfaces, and impervious surfaces, but the LCZ classification considers them all as one class with an average thermal impact. Although LCZs have not performed as well as land cover, they still offer useful context for urban structure types, such as compact mid-rise, open low-rise, and sparsely built areas. However, they do not distinguish between thermally active surfaces within these categories.

The land cover classification achieved higher accuracy compared to the LCZ typologies, which is in agreement with more recent findings (Oliveira et al., 2020) that LCZ classification cannot surpass in accuracy the source land cover maps and other data, like morphology and surface characteristics, that are inputs in the LCZ classification processes and LCZ maps accuracy slightly decreases compared to land cover maps accuracy. The interpolation methods based on the LCZ classification (Anjos et al., 2025) have been found to be challenging in areas of irregular shape or where there are few inputs like in LCZ 8 (large low-rise) and LCZ 14 (low plants), whereas methods based on standard spatial smoothing have yielded a higher accuracy. They also concluded that the discrete categories used in the LCZ typology might not adequately represent local temperature variability caused by natural or man-made elements which are not taken into account in the LCZ typology.

When considering the influence of the PSF application, the performance was better on both models, and the Land Cover Model is more sensitive to PSF application than the LCZ Model. The LCZ Model has lower sensitivity than the Land Cover Model because a finer-resolution map, such as land cover classification, benefits from PSF to address radiative transfer diffusion in low-resolution thermal images. All models of different types improved by PSF correction, confirming that it is an indispensable step for SUHI mapping, and it must be used in future analyses. This finding is consistent with Radoux et al. (2025), who demonstrated that the PSF model effectively captures the influence of land cover on SUHI across multiple acquisition dates, and that sensor PSF must be considered when interpreting LST derived from medium-resolution satellites such as Landsat.

7.2 Systematic Model Errors

Even though the Land Cover Model performs quite good (R = 0.834), analysis of the residuals showed systematic errors located on some pixels having the same pattern for the three acquisition dates (23 September 2023, 9 October 2023 and 17 October 2023). The residuals range from -7.33 °C (model overestimate) to +9.28 °C (model underestimate), with most predicted values within 2 °C of the measured values. It is interesting to note the persistence of these residuals in terms of spatial pattern. Those points that gave positive residuals (red boxed area) consistently did so, as did those which gave negative residuals (blue boxed area), over all three date acquisitions shown in Fig 17, regardless of the prevailing meteorological conditions or the season. This suggests a system of bias associated with a particular characteristic of the surface, which is not properly represented in the generic land cover classifications.

The red boxed area consistently had positive residuals (model underestimated the temperature) across all three dates of acquisition. Examination of high-resolution imagery shows that these areas of hotspot prediction predominantly represent bare soil surfaces, including an area designated for waste disposal. This finding indicates that the land cover classification, while distinguishing bare soil as a separate category, may not adequately represent the thermal variability within bare soil areas. To be clearer, the explanation for each thermal behaviour is provided below:

1. Bare soil hotspots (consistent underprediction).
   The first hotspot pattern was found across bare soil. The value of underprediction suggests that these locations are significantly more thermally active than the generalized bare soil thermal contribution would indicate. This means that bare soil areas with certain characteristics, such as being disturbed, compacted, or lacking moisture, heat up much more than agricultural bare soil or fallow fields within the same land cover type. This conclusion is backed by an accuracy assessment. It showed that bare soil reached a producer's accuracy of 88.59%. This indicates that about 11% of actual bare soil pixels were incorrectly classified as other categories, mostly as crop with vegetation. This classification uncertainty means that some thermally active bare surfaces are assigned the thermal contribution of less extreme classes, directly contributing to systematic underprediction in these areas.
2. Waste dumping site hotspots (consistent underprediction).
   The dumping site was also found to be a hotspot. Research by Edmondson et al. (2016) found that barren lands and poorly managed open surfaces, including waste and degraded land-cover areas, have distinct thermal properties. It contributes to higher land surface temperatures because of reduced vegetation cover and altered thermal storage characteristics. A study also found that open dumpsites containing organic waste, which generate measurable heat increases through biological and chemical decomposition processes (Mahmood et al, 2016).

The blue-boxed region consistently exhibited negative residuals (overprediction) across all three dates. High-resolution imagery revealed distinct coolspot overprediction characteristics in industrial Infrastructure. The coolspot areas in the blue-boxed region and also red-boxed region (see Figure 17) are characterized by metal roofing and metal-based building materials in industrial/commercial areas. This overprediction of LST reflects the fact that metal roofing exhibits strong cooling through reflectance of solar radiation and high emissivity, allowing it to cool down quickly.

Aluminum and galvanized steel roofing materials have high albedo values, ranging from 0.35 to 0.75. This means they reflect a larger portion of incoming solar radiation, which reduces heat absorption and surface temperature more than what generalized land cover thermal contributions suggest (Stache et al., 2022; Ahmed et al., 2025). The area and density of metal-roofed buildings can help create cooler local microclimates in industrial areas, a result not clearly shown by combined land cover categories. The cool spot is located in a mixed landscape of industry and aquaculture, where industrial buildings sit near fish ponds and water bodies. This overestimation of cooling probably comes from the difference in spatial resolution between the detailed land cover classification and the 30-meter Landsat LST pixels. At the boundaries between industrial surfaces and adjacent fish ponds, a single Landsat pixel captures a mixed thermal signal from both the hot industrial surface and the cool water body. The model, however, applies the full cooling weight of the pond fraction derived from the high-resolution land cover, leading to a systematic overprediction of cooling effects in these mixed industrial-aquaculture zones.

7.3 Primary Thermal Drivers in Tegal City

Land cover analysis reveals a clear thermal hierarchy in Tegal City, with specific surface types exhibiting distinct contributions to SUHI intensity. The thermal contribution spectrum ranges from strong warming effects for rail networks to substantial cooling effects for broadleaved trees, demonstrating that material composition is the primary control on spatial LST variation across the city.

Four land cover classes contribute to thermal enhancement in Tegal City:

1. Rail Networks.
   The strongest warming contributor despite occupying only 0.44% of the city. This exceptional thermal signature reflects the composition of rail infrastructure: metal rails, stone ballast, and concrete sleepers, which have low albedo values (0.30–0.45) and efficiently absorb solar radiation (Prado and Ferreira, 2005). The massive metal piece and stone materials accumulate and retain thermal energy, creating persistent hotspots along rail corridors. This finding aligns with research demonstrating that metal infrastructure contributes to increasing local thermal anomalies.
2. Artificial Sealed Surfaces.
   The second-largest warming contributor, reflecting Tegal's extensive network of asphalt roads, concrete parking areas, and paved surfaces. These materials have low albedo (0.05-0.20) and high thermal mass, absorbing daytime solar radiation and releasing it as sensible heat during thermal transitions (Stache et al., 2022).
3. Built-Up Areas.
   Built-up areas comprise 21.94% of Tegal City and contribute +5.79°C to LST, with thermal variability driven primarily by roofing material composition. Among the roofing materials examined, tile and clay exhibited the strongest warming effect, attributable to their low albedo and high thermal mass, which enables efficient absorption and retention of solar radiation, generating surface temperatures consistently above the

spatial mean. Concrete roofing showed no meaningful independent thermal influence, likely reflecting its limited spatial coverage within the study area rather than an absence of thermal effect. These findings suggest that rooftop material selection is a thermally significant decision in low-rise urban environments, with tile and clay dominating thermal enhancement.

4. Bare Soil.
   Contributes moderate warming, though the residual analysis (Section 6.4) revealed that specific bare soil conditions can warm significantly more than this generalized value suggests.

Regarding urban built-up characteristics captured by LCZ classes, the LCZ compactness emerges as a primary control on LST thermal response in Tegal City, with pronounced density-dependent warming patterns. LCZ compactness significantly controls LST, with compact mid-rise warming substantially more than compact low-rise, confirming research by Stewart & Oke (2012) showing that compact zones (LCZs 1–3) are consistently the warmest because their "canyon" geometry traps long-wave radiation and retards nocturnal cooling. In contrast, open low-rise and sparsely built zones remain cooler through higher pervious surface fractions and enhanced airflow.

7.4 Cooling Effects Drivers in Tegal City

Beyond vegetation, aquaculture and water features provide substantial thermal mitigation through high thermal capacity and evaporative cooling processes. Four land cover types exhibit pronounced cooling effects, forming a secondary cooling hierarchy distinct from vegetation mechanisms:

1. Broadleaved Trees.
   Despite comprising only 7.18% of the city, broadleaved trees provide the strongest cooling through combined effects of solar radiation shading and evapotranspiration. This finding is strongly supported by meta-analytic evidence showing that broadleaved tree canopy exhibits a stronger correlation with LST than herbaceous grass (Yang et al., 2022).
2. Fish Ponds with Water.
   Tegal City benefits from its aquaculture features. This finding is supported by Nguyen and Thi (2025), who found that a pond system can reduce the temperature of its surrounding environment by a maximum of 2.7°C, and further noted that ponds provide multiple ecosystem services, including microclimate regulation. While fish ponds without water show a slightly lower cooling intensity of -4.88°C compared to fish ponds

with water, this suggests that larger water surfaces tend to produce a cooler thermal environment, a pattern consistent with Syafii et al. (2021), who confirmed a positive relationship between pond size and cooling capacity, whereby larger water surfaces generate greater amounts of cool air. This has major implications for Tegal's urban planning, as fish ponds represent both cultural heritage and an underutilized nature-based climate adaptation resource.

3. Swamps and Waterbodies.
   Natural and constructed water features offer cooling effects that are comparable to or even exceed those of fish ponds. This can be attributed to water's high heat capacity, which enables it to absorb large amounts of energy with relatively little change in temperature, making it a conservative thermal influence and effective energy storer (Oke, 1987). This finding aligns with research conducted by Radoux et al. (2025) in Liège City, Belgium, which indicated that surface waters contribute to the lowest LST differences, with a mean LST difference of -7.09°C recorded over ten different dates.
4. Herbaceous Cover.
   Despite occupying 29.10% of Tegal City (the second-largest land cover class), herbaceous vegetation provides minimal cooling (−0.23°C), a counterintuitive finding confirmed by research showing that grassland provides negligible thermal benefit in tropical contexts (Moncada-Morales et al, 2025). This is consistent with research showing grass cooling is 3–4 times weaker than tree cooling due to low evapotranspiration rates and minimal shade provision (Yang et al., 2022). There may be some reasons to account for the result. The study period consisted of a long-term dry spell, which reduced the cooling effect of herbaceous cover due to limitations in evapotranspiration. Also, the broad definition of herbaceous cover might have combined spectrally similar yet thermally distinct surfaces. Land cover map errors might diminish the cooling effect by incorporating pixels not covered by vegetation. Herbaceous pixels located near buildings may not indicate their actual cooling capability in 30m resolution Landsat pixels. All the possible factors above may reveal that the results are due to the limitations of climate, classification, and sensor resolution, rather than true cooling insufficiency.

Among LCZ classes in natural LCZs, LCZ A-Dense trees showed the highest cooling, followed by LCZ G-Water, with the hierarchy matching the land cover model result (broadleaved trees, fish ponds with water) as dominant cooling classes. The close relationship between both frameworks shows that vegetation and water bodies function through the same basic thermal processes, evapotranspiration, and high heat capacity, no matter which classification system is used. Small differences in the cooling effect between the two models are due to the broader spatial grouping in the LCZ framework. This framework captures thermal behavior at the landscape level instead of focusing on the exact contribution of each surface type.

Meanwhile, within the built-up classes of LCZ, the Sparsely Built LCZ 9 has the highest negative correlation with land surface temperature (LST). A high percentage of pervious surface fraction (PvSF=0.81) and a low building surface fraction resulted in a low surface temperature. This study indicates that, for controlling urban temperature, it is equally important to achieve proper balance between building surface fraction (BSF) and pervious surface fraction (PvSF). Those with high BSF (0.47-0.51) and low PvSF (<0.4) have the highest thermal stress. However, the low-density area with low BSF (0.10) and high PvSF (0.81) has the coolest surface temperature. Research confirms that pervious surface expansion enhances cooling through evapotranspiration and soil moisture retention (He et al., 2025).

In built-up LCZ, fine-scale analysis confirmed that Metal and uPVC roofing, demonstrated cooling effects consistent with their comparatively higher surface reflectivity, which reduces heat absorption and lowers surface temperatures relative to surrounding surfaces. These findings are further corroborated by the residual analysis (Section 7.2), where metal-roofed industrial areas were associated with systematic model overprediction of cooling. This finding shows that reflective materials offer a measurable mitigation potential.

7.5 Multi-temporal LST Variability at the Urban Morphology Scale

In the constrained built-up environment, which includes 50 sample areas of 0.058 km² each, a multi-temporal analysis conducted over six periods from September 2023 to October 2024 revealed that roofing materials have a more significant impact than urban morphological metrics. This detailed perspective shows that, although regional thermal influences dominate general patterns, the properties of local materials are responsible for persistent thermal anomalies that remain consistent during both heatwaves and transitional periods.

Among the roofing materials, tile/clay exhibited a strong positive relationship with LST anomaly, whereas both metal and uPVC registered cooling values. Concrete had no significant thermal influence. The strong positive and negative correlation with albedo and thermal emissivity, respectively, reflect the significant influence of these properties on the heat balance of urban surface (Stewart & Oke 2012). The perfect inverse relationship of amounts of metal and tile reflects their synergistic efficiency in the residential area of Tegal.

When examining urban morphological parameters, the fraction of pervious surfaces emerged as the most significant predictor of cooling. This aligns with the understanding that vegetated surfaces encourage evapotranspiration and decrease net radiation absorption, and is further supported by evidence that NDVI serves as a dominant thermal control factor in compact and open low-rise environments, while vegetation arranged in small, fragmented clusters can paradoxically obstruct ventilation and elevate local temperatures, suggesting that the spatial configuration of green cover matters as much as its quantity (Moncada-Morales et al., 2025; Zhou et al., 2024). In contrast, the building surface fraction exhibited a moderate warming relationship with LST, as increasing building coverage traps more absorbed solar energy and diminishes heat exchange between the surface and the atmosphere, a pattern confirmed across all LCZ built types with compact low-rise zones showing particular sensitivity to building density increases (Li et al., 2025; Zhou et al., 2024). Additionally, the fraction of impervious surfaces showed a weak but statistically significant positive correlation with LST, reflecting the heat-retaining characteristics of sealed surfaces, though its effect remains modest compared to the influences of vegetation and roofing materials. The warming influence of impervious surfaces is also noted to be spatially variable and moderated by proximity to green space and water bodies across different LCZ types (Zhou et al., 2024).

SVF presented a more complex picture. Despite its importance as a driver of longwave radiation trapping in urban canyons, SVF showed no significant relationship with LST in this study. This aligns with the uniformity of the area: in flat terrain with consistent building heights, SVF varies too little to create meaningful thermal differences. As Stewart & Oke (2012) note, SVF is most useful in places with noticeable height differences, and its thermal impact decreases in uniform, low-rise residential zones like those studied here.

The coastal distance presents a significant linear relationship with the surface temperature, illustrated by Figure 25 and 26. The cooling influence is still visible up to the coastal distance of 1 km despite the presence of port facilities, proving that the cooling effect of sea breeze is more than the warming effect from the activities at the port. However, urban, industrial, and aquaculture cover occupies from 1 km to 3.5 km inland, and there, urban thermal effects are more intense than coastal effects, so we see a stable warm trend as illustrated by the graphs. Samples near the coast have always had greater surface temperature values than the mean of the entire area of study, which is unexpected to the common perception of coastal cooling. This abnormal correlation where the proximity to sea leads to the higher surface temperature is caused by the thermally active coastal cover in Tegal city area, influenced greatly by industrial site, port facilities and aquaculture, and though sea breezes can significantly reduce the UHI intensity, the structure of coastal cover may influence it (Yang et al., 2022). When dense urban areas are near the shore, the warming from these surfaces can outweigh the cooling winds, leading to higher temperatures along the coast. The same study also noted that land breeze circulation, which flows from the urban surface toward the sea, tends to be positively associated with heat island intensity, suggesting that in cities where urban density sits adjacent to the shore, nocturnal land breezes can further amplify rather than relieve thermal stress in near-coastal zones (Yang et al., 2022). The residual-based analysis confirmed the same directional effect after controlling for land cover composition and urban morphology, indicating that this coastal warming pattern is a persistent structural feature of Tegal's thermal landscape rather than an artefact of surface composition. Crucially, the relative thermal ordering of samples remained stable across all acquisition dates, including periods of peak heat intensity, confirming that these material and geographic drivers represent persistent structural determinants of Tegal City's intra-urban thermal landscape, consistent with the concept of urban surface thermal inertia (Akbari et al., 1998; Trlica et al., 2017).

7.6 Study Limitations and Methodological Constraints

This study is subject to several methodological limitations inherent to LST retrieval from Landsat thermal imagery and land cover classification in urban environments that warrant discussion. The primary source of uncertainty in Landsat LST retrieval stems from atmospheric correction errors, which contribute 0.2–0.7°C uncertainty in surface temperature estimates, with additional emissivity uncertainty contributing 0.2–0.4°C error (Parastatidis et al., 2017). Errors in atmospheric water vapor content are particularly problematic for mono-window algorithms, which were designed for water vapor ranges of 0–3 g cm^{-2}, and tropical coastal environments like Tegal City often exceed these thresholds (Parastatidis et al., 2017). Furthermore, cloud infiltration and aerosol scattering can introduce systematic bias, with cloud contamination artificially depressing LST values due to lower cloud-top temperatures (Parastatidis et al., 2017). These atmospheric effects errors could explain some discrepancies between modeled and actual LST for this investigation, although the PSF correction corrects some of this. Several issues of limitations must also be noted, including variability in atmospheric conditions based on season, transmission of uncertainty from LST retrieval, and the restricted application of the results due to the urban domination effect.

Regarding the spatial resolution limitation of Landsat 8/9 TIRS has a native spatial resolution of 100 m, resampled to 30 m in distributed products, which constrains fine-scale LST mapping in complex urban environments (Gevaert & García-Haro, 2015). This coarse resolution limits detection of LST spatial patterns at the neighborhood and street-canyon scale, potentially smoothing sharp thermal gradients between high-reflectance (metal roofs) and low-reflectance (dark asphalt) surfaces that exist within single 100 m pixels. LST values in this study represent pixel-aggregated temperatures. We cannot distinguish individual buildings, herbaceous cover, or narrow streets. This limitation may hide thermal differences within pixels, especially in mixed urban areas.

In Tegal City, manual land cover mapping based on composite satellite imagery might not capture changes over time between image acquisition dates (September 2023 to October 2024 across six dates). This is particularly true for dynamic classes like flooded rice paddies, temporary standing water, and changes in vegetation. Seasonal agricultural cycles in Indonesia mean that land cover in farming areas can vary significantly between acquisition dates. This creates a temporal bias if a single land cover map is used for all LST retrievals. Moreover, the confusion caused by spectrally similar classes, such as dark asphalt versus wet bare soil or herbaceous grass versus young vegetation, can lead to misclassification errors of 5 to 10 percent per class. These errors directly affect the Point Spread Function (PSF) model and increase residuals in poorly classified pixels.

This study also identifies refinements that can influence LCZ's representation of SUHI. Observing LCZ that exactly match with the definition of LCZ specified in Stewart & Oke (2012) in Tegal City is a bit difficult since most of the area in the city is organically build and not planned. Research shows that heterogeneity in the urban environment of tropical cities can introduce a mixed urban fabric within a single LCZ class, which may not capture SUHI accurately; therefore, adding sub-classification within LCZ can yield meaningful climate analysis results (Kotharkar and Bagade, 2018). Subclassification mixes a couple of classes, such as a mix of urban 3 and natural F into LCZ 3F: compact low-rise nesting soil. It shows that the more unique and representative the true condition is, the more accurately it represents unique tropical thermal signatures and increase the accuracy to evaluate the air temperature field in areas with mixed urban fabric (Anjos et al., 2020).

Roofing material identification from multispectral Landsat/Sentinel data inherently suffers from spectral similarity and as well as the limitation aged metal roofs can exhibit similar spectral reflectance in visible-infrared bands, particularly when corroded or weathered (Weng and Quattrochi, 2006). Roofing materials are not fixed. Informal settlements and new buildings in Tegal City might see quick roof replacements. This means the roofing material map used here may not accurately show conditions during all six acquisition dates. This is especially true if urban growth or renovations occurred in specific areas during the study period.

Over a thirteen-month period, urban land cover and infrastructure change. These changes include plant growth cycles, agricultural harvest and planting schedules, and construction or demolition activities. The assumption that land cover types and roofing material distributions stay the same throughout the multi-temporal analysis of all six LST retrievals does not hold if significant land-use changes took place. In particular, the fastest-warming LCZ3 areas might see new metal roofs, which lower temperatures by −7.33°C, or lose vegetation. This could alter the thermal balance, making it tough to determine if changes in LST over time are due to weather, land-atmosphere interactions, or unmeasured land-cover changes.

Both the Land Cover Model and the LCZ Model introduce uncertainties from various sources. These include a Land Surface Temperature (LST) retrieval error ranging from 0.2 to 0.7°C, as well as land cover classification errors based on the accuracy assessment shown in Appendix Table D. The overall accuracy for land cover classification is 96.85%, with omission errors for certain classes ranging from 0% to 11.74%. The highest omission errors are found in the bare soil class (11.41%) and for artificial sealed surfaces (11.74%). Additionally, there is a roof type classification error based on the accuracy assessment in Appendix Table G, which shows an overall accuracy of 94.34%. The most significant issues arise from misclassifying metal roofs, resulting in an 18.18% commission error and a 15.41% omission error, largely due to confusion with tile or clay roofs. Finally, there is an emissivity uncertainty of 0.2 to 0.4°C. All these factors influence the performance of the model. High thermal activity exists in bare soil and artificial sealed surfaces classes, while metal roof covers the most cooling surface in this case. When these separate uncertainties combine, the total model error may be larger than the reported RMSE, especially in areas where critical classes are misclassified or where conditions were not ideal. This propagation is not formally quantified, creating unexplained model residuals.

7.7 Future Urban Heat Mitigation Strategies

The findings from this study reveal actionable pathways for reducing SUHI intensity in Tegal City through targeted spatial planning and material interventions. Drawing on quantified thermal contributions of land cover types and urban morphology, we propose evidence-based mitigation strategies with specific thresholds for implementation.

1. Cool roof implementation
   Research from tropical coastal cities demonstrates that increasing roof albedo can reduce ambient temperatures by 1.7–3.6°C at the city scale (Zhang et al., 2025). For Tegal City specifically, a practical cool roof strategy involves applying white solar-reflective coating onto existing tile/clay roofs, the dominant warming material identified in this study ($r = +0.406$), rather than full material replacement, as changing tile color from red to white has been shown to reduce peak rooftop surface temperature by up to 16°C and annual cooling energy demand by up to 13.14% in tropical climates with similar roofing characteristics (Farhan et al., 2021). Targeting LCZ3 and LCZ6 zones where tile/clay roofing dominates thermal warming, such an intervention could yield measurable cooling benefits without requiring land-use change. Implementing cool

roofs requires careful consideration of their effects on individual buildings. Although metal materials can help cool urban areas overall, they may negatively impact individual buildings. Materials with high thermal inertia, like metal roofs and concrete, can absorb solar radiation during the day and retain heat for long periods (Li et al., 2024). In buildings with insufficient thermal insulation and inadequate interior ventilation, this trapped heat can raise indoor air temperatures, leading to reduced thermal comfort for occupants.

2. Waterbodies preservation and strategic expansion

   Given the significant cooling benefits demonstrated by active fish ponds and other water bodies, including rivers, lakes, and retention ponds in Tegal City, urban planning efforts should prioritise the strategic preservation and development of additional water bodies, such as constructed lakes and retention ponds, within high surface temperature zones, particularly in densely built-up areas. Ponds should be designed with longer and more complex perimeters to maximise their cooling surface exposure, as the cooling influence of a pond system can extend up to a maximum distance of 140 m from the pond's edge (Nguyen & Thi, 2025).

3. Building Coverage and Density Thresholds

   This study's analysis demonstrates that BSF shows a moderate warming correlation with LST, consistent with Li et al. (2025), who found that building coverage ratio generates the greatest warming effect, beyond which the warming effect plateaus. For Tegal City, this means that increasing density in key areas (LCZ3, LCZ6) without enough green infrastructure could raise thermal stress. According to Li et al. (2025), a maximum BSF of 0.32 is suggested as a suitable limit for medium-density zones in Tegal City, which aligns with the warming trend seen in this study. An exception is allowed only in Tegal's central business district, as long as it includes mandatory cool roofing and street-level green corridors.

4. Minimum Green Area Requirements and Vegetation Thresholds

   Vegetation especially broadleaved trees is the strongest cooling mechanism and research shows that 10% increase in vegetation coverage reduces temperature ~0.5°C (Peng et al., 2024). A recommendation minimum 25% green/vegetated area across all urban zones:

   - LCZ 2 (Compact Midrise) and LCZ 3 (Compact Low-Rise): Mandate 25% green area via rooftop gardens, street trees, and courtyard vegetation.
   - LCZ6 (Open Low-Rise): Enforce 35% pervious surface through street-tree corridors (8–10 m spacing) and permeable paving.
   - LCZ9 (Sparsely Built): Preserve 50% green area to maintain regional cooling and prevent sprawl-driven SUHI expansion.

8. Conclusion

This study investigated how the spatial distribution of urban surface representation, including land cover, urban form (LCZ), and roofing materials, affects the estimation and interpretation of the SUHI in Tegal City, Indonesia. By the integration of multi-temporal Landsat thermal images and detailed urban surface characterizations, this study suggests that understanding land cover type, spatial arrangements, and roofing materials composition is needed for effective SUHI estimation and interpretation. A single-factor approach (just land cover and just urban morphology) will give an incomplete understanding of urban thermal processes and potentially incorrect mitigation strategies.

This study produced three types of mutually-reinforcing urban surface representations, including land cover by Sentinel-2 spectral indices, urban morphology by the LCZ scheme, and detailed roofing materials. Multi-temporal Land Surface Temperature from six Landsat thermal band acquisitions represented the changes of land surface temperature on seasonal variations and spatial differences. All three features were considered as initial baseline characterization of the urban surface features that control land surface temperature in Tegal City, and each of them shows its unique controls on surface temperature in Tegal City.

Three urban surface components (land cover composition, urban morphology, and roofing material albedo) can influence the magnitude of SUHI in different mechanisms. Land cover composition controls the baseline thermal response to the incident energy by its material's albedo and the potential for evapotranspiration, whereas the increase in built-up area will lead to warming, while vegetation will reduce it. Urban morphology affects these compositional effects through building geometry and ventilation patterns. Dense urban areas trap more heat than those with sparse buildings.

Key findings indicate that small-scale thermal differences in Tegal City are consistent in all acquisition dates, thus insensitive to weather variability, which shows SUHI is controlled by persistent material and geographic features rather than the fluctuation in weather. The coastal proximity may have the effect of maintaining persistent thermal gradients throughout the whole year due to the maritime advection, and the characteristics of building materials lead to thermal signatures that are stable throughout the year. The control morphology composition, form, and materials were strongly supported by analyzing all three types of urban surface representation simultaneously in explaining land surface temperature variations in Tegal City. Thus, to precisely estimate SUHI, not only land cover, but also its structure and material need to be well-understood.

To design an integrated heat-mitigation policy in Tegal City, strategies such as optimizing building materials through cool-roof applications, preserving and increasing vegetation cover, managing building density, and protecting coastal areas must be incorporated. In future studies, it will be essential to monitor dynamic land cover and building materials using high-resolution thermal sensors, such as the Copernicus 50-meter LSTM mission planned for 2028. Additionally, further exploration of the relationship between surface temperature modeling and air temperature measurements is important, as it can lead to a deeper understanding of surface-atmosphere interactions.

9. References

Akbari, H., Pomerantz, M., & Taha, H. (1998). Cool surfaces and shade trees to reduce energy use and improve air quality in urban areas. *Solar Energy*, 70(3), 295–310. https://doi.org/10.1016/S0038-092X(00)00089-2

Alchapar, N. L., Correa, E. N., & Cantón, M. A. (2014). Classification of building materials used in the urban envelopes according to their capacity for mitigation of the urban heat island in semiarid zones. *Energy and Buildings*, 69, 22–32. https://doi.org/10.1016/j.enbuild.2013.10.012

Ahmed, S. Z., La Rosa, D., & Jayakumar, S. (2025). Seasonal and diurnal dynamics of urban surfaces: Toward nature-supportive strategies for SUHI mitigation. *Land*, 14(12), 2412. https://doi.org/10.3390/land14122412

Andriambololonaharisoamalala, R. R., Helmholz, P., Bulatov, D., Ivanova, I., Song, Y., Soon, S., & Jones, E. (2025). Downscaling of urban land surface temperatures using geospatial machine learning with Landsat 8/9 and Sentinel-2 imagery. *Remote Sensing*, 17(14), 2392. https://doi.org/10.3390/rs17142392

Anjos, M., Medeiros, D., Castelhano, F., Meier, F., Silva, T., Correia, E., & Lopes, A. (2025). LCZ4r package R for local climate zones and urban heat islands. *Scientific Reports*, 15(1), 7710. https://doi.org/10.1038/s41598-025-92000-0

Badan Informasi Geospasial. (2026). DEMNAS: Digital Elevation Model Nasional [Data set]. Tanahair Indonesia Portal. https://tanahair.indonesia.go.id/portal-web/

Bulatov, D., Burkard, E., Ilehag, R., Kottler, B., & Helmholz, P. (2020). From multi-sensor aerial data to thermal and infrared simulation of semantic 3D models. *Infrared Physics & Technology*, 105, 103233.

Capeluto, I., & Shaviv, E. (2001). On the use of 'solar volume' for determining the urban fabric. *Solar Energy*, 70, 275–280. https://doi.org/10.1016/S0038-092X(00)00088-8

Cetin, M., Isik Pekkan, Ö., Ozenen Kavlak, M., Atmaca, I., Nasery, S., Derakhshandeh, M., & Cabuk, S. N. (2024). Urban heat island analysis using GIS and remote sensing. *Natural Hazards*, 120, 5509–5536. https://doi.org/10.1007/s11069-024-06431-5

Copernicus Climate Change Service. (2023). ERA5 hourly data on single levels from 1940 to present [Data set]. Copernicus Climate Change Service (C3S) Climate Data Store (CDS). https://doi.org/10.24381/cds.adbb2d47

Dawodu, A., & Cheshmehzangi, A. (2017). Impact of floor area ratio (FAR) on energy consumption at meso scale in China. *Energy Procedia*, 105, 3449–3455. https://doi.org/10.1016/j.egypro.2017.03.789

Deilami, K., Kamruzzaman, M., & Liu, Y. (2018). Urban heat island effect: A systematic review of spatio-temporal factors, data, methods, and mitigation measures. *International Journal of Applied Earth Observation and Geoinformation*, 67, 30–42. https://doi.org/10.1016/j.jag.2017.12.009

Dian, C., Pongrácz, R., Dezső, Z., & Bartholy, J. (2020). Annual and monthly analysis of surface urban heat island intensity with respect to the local climate zones in Budapest. Urban Climate, 31, 100573. https://doi.org/10.1016/j.uclim.2019.100573

Dissanayake, D., Morimoto, T., Ranagalage, M., & Murayama, Y. (2019). Land-use/land-cover changes and their impact on surface urban heat islands. *Climate*, 7(8), 99. https://doi.org/10.3390/cli7080099

Edmondson, J., Stott, I., Davies, Z., et al. (2016). Soil surface temperatures reveal moderation of the urban heat island effect by trees and shrubs. *Scientific Reports*, 6, 33708. https://doi.org/10.1038/srep33708

Elmes, A., Healy, M., Geron, N., Andrews, M. M., Rogan, J., Martin, D. G., Sangermano, F., Williams, C. A., & Weil, B. (2020). Mapping spatiotemporal variability of the urban heat island across an urban gradient in Worcester, Massachusetts. *GIScience & Remote Sensing*, 57(7), 845–864. https://doi.org/10.1080/15481603.2020.1818950

Earth Resources Observation and Science (EROS) Center. (2020). Landsat 8-9 Operational Land Imager/Thermal Infrared Sensor Level-1, Collection 2 [Data set]. U.S. Geological Survey. https://doi.org/10.5066/P975CC9B

Esch, T., Brzoska, E., Dech, S., Leutner, B., Palacios-Lopez, D., Metz-Marconcini, A., Marconcini, M., Roth, A., & Zeidler, J. (2022). World Settlement Footprint 3D - A first three-dimensional survey of the global building stock. *Remote Sensing of Environment*, 270, 112877. https://doi.org/10.1016/j.rse.2021.112877

Estoque, R. C., Murayama, Y., & Myint, S. W. (2017). Effects of landscape composition and pattern on land surface temperature. *Science of the Total Environment*, 577, 349–359. https://doi.org/10.1016/j.scitotenv.2016.10.195

European Space Agency. (2023). Copernicus Sentinel-2 [Level-2A] MSI data [Data set]. Retrieved from https://dataspace.copernicus.eu/

European Space Agency. (2023). Sentinel-2 products specification document (PSD): Collection 1 Level-2A. Retrieved from https://sentinels.copernicus.eu/web/sentinel/technical-guides/sentinel-2-msi/level-2a/product-specification

Farhan, S. A., Ismail, F. I., Kiwan, O., Shafiq, N., Zain-Ahmed, A., Husna, N., & Hamid, A. I. A. (2021). Effect of Roof Tile Color on Heat Conduction Transfer, Roof-Top Surface Temperature and Cooling Load in Modern Residential Buildings under the Tropical Climate of Malaysia. Sustainability, 13(9), 4665. https://doi.org/10.3390/su13094665

Feng, Y., Gao, C., Chen, S., Lei, Z., & Wang, J. (2019). Spatial patterns of land surface temperature and their influencing factors: A case study in Suzhou, China. *Remote Sensing*, 11, 182. https://doi.org/10.3390/rs11020182

Garuma, G. F. (2023). Tropical surface urban heat islands in east Africa. Scientific Reports, 13(1), 4509. https://doi.org/10.1038/s41598-023-31678-6

Gál, T., Bechtel, B., & Unger, J. (2016). Comparison of two different local climate zone mapping methods. *IEEE Journal of Selected Topics in Applied Earth Observations and Remote Sensing*, 9(5), 1841–1853. https://doi.org/10.1109/JSTARS.2016.2539977

Ge, M., Xiong, Z., Li, Y., Li, L., Xie, F., Gong, Y., & Sun, Y. (2025). Research on Thermal Environment Influencing Mechanism and Cooling Model Based on Local Climate Zones: A Case Study of the Changsha–Zhuzhou–Xiangtan Urban Agglomeration. Remote Sensing, 17(14), 2391. https://doi.org/10.3390/rs17142391

Gevaert, C. M., & García-Haro, F. J. (2015). Combining Landsat 8 and Sentinel-2 data in Google Earth Engine to derive higher resolution land surface temperature maps in an urban environment. *Remote Sensing*, 14(16), 4076. https://doi.org/10.3390/rs14164076

Ginting, S. G. (2024). The effect of material and roof shape on thermal comfort in residential buildings. *International Journal of Architecture and Urbanism*, 8(3), 497–503.

Gu, Y., & Li, D. (2018). A modeling study of the sensitivity of urban heat islands to precipitation at climate scales. *Urban Climate*, 24, 982–993.

Hassan, T., Zhang, J., Prodhan, F. A., Pangali Sharma, T. P., & Bashir, B. (2021). Surface urban heat islands dynamics in response to LULC and vegetation across South Asia (2000–2019). *Remote Sensing*, 13(16), 3177. https://doi.org/10.3390/rs13163177

He, R., Wang, J., & Liu, D. (2025). Assessing the impact of urban spatial form on land surface temperature using random forest. *Land*, 14(8), 1639. https://doi.org/10.3390/land14081639

Hersbach, H., et al. (2023). ERA5 hourly data on single levels from 1940 to present. Copernicus Climate Change Service (C3S) Climate Data Store. https://doi.org/10.24381/cds.adbb2d47

Huang, F., Jiang, S., Zhan, W., Bechtel, B., Liu, Z., Demuzere, M., Huang, Y., Xu, Y., Ma, L., Xia, W., Quan, J., Jiang, L., Lai, J., Wang, C., Kong, F., Du, H., Miao, S., Chen, Y., & Chen, J. (2023). Mapping local climate zones for cities: A large review. *Remote Sensing of Environment*, 292, 113573. https://doi.org/10.1016/j.rse.2023.113573

Innayatuhibbah, G. A., Harisudin, M., & Ani, S. W. (2019). Laju konversi lahan pertanian dan faktor-faktor yang memengaruhi konversi lahan pertanian di Kota Tegal. *Agrista*, 7(3), 270–279.

Intergovernmental Panel on Climate Change. (2023). Climate change 2023: Synthesis report. Cambridge University Press. https://doi.org/10.59327/IPCC/AR6-9789291691647.001

Irons, J. R., Barsi, J. A., Johnson, D. M., Lunsford, A. W., Wirsing, K., & Sciretta, K. (2012). The Landsat data continuity mission: Operational Land Imager and Thermal Infrared Sensor. *Remote Sensing of Environment*, 122, 11–21. https://doi.org/10.1016/j.rse.2011.08.026

Jamei, E., Rajagopalan, P., Seyedmahmoudian, M., & Jamei, Y. (2016). Review on the impact of urban geometry and pedestrian level greening on outdoor thermal comfort. *Renewable and Sustainable Energy Reviews*, 54, 1002–1017. https://doi.org/10.1016/j.rser.2015.10.104

Jamei, Y., Rajagopalan, P., & Sun, Q. (2019). Spatial structure of surface urban heat island and its relationship with vegetation and built-up areas in Melbourne, Australia. *Science of the Total Environment*, 659, 1335–1351. https://doi.org/10.1016/j.scitotenv.2018.12.308

Jiménez-Muñoz, J. C., & Sobrino, J. A. (2003). A generalized single-channel method for retrieving land surface temperature from remote sensing data. *Journal of Geophysical Research*, 108, 4688–4695. https://doi.org/10.1029/2003JD003666

Jimenez-Munoz, J. C., Sobrino, J. A., Skokovic, D., Mattar, C., & Cristobal, J. (2014). Land surface temperature retrieval methods from Landsat-8 Thermal Infrared Sensor data. *IEEE Geoscience and Remote Sensing Letters*, 11(10), 1840–1843. https://doi.org/10.1109/LGRS.2014.2312032

Joshi, K. K., & Kono, T. (2009). Optimization of floor area ratio regulation in a growing city. *Regional Science and Urban Economics*, 39(4), 502–511.

Keeley, M. (2011). The green area ratio: An urban site sustainability metric. *Journal of Environmental Planning and Management*, 54(7), 937–958. https://doi.org/10.1080/09640568.2010.547681

Kior, A., Yudina, L., Zolin, Y., Sukhov, V., & Sukhova, E. (2024). RGB imaging as a tool for remote sensing of terrestrial plant characteristics: A review. *Plants*, 13(9), 1262. https://doi.org/10.3390/plants13091262

Kotharkar, R., & Bagade, A. (2018). Evaluating urban heat island in the critical local climate zones of an Indian city. *Landscape and Urban Planning*, 169, 92–104. https://doi.org/10.1016/j.landurbplan.2017.08.009

Lai, J., Zhan, W., Huang, F., Voogt, J., Bechtel, B., Allen, M., ... Du, P. (2018). Identification of typical diurnal patterns for clear-sky climatology of surface urban heat island. *Remote Sensing of Environment*, 217, 203–220.

Li, J., & Chen, B. (2020). Global revisit interval analysis of Landsat-8, Landsat-9 and Sentinel-2A, 2B data for terrestrial monitoring. *Sensors*, 20(22), 6631. https://doi.org/10.3390/s20226631

Li, J., Huang, X., Tu, L., Zhang, T., & Wang, L. (2022). A review of building detection from very high resolution optical remote sensing images. *GIScience & Remote Sensing*, 59(1), 1199–1225.

Li, Y., Wang, Y., Yang, M., Du, Y., & Liu, J. (2025). What is the relationship between urban heat island (UHI) effect and urban surface parameter (USP) at micro-scale? A case study in Gulangyu, China. Sustainable Cities and Society, 106959. https://doi.org/10.1016/j.scs.2025.106959

Li, X., Zhang, Y., & Wang, Z. (2024). Temporal dynamics of land surface temperature and thermal inertia in urban areas. Journal of Applied Remote Sensing, 18(2), 024501. https://doi.org/10.1117/1.JRS.18.024501

Li, X., Zhou, Y., Asrar, G. R., Imhoff, M., & Li, X. (2017). The surface urban heat island response to urban expansion: A panel analysis for the conterminous United States. *Science of the Total Environment*, 605–606, 426–435. https://doi.org/10.1016/j.scitotenv.2017.06.229

Li, Z.-L., Tang, B.-H., Wu, H., Ren, H., Yan, G., Wan, Z., Trigo, I. F., & Sobrino, J. A. (2013). Satellite-derived land surface temperature: Current status and perspectives. *Remote Sensing of Environment*, 131, 14–37. https://doi.org/10.1016/j.rse.2012.12.008

Liu, Y., & Zhou, Y. (2021). Territory spatial planning and national governance system in China. *Land Use Policy*, 102, 105288. https://doi.org/10.1016/j.landusepol.2021.105288

Llano, X. C. (2024). AcATaMa: QGIS plugin for accuracy assessment of thematic maps (Version 24.10) [Software]. SMByC-IDEAM. https://plugins.qgis.org/plugins/AcATaMa/

Mahmood, K., Batool, S. A., & Chaudhry, M. N. (2016). Studying bio-thermal effects at and around MSW dumps using Satellite Remote Sensing and GIS. Waste management, 55, 118-128. http://dx.doi.org/10.1016/j.wasman.2016.04.020

Masson, V., Lemonsu, A., Hidalgo, J., & Voogt, J. (2020). Urban climates and climate change. *Annual Review of Environment and Resources*, 45, 411–444. https://doi.org/10.1146/annurev-environ-012320-083623

Manoli, G., Fatichi, S., Bou-Zeid, E., & Katul, G. G. (2020). Seasonal hysteresis of surface urban heat islands. *Proceedings of the National Academy of Sciences*, 117(13), 7082–7089. https://doi.org/10.1073/pnas.2002068117

Megayanti, T., Widaningsih, L., Minggra, R., & Dewi, N. I. K. (2018). Building coverage ratio at the Eastern Corridor of Jalan Ir. H. Djuanda Bandung. *IOP Conference Series: Materials Science and Engineering*, 288, 012144. https://doi.org/10.1088/1757-899X/288/1/012144

Meng, F., Yan, S., Tian, G., & Wang, Y. (2023). Surface urban heat island effect and its spatiotemporal dynamics in metropolitan area. *Frontiers in Environmental Science*, 11, 1247046. https://doi.org/10.3389/fenvs.2023.1247046

Moncada-Morales, G. A., Verichev, K., López-Guerrero, R. E., & Carpio, M. (2025). A global review of vegetation's interaction effect on urban heat mitigation across different climates. *Urban Science*, 9(9), 361. https://doi.org/10.3390/urbansci9090361

Nguyen, Q. V., & Thi, V. H. D. (2024). Influence of Pond System on Surface Temperature and Urban Cooling. Ecohydrology, 18(1), e2760. https://doi.org/10.1002/eco.2760

Oke, T.R. (1987). Boundary Layer Climates (2nd ed.). Routledge. https://doi.org/10.4324/9780203407219

Oliveira, A., Lopes, A., & Niza, S. (2020). Local climate zones classification method from Copernicus land monitoring service datasets: An ArcGIS-based toolbox. *MethodsX*, 7, 101150. https://doi.org/10.1016/j.mex.2020.101150

Ong, B. L. (2003). Green plot ratio: An ecological measure for architecture and urban planning. *Landscape and Urban Planning*, 63, 197–211. https://doi.org/10.1016/S0169-2046(02)00191-3

Ouyang, W., et al. (2020). Optimal greenery abundance for thermal environment. *Building and Environment*, 174, 106772. https://doi.org/10.1016/j.buildenv.2020.106772

Parastatidis, D., Mitraka, Z., Chrysoulakis, N., & Abrams, M. (2017). Error sources on the land surface temperature retrieved from thermal infrared single channel remote sensing data. *International Journal of Remote Sensing*, 38(23), 6973–6993. https://doi.org/10.1080/01431161.2017.1368098

Pedregosa, F., Varoquaux, G., Gramfort, A., Michel, V., Thirion, B., Grisel, O., ... & Duchesnay, E. (2011). Scikit-learn: Machine learning in Python. *Journal of Machine Learning Research*, 12, 2825–2830.

Peng, J., Jia, J., Liu, Y., Li, H., & Wu, J. (2024). Global urban greening and its implication for urban heat mitigation. *Proceedings of the National Academy of Sciences*, 121(15), e2417179122. https://doi.org/10.1073/pnas.2417179122

Perkins, S. E., Alexander, L. V., & Nairn, J. R. (2012). Increasing frequency, intensity and duration of observed global heatwaves and warm spells. *Geophysical Research Letters*, 39(20), L20714. https://doi.org/10.1029/2012GL053361

Persson, C. (2013). Deliberation or doctrine? Land use and spatial planning for sustainable development in Sweden. *Land Use Policy*, 34, 301–313.

Posit Team. (2024). RStudio: Integrated development environment for R. Posit Software, PBC. http://www.posit.co/

Prado, R. T. A., & Ferreira, F. L. (2005). Measurement of albedo and analysis of its influence on the surface temperature of building roof materials. *Energy and Buildings*, 37(4), 295–300. https://doi.org/10.1016/j.enbuild.2004.03.009

Presiden Republik Indonesia. (2021). Peraturan Pemerintah Republik Indonesia Nomor 21 Tahun 2021 tentang Penyelenggaraan Penataan Ruang. [Government Regulation on Spatial Planning].

QGIS Development Team. (2024). QGIS Geographic Information System. QGIS Association. http://www.qgis.org

Radhi, H., Assem, E., & Sharples, S. (2014). On the colors and properties of building surface materials to mitigate urban heat islands in highly productive solar regions. *Building and Environment*, 72, 162–172. https://doi.org/10.1016/j.buildenv.2013.11.005

Radoux, J., Dominique, M., Hartley, A., Lamarche, C., Bos, A., & Defourny, P. (2025). Land cover types drive the surface temperature for upscaling surface urban heat islands with daylight images. *Remote Sensing*, 17(16), 2815. https://doi.org/10.3390/rs17162815

Republik Indonesia, Menteri Agraria dan Tata Ruang. (2021). Peraturan Menteri Agraria dan Tata Ruang Nomor 11 Tahun 2021. [Ministerial Regulation on Spatial Planning Procedures].

Roy, D. P., Kovalskyy, V., Zhang, H. K., Vermote, E. F., Yan, L., Kumar, S. S., & Egorov, A. (2016). Characterization of Landsat-7 to Landsat-8 reflective wavelength and normalized difference vegetation index continuity. *Remote Sensing of Environment*, 185, 57–70. https://doi.org/10.1016/j.rse.2015.12.024

Sánchez-Cordero, F., Nanía, L., Hidalgo-García, D., & López-Chacón, S. R. (2025). Assessing the spatial benefits of green roofs to mitigate urban heat island effects in a semi-arid city. *Remote Sensing*, 17(12), 2073. https://doi.org/10.3390/rs17122073

Santamouris, M. (2013). Using cool pavements as a mitigation strategy to fight urban heat island. *Renewable and Sustainable Energy Reviews*, 26, 224–240. https://doi.org/10.1016/j.rser.2013.05.047

Shao, L., et al. (2023). Study on UHI attribution using SHAP and ML models. *Building and Environment*, 242, 110581. https://doi.org/10.1016/j.buildenv.2023.110581

Sismanidis, P., Bechtel, B., Perry, M., & Ghent, D. (2022). The seasonality of surface urban heat islands across climates. Remote Sensing, 14(10), 2318. https://doi.org/10.3390/rs14102318

Siswanto, S., et al. (2023). UHI development and intensity measurement in Jakarta agglomeration. *Remote Sensing Applications: Society and Environment*, 32, 101062. https://doi.org/10.1016/j.rsase.2023.101062

Sobrino, J. A., Oltra-Carrió, R., Sòria, G., Jiménez-Muñoz, J. C., Franch, B., Hidalgo, V., Mattar, C., Julien, Y., Cuenca, J., Romaguera, M., Gómez, J. A., De Miguel, E., Bianchi, R., & Paganini, M. (2012). Evaluation of the surface urban heat island effect in the city of Madrid by thermal remote sensing. *International Journal of Remote Sensing*, 34(9–10), 3177–3192. https://doi.org/10.1080/01431161.2012.716548

Soliman, A., Mackay, A., Schmidt, A., Allan, B., & Wang, S. (2018). Quantifying the geographic distribution of building coverage across the US for urban sustainability studies. *Computers, Environment and Urban Systems*, 71, 199–208. https://doi.org/10.1016/j.compenvurbsys.2018.05.010

Sotoma, M., Miyazaki, H., Kyakuno, T., & Moriyama, M. (2003). Analysis of land use zoning regulations and green coverage ratio. *Journal of Asian Architecture and Building Engineering*, 2(2), b29–b34. https://doi.org/10.3130/jaabe.2.b29

Stache, E., Schilperoort, B., Ottelé, M., & Jonkers, H. M. (2022). Comparative analysis in thermal behaviour of common urban building materials and vegetation and consequences for urban heat island effect. *Building and Environment*, 213, 108489. https://doi.org/10.1016/j.buildenv.2021.108489

Stewart, I. D., & Oke, T. R. (2012). Local climate zones for urban temperature studies. *Bulletin of the American Meteorological Society*, 93(12), 1879–1900. https://doi.org/10.1175/BAMS-D-11-00019.1

Sun, Y., Gao, C., Li, J., Wang, R., & Liu, J. (2019). Quantifying the effects of urban form on land surface temperature in subtropical high-density urban areas using machine learning. *Remote Sensing*, 11(8), 959. https://doi.org/10.3390/rs11080959

Syafii, N.I., Ichinose, M., Kumakura, E., Jusuf, S.K., Hien, W.N., Chigusa, K., Ashie, Y., 2021. Assessment of the Water Pond Cooling Effect on Urban Microclimate: A Parametric Study with Numerical Modeling. International Journal of Technology. Volume 12(3), pp. 461-471. https://doi.org/10.14716/ijtech.v12i3.4126

Tardy, B., Rivalland, V., Huc, M., Hagolle, O., Marcq, S., & Boulet, G. (2016). A software tool for atmospheric correction and surface temperature estimation of Landsat infrared thermal data. Remote Sensing, 8(9), 696. https://doi.org/10.3390/rs8090696

Tegal City Government. (2022). Complete basic map scale 1:50,000 [Data set].

Tegal City Government. (2022). Orthophoto imagery in 50 cm resolution [Data set].

Trigo, I. F., Monteiro, I. T., Olesen, F., & Kabsch, E. (2008). An assessment of remotely sensed land surface temperature. *Journal of Geophysical Research*, 113, D17108. https://doi.org/10.1029/2008JD010035

Trisakti, B. (2017). Vegetation type classification and vegetation cover percentage estimation in urban green zone using Pleiades imagery. *IOP Conference Series: Earth and Environmental Science*, 54, 012003. https://doi.org/10.1088/1755-1315/54/1/012003

Trlica, A., Huemmrich, K. F., Gerace, A., Jesslyn, F., Cook, B. D., Montesano, P. M., & Loranty, M. M. (2017). Albedo, land cover, and daytime surface temperature variation across an urbanized landscape. *Earth's Future*, 5(10), 1084–1101. https://doi.org/10.1002/2017EF000569

U.S. Geological Survey. (2024). Landsat 8-9 Collection 2 Level 2 science product guide (LSDS-1619, Version 6.0). U.S. Department of the Interior.

USGS. (2015). Landsat 8 (L8) data users handbook. U.S. Geological Survey EROS.

Usui, H. (2021). Variation in building heights under zoning regulations of building coverage ratio and floor area ratio. In *ISUF 2020 Virtual Conference Proceedings* (Vol. 1). University of Utah.

Vermote, E. F., Justice, C. O., Claverie, M., & Franch, B. (2016). Analysis of the performance of the Landsat 8/OLI land surface reflectance product. *Remote Sensing of Environment*, 185, 46–56.

Wang, N., Wu, H., Nerry, F., Li, C. R., & Li, Z.-L. (2011). Temperature and emissivity retrievals from hyperspectral thermal infrared data using linear spectral emissivity constraint. *IEEE Transactions on Geoscience and Remote Sensing*, 49, 1291–1303.

Wang, Q., Bian, J., Hu, Z., Hu, T., & Chen, F. (2025). High-resolution urban heat island analysis using SDGSAT-1 thermal infrared and glimmer data. *International Journal of Digital Earth*, 18(2), 2553792. https://doi.org/10.1080/17538947.2024.2553792

Weng, Q., & Quattrochi, D. A. (2006). Urban remote sensing. *International Journal of Remote Sensing*, 27(22), 4957–4962. https://doi.org/10.1080/01431160600756650

Wilson, E., & Piper, J. (2010). *Spatial planning and climate change*. Routledge.

World Bank Group & Asian Development Bank. (2021). Climate risk country profile: Indonesia. https://www.adb.org/publications/climate-risk-country-profile-indonesia

Wu, Z., & Zhang, Y. (2019). Water bodies' cooling effects on urban land daytime surface temperature: Ecosystem service reducing heat island effect. *Sustainability*, 11(3), 787. https://doi.org/10.3390/su11030787

Wulder, M. A., Loveland, T. R., Roy, D. P., Crawford, C. J., Masek, J. G., Woodcock, C. E., Allen, R. G., Anderson, M. C., Belward, A. S., Cohen, W. B., et al. (2019). Current status of Landsat program, science, and applications. *Remote Sensing of Environment*, 225, 127–147. https://doi.org/10.1016/j.rse.2019.02.015

Xu, H., Chen, H., Zhou, X., Wu, Y., & Liu, Y. (2020). Research on the relationship between urban morphology and air temperature based on mobile measurement. *Urban Climate*, 34, 100671.

Xu, X., Pei, H., Wang, C., Xu, Q., Xie, H., Jin, Y., Feng, Y., Tong, X., & Xiao, C. (2023). Long-term analysis of the urban heat island effect using multisource Landsat images. *Science of the Total Environment*, 858, 159777. https://doi.org/10.1016/j.scitotenv.2022.159777

Yang, J., Zhan, Y., Xiao, X., Xia, J. C., Sun, W., & Li, X. (2020). Investigating the diversity of land surface temperature characteristics in different scale cities based on local climate zones. Urban Climate, 34, 100700. https://doi.org/10.1016/j.uclim.2020.100700

Yan, J., Yin, C., An, Z., Mu, B., Wen, Q., Li, Y., Zhang, Y., Chen, W., Wang, L., & Song, Y. (2023). The influence of urban form on land surface temperature: A comprehensive investigation from 2D urban land use and 3D buildings. *Land*, 12(9), 1802. https://doi.org/10.3390/land12091802

Yang, J., Xin, J., Zhang, Y., et al. (2022). Contributions of sea–land breeze and local climate zones to daytime and nighttime heat island intensity. *npj Urban Sustainability*, 2, 12. https://doi.org/10.1038/s42949-022-00055-z

Yang, Q., Xu, Y., Tong, X., Hu, T., Liu, Y., Chakraborty, T. C., Lee, X., & Ma, Z. (2023). Influence of urban extent discrepancy on the estimation of surface urban heat island intensity. *Journal of Cleaner Production*, 426, 139032. https://doi.org/10.1016/j.jclepro.2023.139032

Yang, Y., Pan, Z., Zhang, B., Huang, S., Chen, X., & Hong, T. (2025). Review of cooling effects from roof mitigation strategies against urban heat island effects. *Buildings*, 15(21), 3835. https://doi.org/10.3390/buildings15213835

Yao, R., Wang, L., Huang, X., Niu, Y., Chen, Y., & Niu, Z. (2018). The influence of different data and method on estimating the surface urban heat island intensity. *Ecological Indicators*, 89, 45–55.

Young, N. E., Anderson, R. S., Chignell, S. M., Vorster, A. G., Lawrence, R., & Evangelista, P. H. (2017). A survival guide to Landsat preprocessing. *Ecology*, 98(4), 920–932. https://doi.org/10.1002/ecy.1730

Yuan, Y., Santamouris, M., Xu, D., Geng, X., Li, C., Cheng, W., Su, L., Xiong, P., Fan, Z., & Wang, X. (2025). Surface urban heat island effects intensify more rapidly in lower income countries. *npj Urban Sustainability*, 5(1), 1–11. https://doi.org/10.1038/s42949-025-00198-9

Zhang, J., Tu, L., & Shi, B. (2023). Spatiotemporal patterns of the application of surface urban heat island intensity calculation methods. *Atmosphere*, 14(10), 1580. https://doi.org/10.3390/atmos14101580

Zheng, J., Li, Z., & Zheng, B. (2024). A study on the effect of green plot ratio (GPR) on urban heat island intensity and outdoor thermal comfort in residential areas. *Forests*, 15(3), 518. https://doi.org/10.3390/f15030518

Zhou, M., Wang, R., & Guo, Y. (2024). How urban spatial characteristics impact surface urban heat island in subtropical high-density cities based on LCZs: A case study of Macau. Sustainable Cities and Society, 112, 105587. https://doi.org/10.1016/j.scs.2024.105587

Zhou, W., Qian, Y., Li, X., Li, W., & Han, L. (2014). Relationships between land cover and the surface urban heat island. *Landscape Ecology*, 29(1), 153–167. https://doi.org/10.1007/s10980-013-9950-5

Zhou, Y., Zhao, H., Mao, S., Zhang, G., Jin, Y., Luo, Y., Huo, W., Pan, Z., An, P., & Lun, F. (2022). Exploring surface urban heat island (SUHI) intensity and its implications based on urban 3D neighborhood metrics. *Science of the Total Environment*, 847, 157662. https://doi.org/10.1016/j.scitotenv.2022.157662

Appendices

1. Figures

a) LST on October 9, 2023

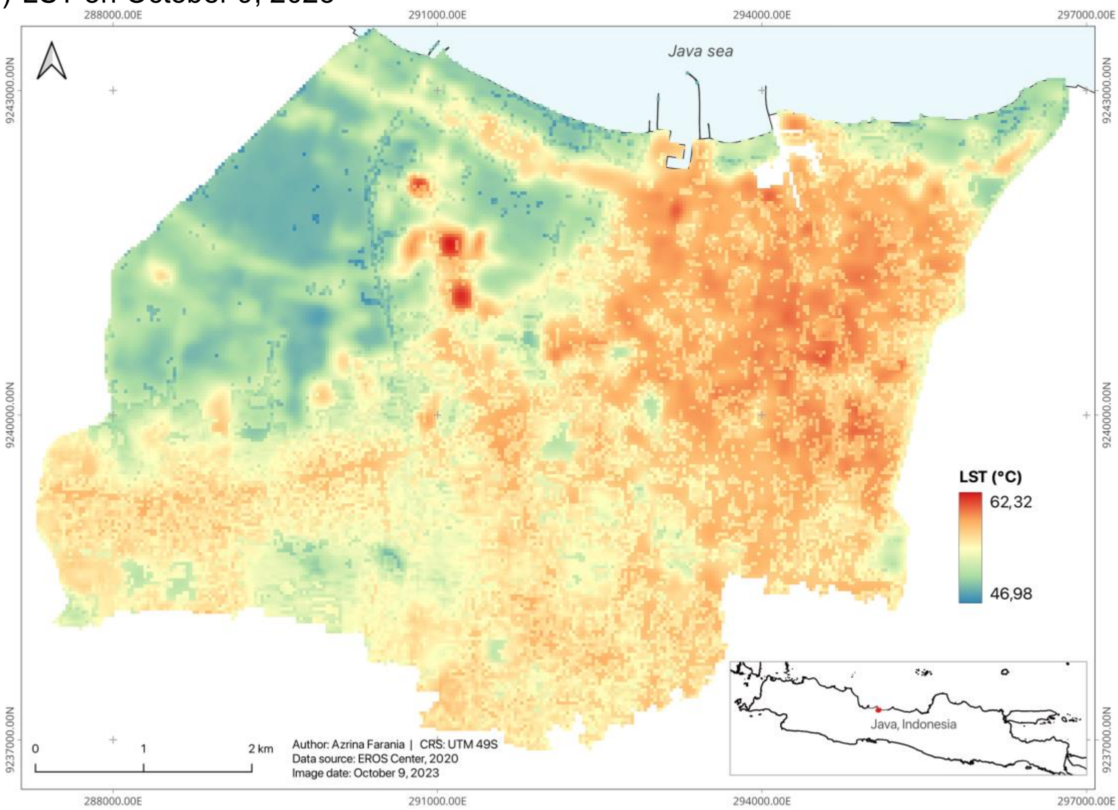

b) LST on October 17, 2023

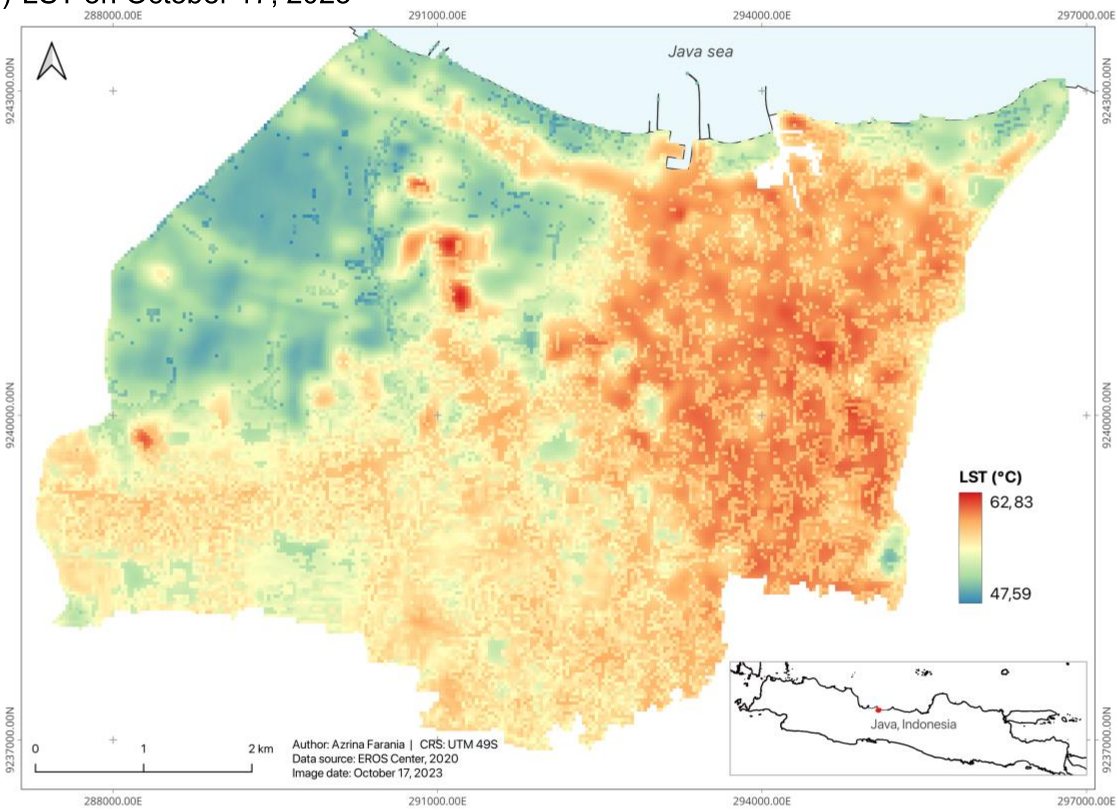

c) LST on December 12, 2023

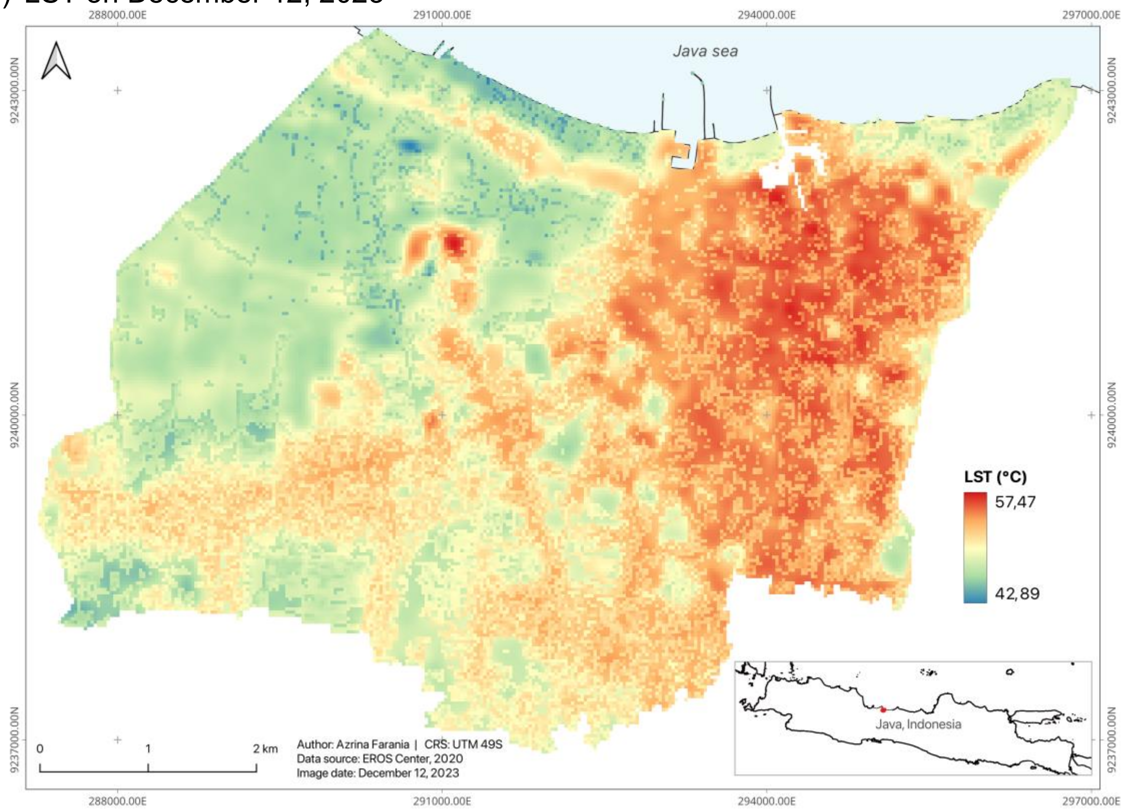

d) LST on September 25, 2024

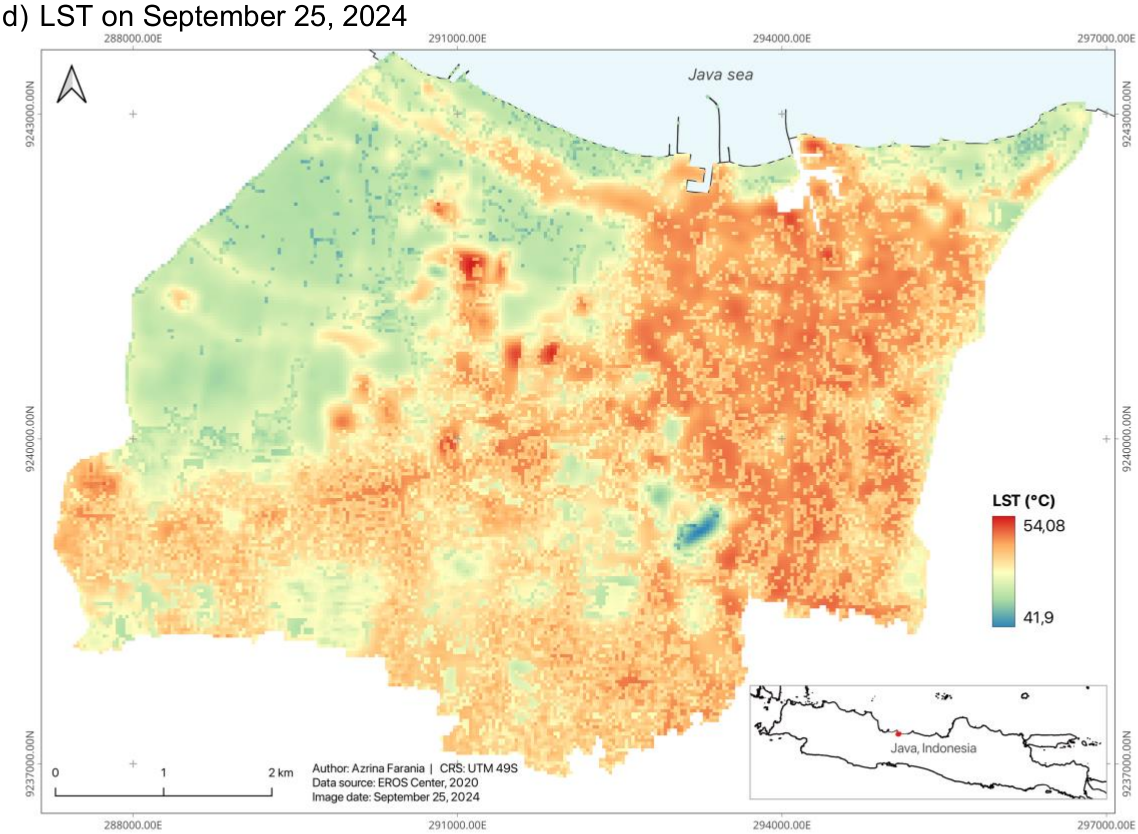

e) LST on October 27, 2024

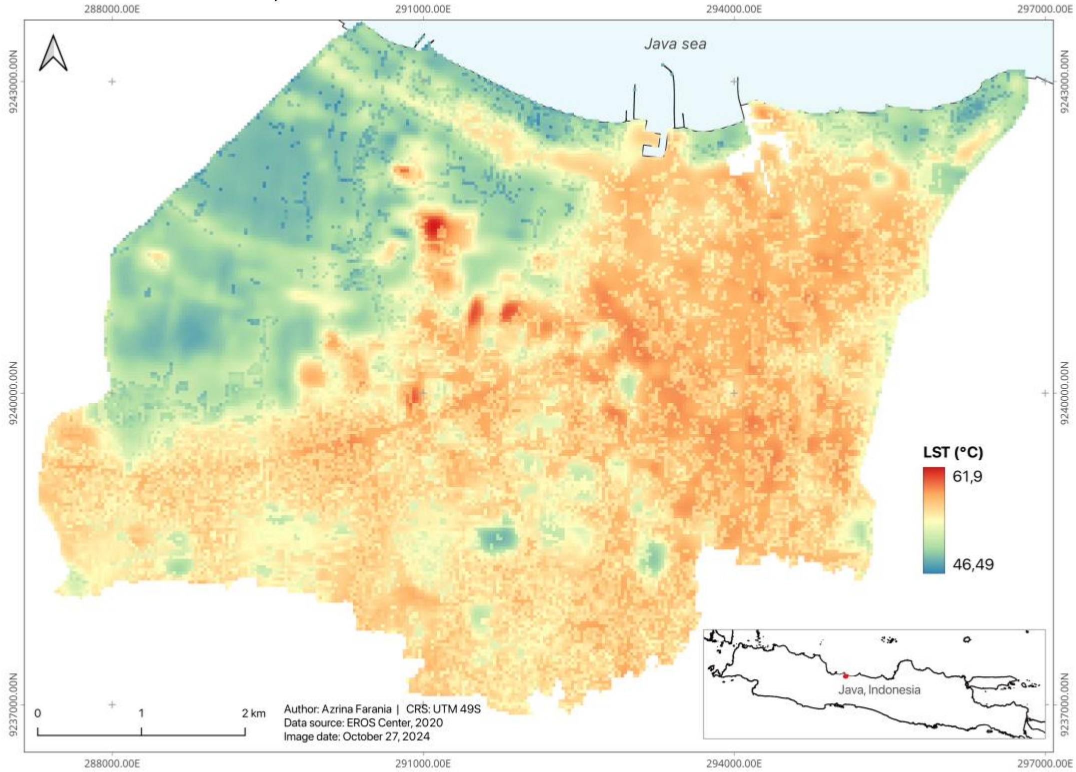

Figure A: LST Distribution During Multi-Heatwave Periods in Tegal City using original scale ranges on a) October 9, 2023, b) October 17, 2023, c) December 12, 2023, and d) September 25, 2023, e) October 27, 2024.

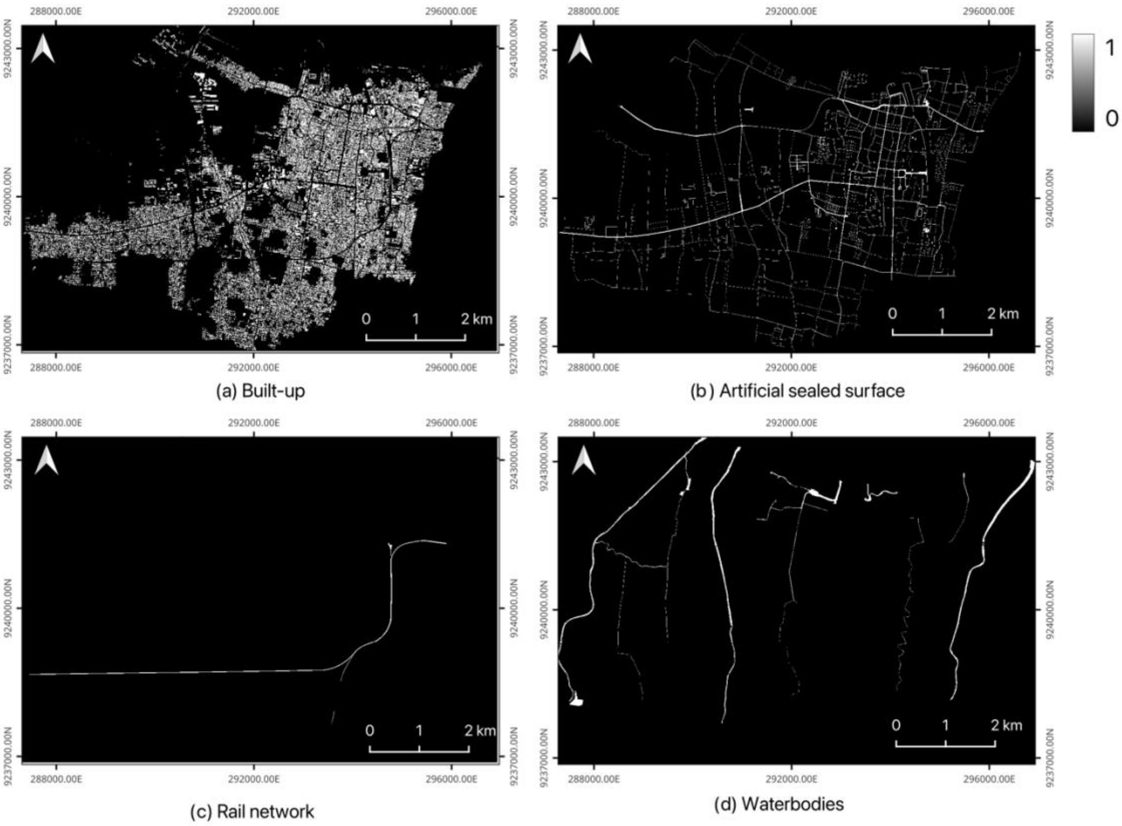

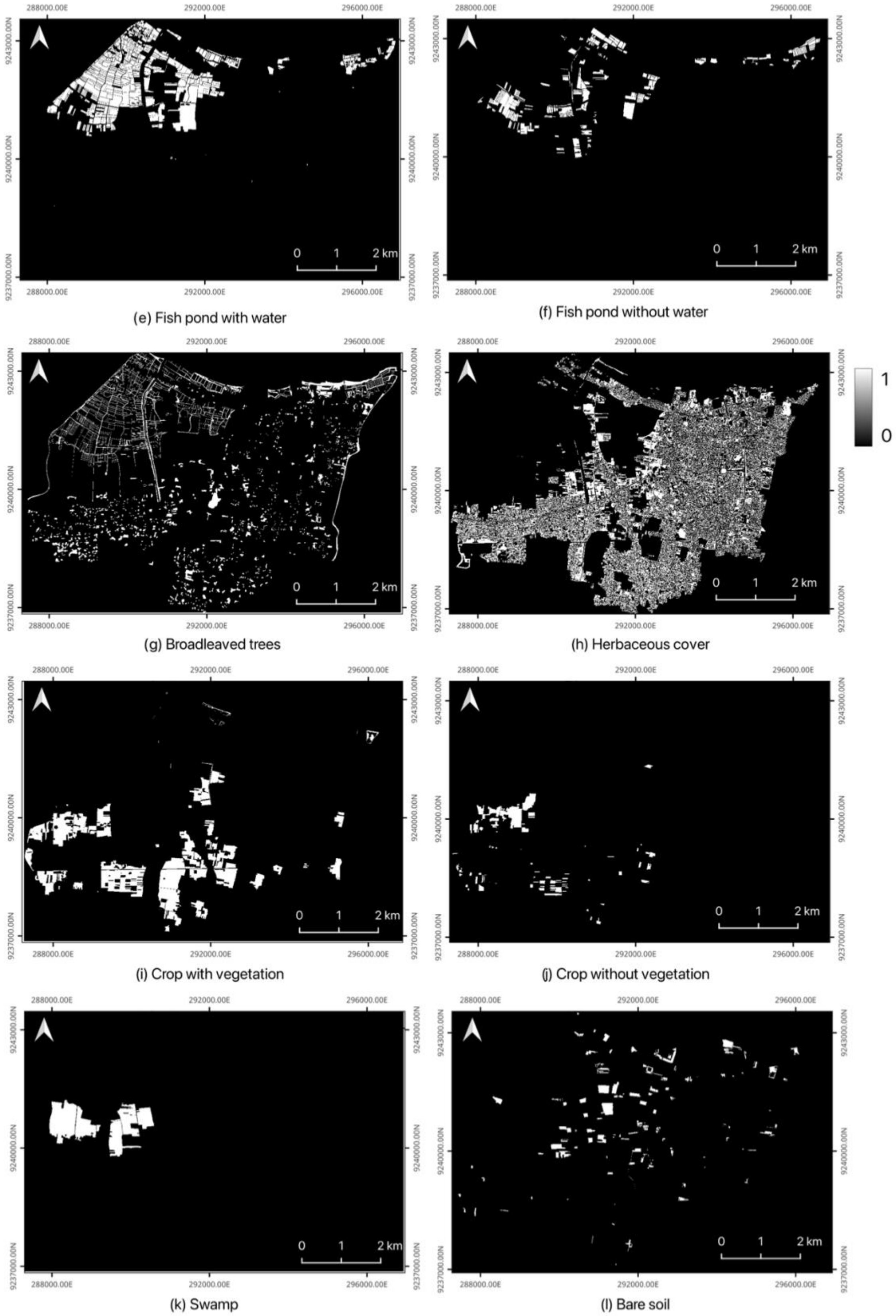

Figure B: Binary land cover fraction maps for 12 individual classes in Tegal City at 0.5 m resolution, derived from the updated land cover map: (a) built up, (b) artificial sealed surface, (c) rail network, (d) waterbodies, (e) fish pond with water, (f) fish pond without water, (g) broadleaved trees, (h) herbaceous cover, (i) crop with vegetation, (j) crop without vegetation, (k) swamp, and (l) bare soil. White pixels (value = 1) indicate the presence of each class; black pixels (value = 0) indicate absence. CRS: UTM Zone 49S.

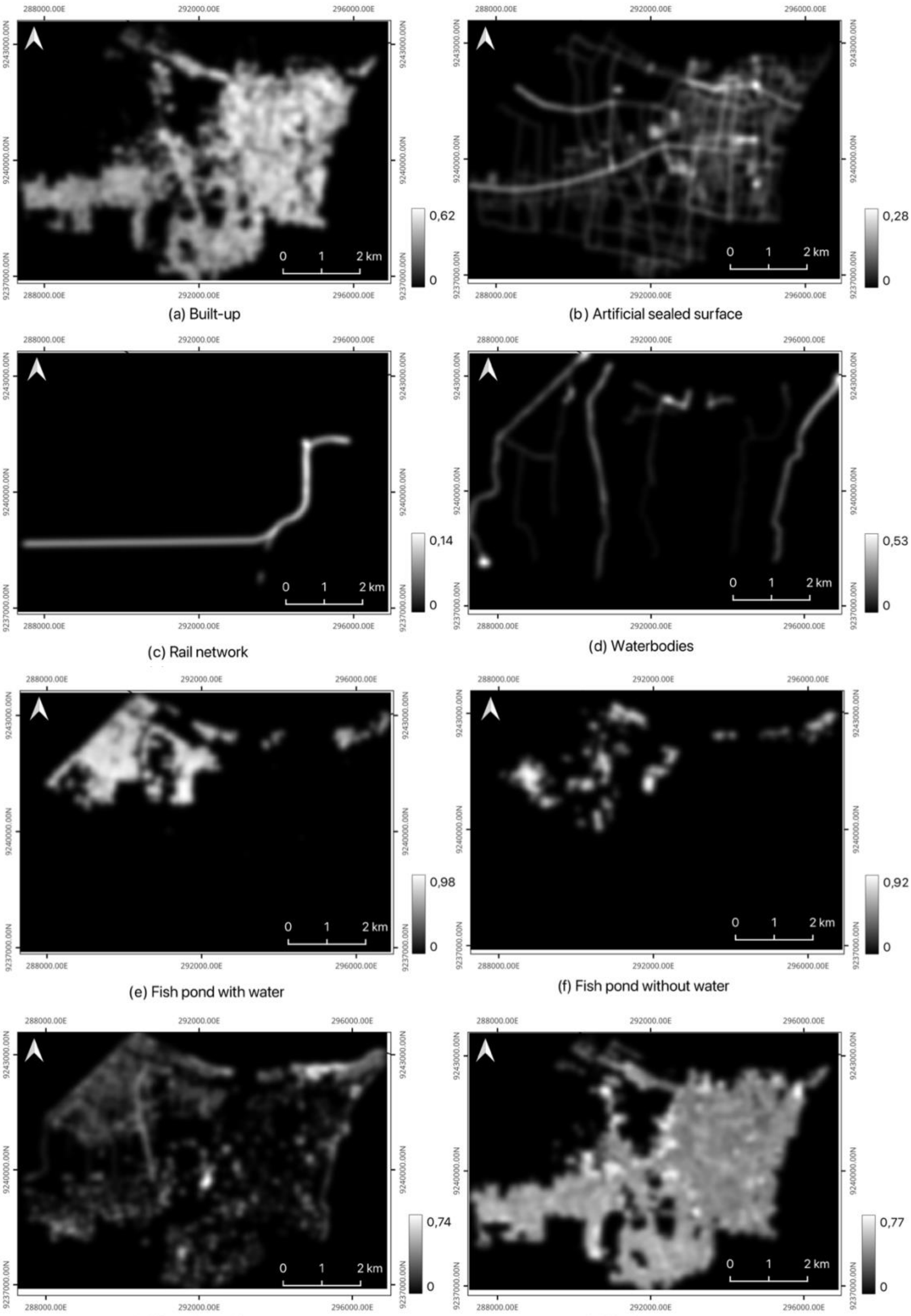

(a) Built-up
(b) Artificial sealed surface
(c) Rail network
(d) Waterbodies
(e) Fish pond with water
(f) Fish pond without water
(g) Broadleaved trees
(h) Herbaceous cover

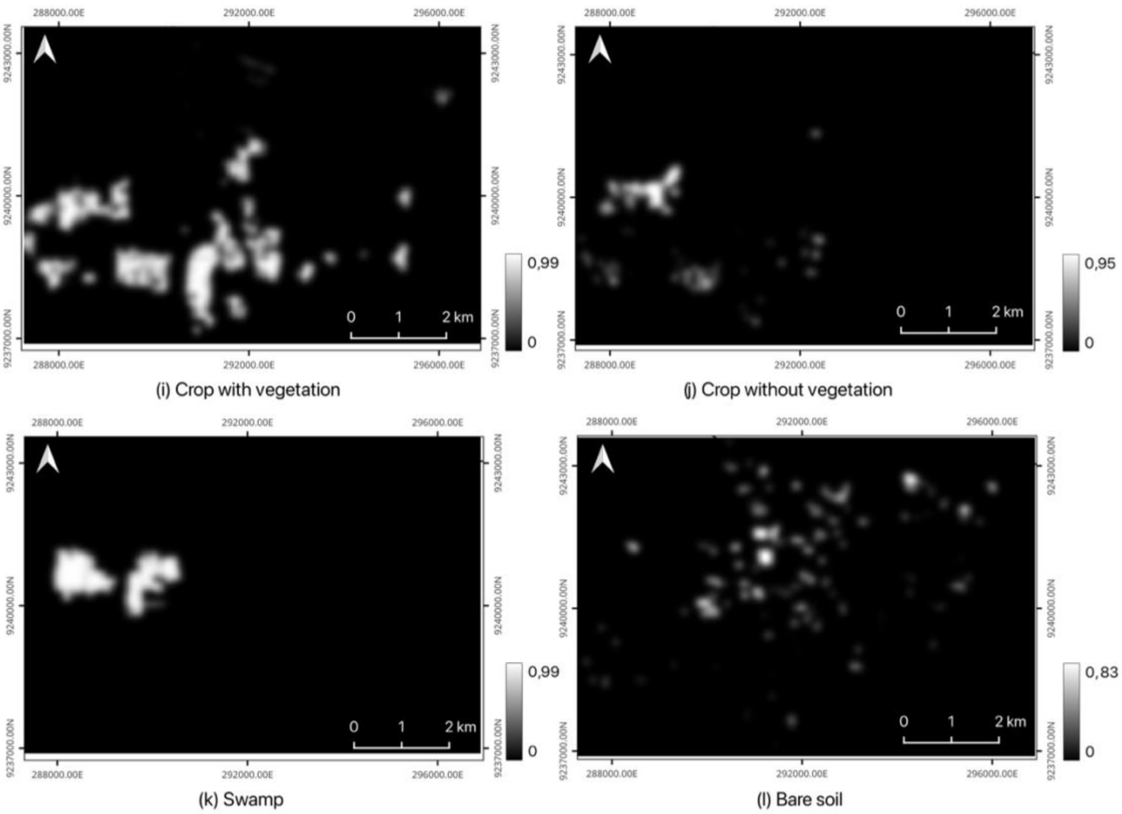

Figure C: PSF-weighted land cover fraction maps for 12 individual classes in Tegal City at 30 m resolution after PSF convolution, used as input to the linear mixed model: (a) built-up, (b) artificial sealed surface, (c) rail network, (d) waterbodies, (e) fish pond with water, (f) fish pond without water, (g) broadleaved trees, (h) herbaceous cover, (i) crop with vegetation, (j) crop without vegetation, (k) swamp, and (l) bare soil. CRS: UTM Zone 49S.

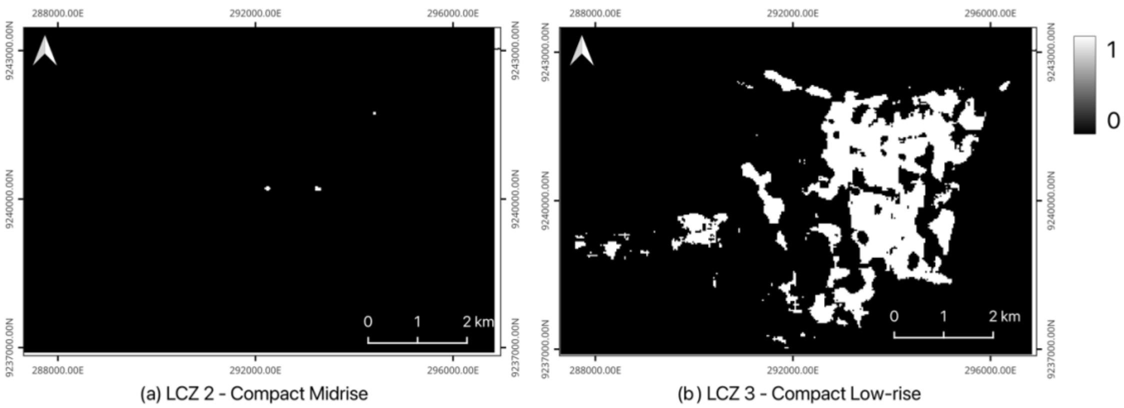

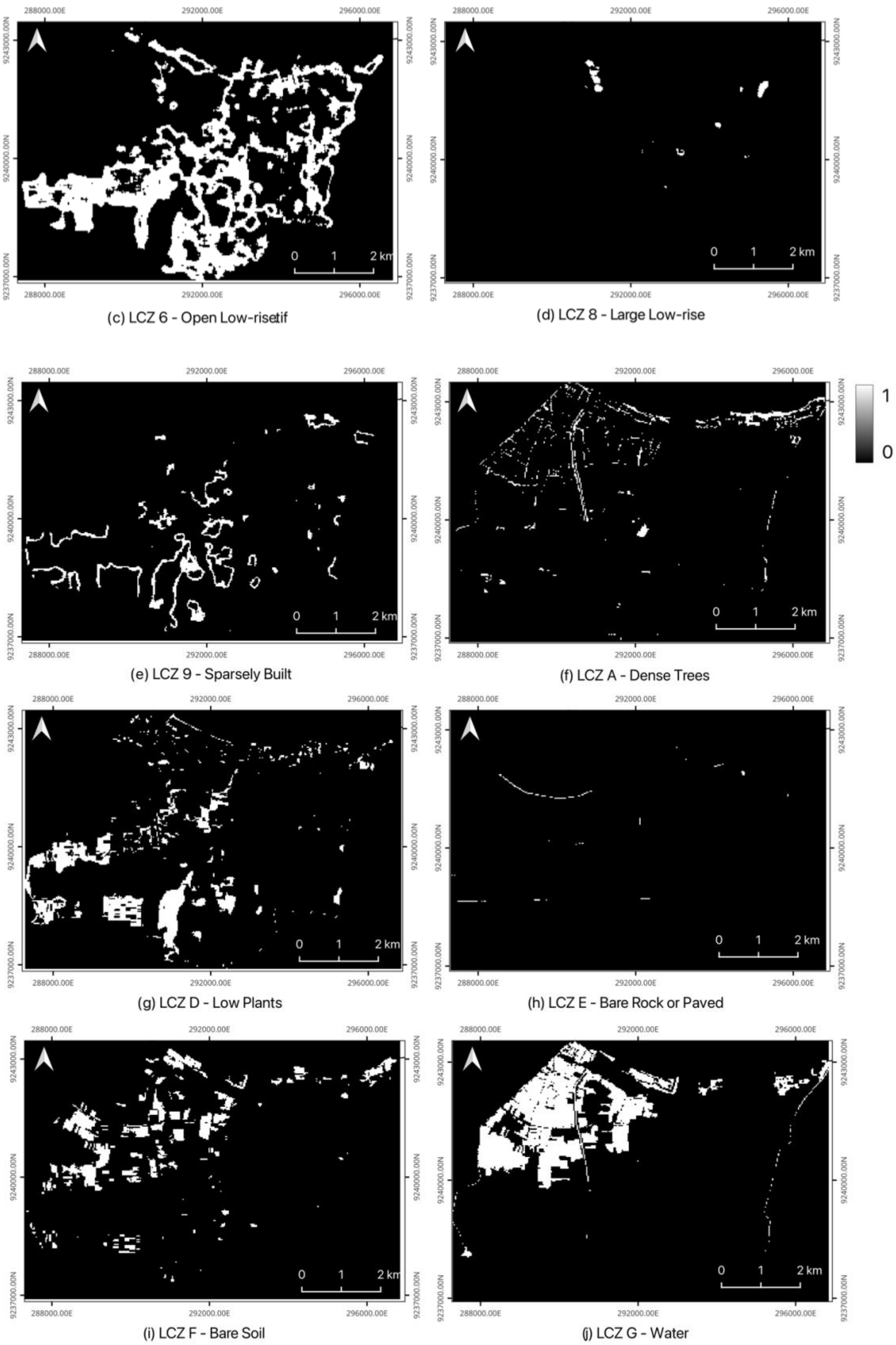

Figure D: Binary LCZ maps for 10 classes in Tegal City at 30 m resolution: (a) LCZ 2 – Compact Mid-rise, (b) LCZ 3 – Compact Low-rise, (c) LCZ 6 – Open Low-rise, (d) LCZ 8 – Large Low-rise, (e) LCZ 9 – Sparsely Built, (f) LCZ A – Dense Trees, (g) LCZ D – Low Plants, (h) LCZ E – Bare Rock or Paved, (i) LCZ F – Bare Soil, and (j) LCZ G – Water. White pixels (value = 1) indicate the presence of each class; black pixels (value = 0) indicate absence. CRS: UTM Zone 49S.

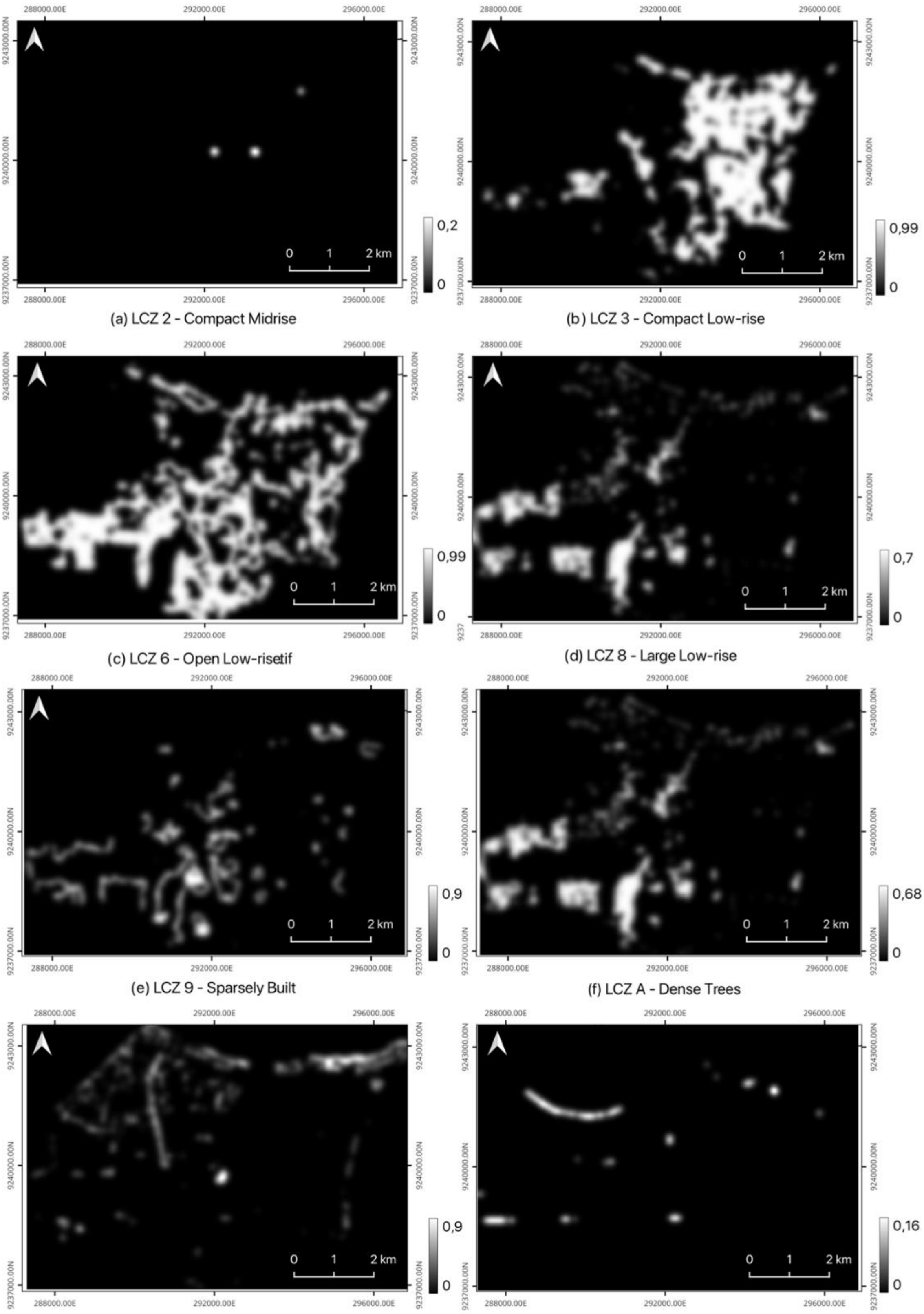

(a) LCZ 2 - Compact Midrise
(b) LCZ 3 - Compact Low-rise
(c) LCZ 6 - Open Low-risetif
(d) LCZ 8 - Large Low-rise
(e) LCZ 9 - Sparsely Built
(f) LCZ A - Dense Trees
(g) LCZ D - Low Plants
(h) LCZ E - Bare Rock or Paved

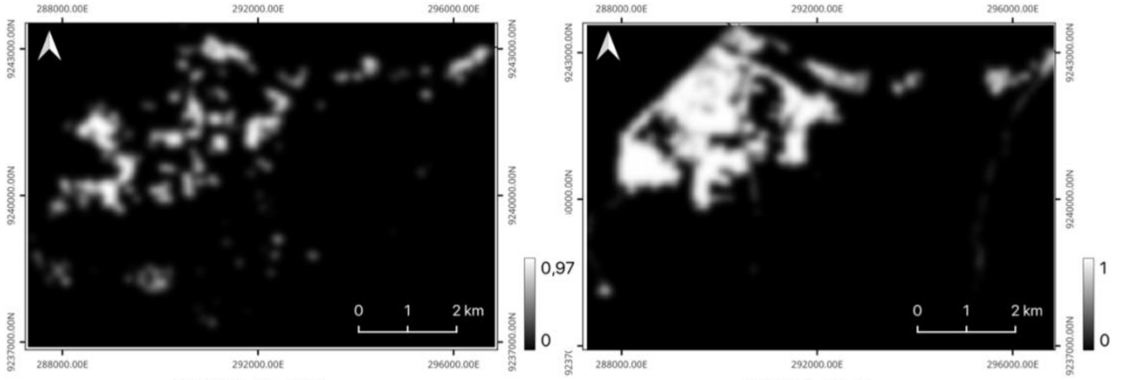

(i) LCZ F - Bare Soil (j) LCZ G - Water

Figure E: PSF-weighted LCZ fraction maps for 10 classes in Tegal City at 30 m resolution, used as input to the linear mixed model: (a) LCZ 2 – Compact Mid-rise, (b) LCZ 3 – Compact Low-rise, (c) LCZ 6 – Open Low-rise, (d) LCZ 8 – Large Low-rise, (e) LCZ 9 – Sparsely Built, (f) LCZ A – Dense Trees, (g) LCZ D – Low Plants, (h) LCZ E – Bare Rock or Paved, (i) LCZ F – Bare Soil, and (j) LCZ G – Water. Pixel values represent the Gaussian PSF-weighted fraction of each LCZ class. CRS: UTM Zone 49S.

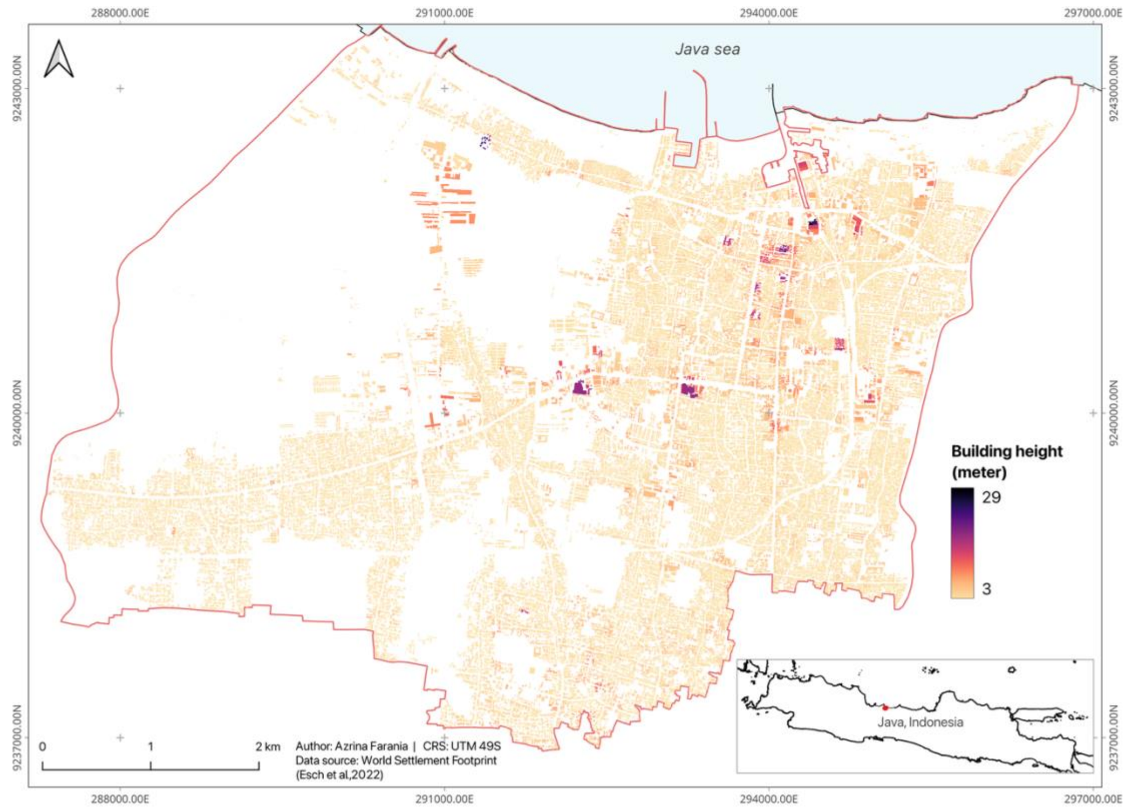

Figure F: Building height distribution in Tegal City (3–29 m), derived from the World Settlement Footprint 3D dataset (WSF3D; Esch et al., 2022) with manual correction to the building layer. The majority of buildings are low-rise (3–5 m), with taller structures concentrated in the urban core.

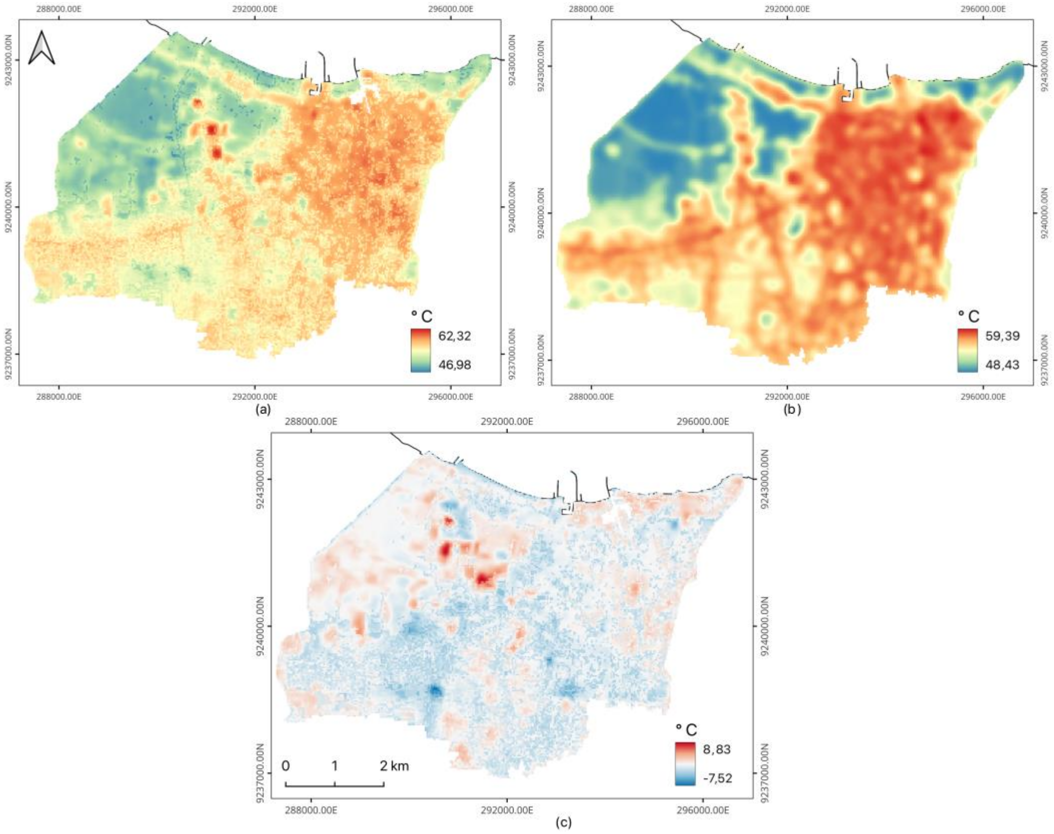

Figure G: Comparison of (a) observed LST from Landsat 8/9 TIRS, (b) reconstructed LST from the Land Cover linear mixed model, and (c) residual LST (observed minus reconstructed) in Tegal City on October 9, 2023. Positive residuals (red) indicate areas where the model underestimates LST and negative residuals (blue) indicate overestimation.

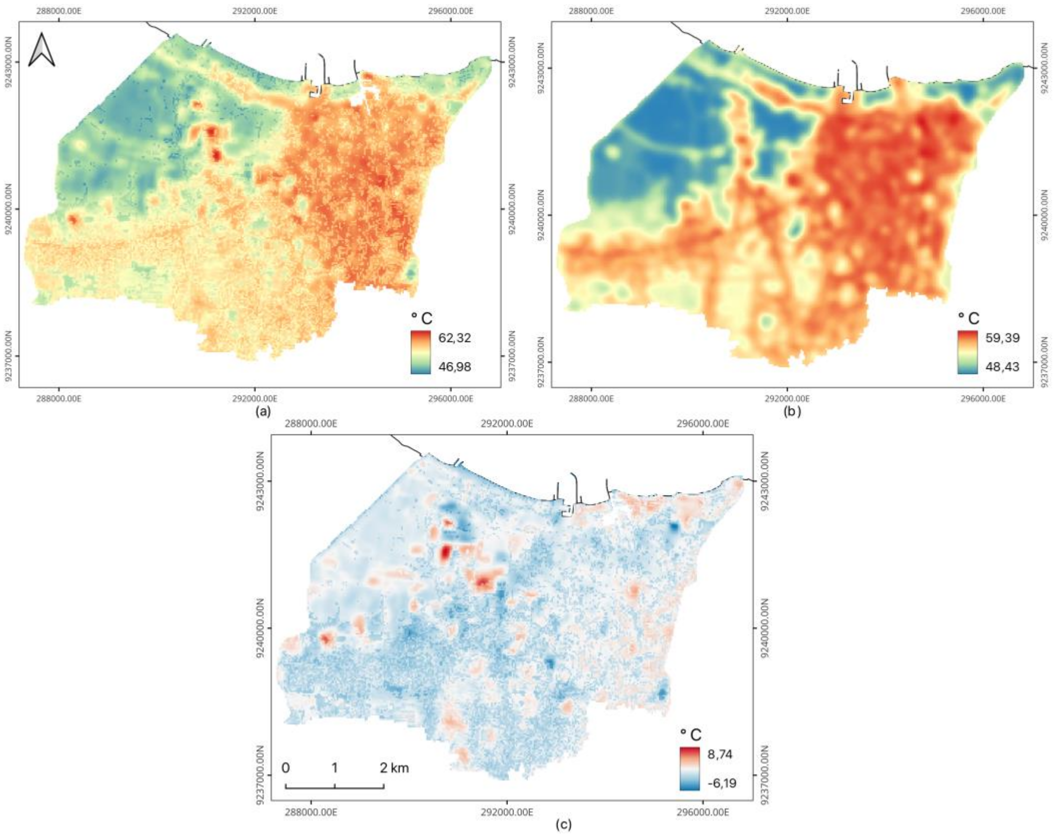

Figure H: Comparison of (a) observed LST from Landsat 8/9 TIRS, (b) reconstructed LST from the Land Cover linear mixed model, and (c) residual LST (observed minus reconstructed) in Tegal City on October 17, 2023. Positive residuals (red) indicate areas where the model underestimates LST and negative residuals (blue) indicate overestimation.

Figure I: Orthophoto Image of Tegal City in 2022

2. Table

Table A: Sample Distribution of Land Cover Map Accuracy Assessment

Class ID	Land Cover Class Name	Proportion (%)	Samples (out of 600)
1	Built up	21.94	130
2	Artificial sealed surface	3.92	24
3	Rail network	0.44	3
4	Waterbodies	2.01	12
5	Fish pond with water	10.97	66
6	Fish pond without water	4.17	25
7	Broadleaved trees	8.76	53
8	Herbaceous cover	29.10	175
9	Crop without vegetation	1.97	12
10	Crop with vegetation	10.09	61
11	Swamp	3.99	24
12	Bare soil	2.64	15
	TOTAL	**100**	**600**

Table B: Sample Distribution of Roofing Material Map Accuracy Assessment

Class ID	Roof Material Name	Proportion (%)	Samples (out of 200)
1	Concrete	0.25	3*
2	Metal	17.11	33
3	Tile/Clay	82.09	161
4	Unplasticized Polyvinyl Chloride (uPVC)	0.55	3*
	TOTAL		**200**

*number is adjusted to add significancy of the sample

Table C: Urban Morphology Fraction, Roofing Material Fraction and Coastal Proximity Value Distribution Across Heatwave Dates

Sample ID	Date	Roofing Material				Urban Morphology				Coastal Proximity (meter)	LST anomaly (°C) All date	LST anomaly (°C) Residuals
		Concrete Fraction	uPVC Fraction	Metal Fraction	Tile/Clay Fraction	BSF	ISF	PSF	SVF			
S1	23/09/23	0	0.39	0.25	0.36	0.44	0.1	0.46	0.9959	2217.09	-0.95	-0.12
S2	23/09/23	0.39	0	0.31	0.3	0.51	0.11	0.38	0.9969	2098.27	1.26	0.08
S3	23/09/23	0.01	0.75	0.01	0.23	0.29	0.2	0.5	0.9996	1834.74	-0.42	-0.93
S4	23/09/23	0	0.65	0	0.35	0.47	0.09	0.44	0.9995	2364.13	-1.11	-0.7
S5	23/09/23	0	0	0.81	0.19	0.6	0.05	0.35	0.9986	946.8	0.54	0.14
S6	23/09/23	0	0	0.66	0.34	0.57	0.08	0.35	0.9983	1640.98	2.19	1.26
S7	23/09/23	0	0	0.97	0.03	0.42	0.02	0.56	0.9981	865.12	-4.88	-3.68
S8	23/09/23	0	0.48	0.05	0.47	0.27	0.06	0.66	0.9996	3205.31	-2.9	0.68
S9	23/09/23	0.12	0	0.52	0.36	0.42	0.01	0.57	0.9988	1899.57	-1.22	-0.49
S10	23/09/23	0	0	0.55	0.45	0.35	0.19	0.46	0.9994	2497.08	-0.63	-0.01
S11	23/09/23	0	0	0.47	0.53	0.46	0.04	0.5	0.9983	3709.63	-1.15	-1
S12	23/09/23	0	0	0.21	0.79	0.6	0.07	0.33	0.9995	851.51	1.52	0.19
S13	23/09/23	0	0	0.55	0.45	0.5	0.09	0.41	0.9979	2500.17	0.39	-0.02
S14	23/09/23	0	0	0.01	0.99	0.46	0.02	0.52	0.9997	4108.29	-1.4	-0.53
S15	23/09/23	0	0	0.51	0.49	0.47	0.11	0.42	0.9993	459.51	-1.93	-1.13
S16	23/09/23	0	0	0.58	0.42	0.57	0.14	0.29	0.9986	968.1	1.27	0.11
S17	23/09/23	0	0	0.34	0.66	0.52	0.05	0.44	0.9994	2671.17	-0.4	0.39
S18	23/09/23	0	0	0.09	0.91	0.51	0.03	0.46	0.9995	3260.63	-0.02	0.69
S19	23/09/23	0	0	0.58	0.42	0.46	0.06	0.47	0.9988	647.69	0.59	0.18
S20	23/09/23	0	0	0.27	0.73	0.48	0.08	0.44	0.9992	3480.52	0.02	0.25
S21	23/09/23	0	0	0.41	0.59	0.45	0.14	0.41	0.9991	1675.94	1.05	-0.08
S22	23/09/23	0.41	0.02	0.26	0.3	0.24	0.11	0.65	0.9987	1749.76	0.42	1.21
S23	23/09/23	0	0	0.67	0.33	0.39	0.1	0.51	0.9979	2662.38	1.48	1.35

Sample ID	Date	Roofing Material				Urban Morphology				Coastal Proximity (meter)	LST anomaly (°C) All date	LST anomaly (°C) Residuals
		Concrete Fraction	uPVC Fraction	Metal Fraction	Tile/Clay Fraction	BSF	ISF	PSF	SVF			
S24	23/09/23	0	0	0.19	0.81	0.62	0.03	0.35	0.9992	494.75	0.95	0.33
S25	23/09/23	0	0	0.19	0.81	0.46	0.11	0.44	0.9995	2880.54	0.08	0.62
S26	23/09/23	0	0	0.66	0.34	0.49	0.04	0.47	0.9980	2975.35	-2.55	-2.95
S27	23/09/23	0	0	0.1	0.9	0.61	0.03	0.36	0.9995	1648.56	0.81	0.31
S28	23/09/23	0	0	0.31	0.69	0.52	0.07	0.41	0.9994	2978.27	0.09	0.25
S29	23/09/23	0	0	0.34	0.66	0.56	0.03	0.41	0.9990	1329.69	1.51	0.95
S30	23/09/23	0	0	0.51	0.49	0.48	0.07	0.45	0.9976	946.9	1.07	0.91
S31	23/09/23	0	0	0.12	0.88	0.45	0.05	0.5	0.9993	4099.65	-0.7	-0.26
S32	23/09/23	0	0	0.08	0.92	0.55	0.07	0.38	0.9996	1547.68	1.37	0.97
S33	23/09/23	0	0	0.23	0.77	0.6	0.04	0.37	0.9992	996.73	1.25	0.59
S34	23/09/23	0	0	0.06	0.94	0.46	0.03	0.51	0.9994	4797.44	-0.74	-0.45
S35	23/09/23	0	0	0.41	0.59	0.47	0.04	0.48	0.9992	142.44	0.73	0.46
S36	23/09/23	0	0	0.26	0.74	0.58	0.04	0.38	0.9995	726.6	0.86	0.19
S37	23/09/23	0	0	0.11	0.89	0.55	0.07	0.38	0.9996	2705.5	0.49	0.58
S38	23/09/23	0	0	0.27	0.73	0.57	0.07	0.35	0.9990	1129.26	1.2	0.63
S39	23/09/23	0	0	0.02	0.98	0.49	0.03	0.48	0.9993	4578.38	-0.44	0.24
S40	23/09/23	0	0	0.13	0.87	0.62	0.05	0.34	0.9995	1245.95	0.89	0.48
S41	23/09/23	0	0	0.29	0.71	0.5	0.04	0.46	0.9986	1980.51	1.25	0.59
S42	23/09/23	0	0	0.39	0.61	0.43	0.08	0.49	0.9993	2407.54	0.41	0.82
S43	23/09/23	0	0	0.51	0.49	0.36	0.03	0.61	0.9993	2013.37	-0.67	0.68
S44	23/09/23	0	0	0	1	0.44	0.01	0.54	0.9997	3787.43	-1.55	-0.44
S45	23/09/23	0	0	0.1	0.9	0.51	0.05	0.44	0.9993	1312.87	0.9	0.54
S46	23/09/23	0	0	0.1	0.9	0.58	0.04	0.38	0.9995	3115.62	1.33	0.68
S47	23/09/23	0	0	0.25	0.75	0.47	0.04	0.49	0.9994	1127.16	0.51	0.99

Sample ID	Date	Roofing Material				Urban Morphology				Coastal Proximity (meter)	LST anomaly (°C) All date	LST anomaly (°C) Residuals
		Concrete Fraction	uPVC Fraction	Metal Fraction	Tile/Clay Fraction	BSF	ISF	PSF	SVF			
S48	23/09/23	0	0	0.85	0.15	0.27	0.02	0.71	0.9992	1393.86	-3.42	-1.01
S49	23/09/23	0	0	0.1	0.9	0.58	0.02	0.39	0.9994	2468.73	1.38	1.01
S50	23/09/23	0	0	0.2	0.8	0.42	0.09	0.49	0.9994	2971.81	-0.83	0.06
S1	09/10/23	0	0.39	0.25	0.36	0.44	0.1	0.46	0.9959	2217.09	-1.13	-0.58
S2	09/10/23	0.39	0	0.31	0.3	0.51	0.11	0.38	0.9969	2098.27	0.9	0.41
S3	09/10/23	0.01	0.75	0.01	0.23	0.29	0.2	0.5	0.9996	1834.74	-1.28	-0.63
S4	09/10/23	0	0.65	0	0.35	0.47	0.09	0.44	0.9995	2364.13	-1.61	-0.79
S5	09/10/23	0	0	0.81	0.19	0.6	0.05	0.35	0.9986	946.8	0.42	-0.2
S6	09/10/23	0	0	0.66	0.34	0.57	0.08	0.35	0.9983	1640.98	2.66	1.02
S7	09/10/23	0	0	0.97	0.03	0.42	0.02	0.56	0.9981	865.12	-5.87	-2.16
S8	09/10/23	0	0.48	0.05	0.47	0.27	0.06	0.66	0.9996	3205.31	-2.68	-0.51
S9	09/10/23	0.12	0	0.52	0.36	0.42	0.01	0.57	0.9988	1899.57	-1.13	-0.65
S10	09/10/23	0	0	0.55	0.45	0.35	0.19	0.46	0.9994	2497.08	-0.24	-0.92
S11	09/10/23	0	0	0.47	0.53	0.46	0.04	0.5	0.9983	3709.63	-2.03	-1.03
S12	09/10/23	0	0	0.21	0.79	0.6	0.07	0.33	0.9995	851.51	0.79	0.33
S13	09/10/23	0	0	0.55	0.45	0.5	0.09	0.41	0.9979	2500.17	0.19	-0.18
S14	09/10/23	0	0	0.01	0.99	0.46	0.02	0.52	0.9997	4108.29	-1.42	-1.31
S15	09/10/23	0	0	0.51	0.49	0.47	0.11	0.42	0.9993	459.51	-2.67	-1.14
S16	09/10/23	0	0	0.58	0.42	0.57	0.14	0.29	0.9986	968.1	2.14	0.05
S17	09/10/23	0	0	0.34	0.66	0.52	0.05	0.44	0.9994	2671.17	0.83	-0.8
S18	09/10/23	0	0	0.09	0.91	0.51	0.03	0.46	0.9995	3260.63	0.59	-0.27
S19	09/10/23	0	0	0.58	0.42	0.46	0.06	0.47	0.9988	647.69	0.65	0.2
S20	09/10/23	0	0	0.27	0.73	0.48	0.08	0.44	0.9992	3480.52	0.85	-0.53
S21	09/10/23	0	0	0.41	0.59	0.45	0.14	0.41	0.9991	1675.94	1.15	0.05

Sample ID	Date	Roofing Material				Urban Morphology				Coastal Proximity (meter)	LST anomaly (°C) All date	LST anomaly (°C) Residuals
		Concrete Fraction	uPVC Fraction	Metal Fraction	Tile/Clay Fraction	BSF	ISF	PSF	SVF			
S22	09/10/23	0.41	0.02	0.26	0.3	0.24	0.11	0.65	0.9987	1749.76	-0.52	0.91
S23	09/10/23	0	0	0.67	0.33	0.39	0.1	0.51	0.9979	2662.38	1.02	1.12
S24	09/10/23	0	0	0.19	0.81	0.62	0.03	0.35	0.9992	494.75	0.02	0.06
S25	09/10/23	0	0	0.19	0.81	0.46	0.11	0.44	0.9995	2880.54	-0.14	-0.35
S26	09/10/23	0	0	0.66	0.34	0.49	0.04	0.47	0.9980	2975.35	-3.26	-2.63
S27	09/10/23	0	0	0.1	0.9	0.61	0.03	0.36	0.9995	1648.56	0.46	-0.02
S28	09/10/23	0	0	0.31	0.69	0.52	0.07	0.41	0.9994	2978.27	0.89	-0.72
S29	09/10/23	0	0	0.34	0.66	0.56	0.03	0.41	0.9990	1329.69	1.86	0.69
S30	09/10/23	0	0	0.51	0.49	0.48	0.07	0.45	0.9976	946.9	2.12	0.59
S31	09/10/23	0	0	0.12	0.88	0.45	0.05	0.5	0.9993	4099.65	-0.83	-0.66
S32	09/10/23	0	0	0.08	0.92	0.55	0.07	0.38	0.9996	1547.68	1.82	0.56
S33	09/10/23	0	0	0.23	0.77	0.6	0.04	0.37	0.9992	996.73	1.66	0.45
S34	09/10/23	0	0	0.06	0.94	0.46	0.03	0.51	0.9994	4797.44	-1.61	-0.49
S35	09/10/23	0	0	0.41	0.59	0.47	0.04	0.48	0.9992	142.44	-0.4	0.36
S36	09/10/23	0	0	0.26	0.74	0.58	0.04	0.38	0.9995	726.6	1.6	0.02
S37	09/10/23	0	0	0.11	0.89	0.55	0.07	0.38	0.9996	2705.5	1.13	-0.31
S38	09/10/23	0	0	0.27	0.73	0.57	0.07	0.35	0.9990	1129.26	2.19	0.06
S39	09/10/23	0	0	0.02	0.98	0.49	0.03	0.48	0.9993	4578.38	-0.75	-0.61
S40	09/10/23	0	0	0.13	0.87	0.62	0.05	0.34	0.9995	1245.95	0.83	-0.1
S41	09/10/23	0	0	0.29	0.71	0.5	0.04	0.46	0.9986	1980.51	1.08	0.62
S42	09/10/23	0	0	0.39	0.61	0.43	0.08	0.49	0.9993	2407.54	1.06	0.47
S43	09/10/23	0	0	0.51	0.49	0.36	0.03	0.61	0.9993	2013.37	-0.66	0.68
S44	09/10/23	0	0	0	1	0.44	0.01	0.54	0.9997	3787.43	-1.22	-1.31
S45	09/10/23	0	0	0.1	0.9	0.51	0.05	0.44	0.9993	1312.87	1.52	0.37

Sample ID	Date	Roofing Material				Urban Morphology				Coastal Proximity (meter)	LST anomaly (°C) All date	LST anomaly (°C) Residuals
		Concrete Fraction	uPVC Fraction	Metal Fraction	Tile/Clay Fraction	BSF	ISF	PSF	SVF			
S46	09/10/23	0	0	0.1	0.9	0.58	0.04	0.38	0.9995	3115.62	1.58	0.66
S47	09/10/23	0	0	0.25	0.75	0.47	0.04	0.49	0.9994	1127.16	1.06	0.32
S48	09/10/23	0	0	0.85	0.15	0.27	0.02	0.71	0.9992	1393.86	-5.1	0.05
S49	09/10/23	0	0	0.1	0.9	0.58	0.02	0.39	0.9994	2468.73	1.77	0.77
S50	09/10/23	0	0	0.2	0.8	0.42	0.09	0.49	0.9994	2971.81	-0.12	-0.68
S1	17/10/23	0	0.39	0.25	0.36	0.44	0.1	0.46	0.9959	2217.09	-0.77	-0.25
S2	17/10/23	0.39	0	0.31	0.3	0.51	0.11	0.38	0.9969	2098.27	1.38	0.67
S3	17/10/23	0.01	0.75	0.01	0.23	0.29	0.2	0.5	0.9996	1834.74	-0.83	-0.89
S4	17/10/23	0	0.65	0	0.35	0.47	0.09	0.44	0.9995	2364.13	-0.99	-0.52
S5	17/10/23	0	0	0.81	0.19	0.6	0.05	0.35	0.9986	946.8	-0.41	-1
S6	17/10/23	0	0	0.66	0.34	0.57	0.08	0.35	0.9983	1640.98	2.29	1.27
S7	17/10/23	0	0	0.97	0.03	0.42	0.02	0.56	0.9981	865.12	-5.28	-2.41
S8	17/10/23	0	0.48	0.05	0.47	0.27	0.06	0.66	0.9996	3205.31	-3.35	-0.82
S9	17/10/23	0.12	0	0.52	0.36	0.42	0.01	0.57	0.9988	1899.57	-0.89	-0.17
S10	17/10/23	0	0	0.55	0.45	0.35	0.19	0.46	0.9994	2497.08	0.41	0.27
S11	17/10/23	0	0	0.47	0.53	0.46	0.04	0.5	0.9983	3709.63	-1.78	-1.51
S12	17/10/23	0	0	0.21	0.79	0.6	0.07	0.33	0.9995	851.51	1.5	0.45
S13	17/10/23	0	0	0.55	0.45	0.5	0.09	0.41	0.9979	2500.17	0.48	0.06
S14	17/10/23	0	0	0.01	0.99	0.46	0.02	0.52	0.9997	4108.29	-1.96	-1.72
S15	17/10/23	0	0	0.51	0.49	0.47	0.11	0.42	0.9993	459.51	-1.96	-1.01
S16	17/10/23	0	0	0.58	0.42	0.57	0.14	0.29	0.9986	968.1	0.69	-0.38
S17	17/10/23	0	0	0.34	0.66	0.52	0.05	0.44	0.9994	2671.17	0.62	0.36
S18	17/10/23	0	0	0.09	0.91	0.51	0.03	0.46	0.9995	3260.63	0.87	0.77
S19	17/10/23	0	0	0.58	0.42	0.46	0.06	0.47	0.9988	647.69	0.12	-0.12

Sample ID	Date	Roofing Material				Urban Morphology				Coastal Proximity (meter)	LST anomaly (°C) All date	LST anomaly (°C) Residuals
		Concrete Fraction	uPVC Fraction	Metal Fraction	Tile/Clay Fraction	BSF	ISF	PSF	SVF			
S20	17/10/23	0	0	0.27	0.73	0.48	0.08	0.44	0.9992	3480.52	0.93	0.54
S21	17/10/23	0	0	0.41	0.59	0.45	0.14	0.41	0.9991	1675.94	1.17	0.32
S22	17/10/23	0.41	0.02	0.26	0.3	0.24	0.11	0.65	0.9987	1749.76	0.48	1.12
S23	17/10/23	0	0	0.67	0.33	0.39	0.1	0.51	0.9979	2662.38	1.9	1.7
S24	17/10/23	0	0	0.19	0.81	0.62	0.03	0.35	0.9992	494.75	0.75	0.01
S25	17/10/23	0	0	0.19	0.81	0.46	0.11	0.44	0.9995	2880.54	-0.38	-0.66
S26	17/10/23	0	0	0.66	0.34	0.49	0.04	0.47	0.9980	2975.35	-2.97	-2.9
S27	17/10/23	0	0	0.1	0.9	0.61	0.03	0.36	0.9995	1648.56	1.1	0.42
S28	17/10/23	0	0	0.31	0.69	0.52	0.07	0.41	0.9994	2978.27	1.22	0.55
S29	17/10/23	0	0	0.34	0.66	0.56	0.03	0.41	0.9990	1329.69	1.22	0.56
S30	17/10/23	0	0	0.51	0.49	0.48	0.07	0.45	0.9976	946.9	0.66	0.33
S31	17/10/23	0	0	0.12	0.88	0.45	0.05	0.5	0.9993	4099.65	-1.15	-0.95
S32	17/10/23	0	0	0.08	0.92	0.55	0.07	0.38	0.9996	1547.68	1.28	0.62
S33	17/10/23	0	0	0.23	0.77	0.6	0.04	0.37	0.9992	996.73	1.24	0.59
S34	17/10/23	0	0	0.06	0.94	0.46	0.03	0.51	0.9994	4797.44	-1.25	-0.85
S35	17/10/23	0	0	0.41	0.59	0.47	0.04	0.48	0.9992	142.44	0.21	-0.01
S36	17/10/23	0	0	0.26	0.74	0.58	0.04	0.38	0.9995	726.6	0.68	-0.01
S37	17/10/23	0	0	0.11	0.89	0.55	0.07	0.38	0.9996	2705.5	1.76	1.12
S38	17/10/23	0	0	0.27	0.73	0.57	0.07	0.35	0.9990	1129.26	0.84	-0.15
S39	17/10/23	0	0	0.02	0.98	0.49	0.03	0.48	0.9993	4578.38	-0.78	-0.8
S40	17/10/23	0	0	0.13	0.87	0.62	0.05	0.34	0.9995	1245.95	1.28	0.44
S41	17/10/23	0	0	0.29	0.71	0.5	0.04	0.46	0.9986	1980.51	1.17	0.69
S42	17/10/23	0	0	0.39	0.61	0.43	0.08	0.49	0.9993	2407.54	0.77	0.98
S43	17/10/23	0	0	0.51	0.49	0.36	0.03	0.61	0.9993	2013.37	-0.53	0.97

Sample ID	Date	Roofing Material				Urban Morphology				Coastal Proximity (meter)	LST anomaly (°C) All date	LST anomaly (°C) Residuals
		Concrete Fraction	uPVC Fraction	Metal Fraction	Tile/Clay Fraction	BSF	ISF	PSF	SVF			
S44	17/10/23	0	0	0	1	0.44	0.01	0.54	0.9997	3787.43	-2.22	-1.83
S45	17/10/23	0	0	0.1	0.9	0.51	0.05	0.44	0.9993	1312.87	1.05	0.67
S46	17/10/23	0	0	0.1	0.9	0.58	0.04	0.38	0.9995	3115.62	1.83	1.31
S47	17/10/23	0	0	0.25	0.75	0.47	0.04	0.49	0.9994	1127.16	0.68	0.64
S48	17/10/23	0	0	0.85	0.15	0.27	0.02	0.71	0.9992	1393.86	-4.94	-1.32
S49	17/10/23	0	0	0.1	0.9	0.58	0.02	0.39	0.9994	2468.73	1.83	1.38
S50	17/10/23	0	0	0.2	0.8	0.42	0.09	0.49	0.9994	2971.81	0.13	0.43
S1	12/12/23	0	0.39	0.25	0.36	0.44	0.1	0.46	0.9959	2217.09	-0.77	
S2	12/12/23	0.39	0	0.31	0.3	0.51	0.11	0.38	0.9969	2098.27	0.65	
S3	12/12/23	0.01	0.75	0.01	0.23	0.29	0.2	0.5	0.9996	1834.74	-1	
S4	12/12/23	0	0.65	0	0.35	0.47	0.09	0.44	0.9995	2364.13	-1.31	
S5	12/12/23	0	0	0.81	0.19	0.6	0.05	0.35	0.9986	946.8	0.59	
S6	12/12/23	0	0	0.66	0.34	0.57	0.08	0.35	0.9983	1640.98	2.14	
S7	12/12/23	0	0	0.97	0.03	0.42	0.02	0.56	0.9981	865.12	-6.69	
S8	12/12/23	0	0.48	0.05	0.47	0.27	0.06	0.66	0.9996	3205.31	-2	
S9	12/12/23	0.12	0	0.52	0.36	0.42	0.01	0.57	0.9988	1899.57	-1.35	
S10	12/12/23	0	0	0.55	0.45	0.35	0.19	0.46	0.9994	2497.08	-0.01	
S11	12/12/23	0	0	0.47	0.53	0.46	0.04	0.5	0.9983	3709.63	-1.4	
S12	12/12/23	0	0	0.21	0.79	0.6	0.07	0.33	0.9995	851.51	1.1	
S13	12/12/23	0	0	0.55	0.45	0.5	0.09	0.41	0.9979	2500.17	0.27	
S14	12/12/23	0	0	0.01	0.99	0.46	0.02	0.52	0.9997	4108.29	-0.91	
S15	12/12/23	0	0	0.51	0.49	0.47	0.11	0.42	0.9993	459.51	-2.21	
S16	12/12/23	0	0	0.58	0.42	0.57	0.14	0.29	0.9986	968.1	1.05	
S17	12/12/23	0	0	0.34	0.66	0.52	0.05	0.44	0.9994	2671.17	0.51	

Sample ID	Date	Roofing Material				Urban Morphology				Coastal Proximity (meter)	LST anomaly (°C) All date	LST anomaly (°C) Residuals
		Concrete Fraction	uPVC Fraction	Metal Fraction	Tile/Clay Fraction	BSF	ISF	PSF	SVF			
S18	12/12/23	0	0	0.09	0.91	0.51	0.03	0.46	0.9995	3260.63	0.65	
S19	12/12/23	0	0	0.58	0.42	0.46	0.06	0.47	0.9988	647.69	0.27	
S20	12/12/23	0	0	0.27	0.73	0.48	0.08	0.44	0.9992	3480.52	0.51	
S21	12/12/23	0	0	0.41	0.59	0.45	0.14	0.41	0.9991	1675.94	0.63	
S22	12/12/23	0.41	0.02	0.26	0.3	0.24	0.11	0.65	0.9987	1749.76	0.42	
S23	12/12/23	0	0	0.67	0.33	0.39	0.1	0.51	0.9979	2662.38	1.41	
S24	12/12/23	0	0	0.19	0.81	0.62	0.03	0.35	0.9992	494.75	0.94	
S25	12/12/23	0	0	0.19	0.81	0.46	0.11	0.44	0.9995	2880.54	0.76	
S26	12/12/23	0	0	0.66	0.34	0.49	0.04	0.47	0.9980	2975.35	-3.16	
S27	12/12/23	0	0	0.1	0.9	0.61	0.03	0.36	0.9995	1648.56	0.86	
S28	12/12/23	0	0	0.31	0.69	0.52	0.07	0.41	0.9994	2978.27	0.78	
S29	12/12/23	0	0	0.34	0.66	0.56	0.03	0.41	0.9990	1329.69	1.48	
S30	12/12/23	0	0	0.51	0.49	0.48	0.07	0.45	0.9976	946.9	1.1	
S31	12/12/23	0	0	0.12	0.88	0.45	0.05	0.5	0.9993	4099.65	-0.59	
S32	12/12/23	0	0	0.08	0.92	0.55	0.07	0.38	0.9996	1547.68	1.49	
S33	12/12/23	0	0	0.23	0.77	0.6	0.04	0.37	0.9992	996.73	1.1	
S34	12/12/23	0	0	0.06	0.94	0.46	0.03	0.51	0.9994	4797.44	-0.99	
S35	12/12/23	0	0	0.41	0.59	0.47	0.04	0.48	0.9992	142.44	0.54	
S36	12/12/23	0	0	0.26	0.74	0.58	0.04	0.38	0.9995	726.6	0.73	
S37	12/12/23	0	0	0.11	0.89	0.55	0.07	0.38	0.9996	2705.5	1.08	
S38	12/12/23	0	0	0.27	0.73	0.57	0.07	0.35	0.9990	1129.26	1.48	
S39	12/12/23	0	0	0.02	0.98	0.49	0.03	0.48	0.9993	4578.38	0.12	
S40	12/12/23	0	0	0.13	0.87	0.62	0.05	0.34	0.9995	1245.95	1.18	
S41	12/12/23	0	0	0.29	0.71	0.5	0.04	0.46	0.9986	1980.51	0.93	

Sample ID	Date	Roofing Material				Urban Morphology				Coastal Proximity (meter)	LST anomaly (°C) All date	LST anomaly (°C) Residuals
		Concrete Fraction	uPVC Fraction	Metal Fraction	Tile/Clay Fraction	BSF	ISF	PSF	SVF			
S42	12/12/23	0	0	0.39	0.61	0.43	0.08	0.49	0.9993	2407.54	0.47	
S43	12/12/23	0	0	0.51	0.49	0.36	0.03	0.61	0.9993	2013.37	-0.96	
S44	12/12/23	0	0	0	1	0.44	0.01	0.54	0.9997	3787.43	-0.96	
S45	12/12/23	0	0	0.1	0.9	0.51	0.05	0.44	0.9993	1312.87	0.78	
S46	12/12/23	0	0	0.1	0.9	0.58	0.04	0.38	0.9995	3115.62	1.07	
S47	12/12/23	0	0	0.25	0.75	0.47	0.04	0.49	0.9994	1127.16	0.89	
S48	12/12/23	0	0	0.85	0.15	0.27	0.02	0.71	0.9992	1393.86	-4.76	
S49	12/12/23	0	0	0.1	0.9	0.58	0.02	0.39	0.9994	2468.73	1.33	
S50	12/12/23	0	0	0.2	0.8	0.42	0.09	0.49	0.9994	2971.81	-0.38	
S1	25/09/24	0	0.39	0.25	0.36	0.44	0.1	0.46	0.9959	2217.09	-0.3	
S2	25/09/24	0.39	0	0.31	0.3	0.51	0.11	0.38	0.9969	2098.27	0.74	
S3	25/09/24	0.01	0.75	0.01	0.23	0.29	0.2	0.5	0.9996	1834.74	-0.28	
S4	25/09/24	0	0.65	0	0.35	0.47	0.09	0.44	0.9995	2364.13	0.13	
S5	25/09/24	0	0	0.81	0.19	0.6	0.05	0.35	0.9986	946.8	-0.1	
S6	25/09/24	0	0	0.66	0.34	0.57	0.08	0.35	0.9983	1640.98	1.37	
S7	25/09/24	0	0	0.97	0.03	0.42	0.02	0.56	0.9981	865.12	-3.42	
S8	25/09/24	0	0.48	0.05	0.47	0.27	0.06	0.66	0.9996	3205.31	-0.72	
S9	25/09/24	0.12	0	0.52	0.36	0.42	0.01	0.57	0.9988	1899.57	-1.13	
S10	25/09/24	0	0	0.55	0.45	0.35	0.19	0.46	0.9994	2497.08	-0.33	
S11	25/09/24	0	0	0.47	0.53	0.46	0.04	0.5	0.9983	3709.63	-0.77	
S12	25/09/24	0	0	0.21	0.79	0.6	0.07	0.33	0.9995	851.51	1.05	
S13	25/09/24	0	0	0.55	0.45	0.5	0.09	0.41	0.9979	2500.17	0.13	
S14	25/09/24	0	0	0.01	0.99	0.46	0.02	0.52	0.9997	4108.29	-0.47	
S15	25/09/24	0	0	0.51	0.49	0.47	0.11	0.42	0.9993	459.51	-1	

Sample ID	Date	Roofing Material				Urban Morphology				Coastal Proximity (meter)	LST anomaly (°C) All date	LST anomaly (°C) Residuals
		Concrete Fraction	uPVC Fraction	Metal Fraction	Tile/Clay Fraction	BSF	ISF	PSF	SVF			
S16	25/09/24	0	0	0.58	0.42	0.57	0.14	0.29	0.9986	968.1	0.91	
S17	25/09/24	0	0	0.34	0.66	0.52	0.05	0.44	0.9994	2671.17	0.12	
S18	25/09/24	0	0	0.09	0.91	0.51	0.03	0.46	0.9995	3260.63	0.67	
S19	25/09/24	0	0	0.58	0.42	0.46	0.06	0.47	0.9988	647.69	0.29	
S20	25/09/24	0	0	0.27	0.73	0.48	0.08	0.44	0.9992	3480.52	0.88	
S21	25/09/24	0	0	0.41	0.59	0.45	0.14	0.41	0.9991	1675.94	0.52	
S22	25/09/24	0.41	0.02	0.26	0.3	0.24	0.11	0.65	0.9987	1749.76	-0.53	
S23	25/09/24	0	0	0.67	0.33	0.39	0.1	0.51	0.9979	2662.38	0.76	
S24	25/09/24	0	0	0.19	0.81	0.62	0.03	0.35	0.9992	494.75	0.74	
S25	25/09/24	0	0	0.19	0.81	0.46	0.11	0.44	0.9995	2880.54	0.61	
S26	25/09/24	0	0	0.66	0.34	0.49	0.04	0.47	0.9980	2975.35	-3.1	
S27	25/09/24	0	0	0.1	0.9	0.61	0.03	0.36	0.9995	1648.56	0.76	
S28	25/09/24	0	0	0.31	0.69	0.52	0.07	0.41	0.9994	2978.27	0.71	
S29	25/09/24	0	0	0.34	0.66	0.56	0.03	0.41	0.9990	1329.69	0.91	
S30	25/09/24	0	0	0.51	0.49	0.48	0.07	0.45	0.9976	946.9	0.9	
S31	25/09/24	0	0	0.12	0.88	0.45	0.05	0.5	0.9993	4099.65	-0.21	
S32	25/09/24	0	0	0.08	0.92	0.55	0.07	0.38	0.9996	1547.68	0.93	
S33	25/09/24	0	0	0.23	0.77	0.6	0.04	0.37	0.9992	996.73	0.86	
S34	25/09/24	0	0	0.06	0.94	0.46	0.03	0.51	0.9994	4797.44	-0.34	
S35	25/09/24	0	0	0.41	0.59	0.47	0.04	0.48	0.9992	142.44	0.51	
S36	25/09/24	0	0	0.26	0.74	0.58	0.04	0.38	0.9995	726.6	0.43	
S37	25/09/24	0	0	0.11	0.89	0.55	0.07	0.38	0.9996	2705.5	0.95	
S38	25/09/24	0	0	0.27	0.73	0.57	0.07	0.35	0.9990	1129.26	0.93	
S39	25/09/24	0	0	0.02	0.98	0.49	0.03	0.48	0.9993	4578.38	0.18	

Sample ID	Date	Roofing Material				Urban Morphology				Coastal Proximity (meter)	LST anomaly (°C) All date	LST anomaly (°C) Residuals
		Concrete Fraction	uPVC Fraction	Metal Fraction	Tile/Clay Fraction	BSF	ISF	PSF	SVF			
S40	25/09/24	0	0	0.13	0.87	0.62	0.05	0.34	0.9995	1245.95	1	
S41	25/09/24	0	0	0.29	0.71	0.5	0.04	0.46	0.9986	1980.51	0.63	
S42	25/09/24	0	0	0.39	0.61	0.43	0.08	0.49	0.9993	2407.54	0.05	
S43	25/09/24	0	0	0.51	0.49	0.36	0.03	0.61	0.9993	2013.37	-0.93	
S44	25/09/24	0	0	0	1	0.44	0.01	0.54	0.9997	3787.43	-0.5	
S45	25/09/24	0	0	0.1	0.9	0.51	0.05	0.44	0.9993	1312.87	0.83	
S46	25/09/24	0	0	0.1	0.9	0.58	0.04	0.38	0.9995	3115.62	0.92	
S47	25/09/24	0	0	0.25	0.75	0.47	0.04	0.49	0.9994	1127.16	0.28	
S48	25/09/24	0	0	0.85	0.15	0.27	0.02	0.71	0.9992	1393.86	-2.98	
S49	25/09/24	0	0	0.1	0.9	0.58	0.02	0.39	0.9994	2468.73	0.72	
S50	25/09/24	0	0	0.2	0.8	0.42	0.09	0.49	0.9994	2971.81	-4.27	
S1	27/10/24	0	0.39	0.25	0.36	0.44	0.1	0.46	0.9959	2217.09	0.18	
S2	27/10/24	0.39	0	0.31	0.3	0.51	0.11	0.38	0.9969	2098.27	1.25	
S3	27/10/24	0.01	0.75	0.01	0.23	0.29	0.2	0.5	0.9996	1834.74	0.4	
S4	27/10/24	0	0.65	0	0.35	0.47	0.09	0.44	0.9995	2364.13	0.31	
S5	27/10/24	0	0	0.81	0.19	0.6	0.05	0.35	0.9986	946.8	-0.61	
S6	27/10/24	0	0	0.66	0.34	0.57	0.08	0.35	0.9983	1640.98	1.11	
S7	27/10/24	0	0	0.97	0.03	0.42	0.02	0.56	0.9981	865.12	-4.6	
S8	27/10/24	0	0.48	0.05	0.47	0.27	0.06	0.66	0.9996	3205.31	-1.26	
S9	27/10/24	0.12	0	0.52	0.36	0.42	0.01	0.57	0.9988	1899.57	-0.8	
S10	27/10/24	0	0	0.55	0.45	0.35	0.19	0.46	0.9994	2497.08	0.86	
S11	27/10/24	0	0	0.47	0.53	0.46	0.04	0.5	0.9983	3709.63	-1.39	
S12	27/10/24	0	0	0.21	0.79	0.6	0.07	0.33	0.9995	851.51	0.51	
S13	27/10/24	0	0	0.55	0.45	0.5	0.09	0.41	0.9979	2500.17	0.42	

Sample ID	Date	Roofing Material				Urban Morphology				Coastal Proximity (meter)	LST anomaly (°C) All date	LST anomaly (°C) Residuals
		Concrete Fraction	uPVC Fraction	Metal Fraction	Tile/Clay Fraction	BSF	ISF	PSF	SVF			
S14	27/10/24	0	0	0.01	0.99	0.46	0.02	0.52	0.9997	4108.29	-0.17	
S15	27/10/24	0	0	0.51	0.49	0.47	0.11	0.42	0.9993	459.51	-2.43	
S16	27/10/24	0	0	0.58	0.42	0.57	0.14	0.29	0.9986	968.1	0.51	
S17	27/10/24	0	0	0.34	0.66	0.52	0.05	0.44	0.9994	2671.17	0.73	
S18	27/10/24	0	0	0.09	0.91	0.51	0.03	0.46	0.9995	3260.63	0.93	
S19	27/10/24	0	0	0.58	0.42	0.46	0.06	0.47	0.9988	647.69	-0.67	
S20	27/10/24	0	0	0.27	0.73	0.48	0.08	0.44	0.9992	3480.52	0.52	
S21	27/10/24	0	0	0.41	0.59	0.45	0.14	0.41	0.9991	1675.94	0.75	
S22	27/10/24	0.41	0.02	0.26	0.3	0.24	0.11	0.65	0.9987	1749.76	0.04	
S23	27/10/24	0	0	0.67	0.33	0.39	0.1	0.51	0.9979	2662.38	0.3	
S24	27/10/24	0	0	0.19	0.81	0.62	0.03	0.35	0.9992	494.75	0.27	
S25	27/10/24	0	0	0.19	0.81	0.46	0.11	0.44	0.9995	2880.54	0.9	
S26	27/10/24	0	0	0.66	0.34	0.49	0.04	0.47	0.9980	2975.35	-2.05	
S27	27/10/24	0	0	0.1	0.9	0.61	0.03	0.36	0.9995	1648.56	1.67	
S28	27/10/24	0	0	0.31	0.69	0.52	0.07	0.41	0.9994	2978.27	0.88	
S29	27/10/24	0	0	0.34	0.66	0.56	0.03	0.41	0.9990	1329.69	0.79	
S30	27/10/24	0	0	0.51	0.49	0.48	0.07	0.45	0.9976	946.9	0.69	
S31	27/10/24	0	0	0.12	0.88	0.45	0.05	0.5	0.9993	4099.65	0.06	
S32	27/10/24	0	0	0.08	0.92	0.55	0.07	0.38	0.9996	1547.68	0.93	
S33	27/10/24	0	0	0.23	0.77	0.6	0.04	0.37	0.9992	996.73	0.25	
S34	27/10/24	0	0	0.06	0.94	0.46	0.03	0.51	0.9994	4797.44	-0.46	
S35	27/10/24	0	0	0.41	0.59	0.47	0.04	0.48	0.9992	142.44	0.03	
S36	27/10/24	0	0	0.26	0.74	0.58	0.04	0.38	0.9995	726.6	0.02	
S37	27/10/24	0	0	0.11	0.89	0.55	0.07	0.38	0.9996	2705.5	1.54	

Sample ID	Date	Roofing Material				Urban Morphology				Coastal Proximity (meter)	LST anomaly (°C) All date	LST anomaly (°C) Residuals
		Concrete Fraction	uPVC Fraction	Metal Fraction	Tile/Clay Fraction	BSF	ISF	PSF	SVF			
S38	27/10/24	0	0	0.27	0.73	0.57	0.07	0.35	0.9990	1129.26	0.88	
S39	27/10/24	0	0	0.02	0.98	0.49	0.03	0.48	0.9993	4578.38	-0.12	
S40	27/10/24	0	0	0.13	0.87	0.62	0.05	0.34	0.9995	1245.95	1	
S41	27/10/24	0	0	0.29	0.71	0.5	0.04	0.46	0.9986	1980.51	0.27	
S42	27/10/24	0	0	0.39	0.61	0.43	0.08	0.49	0.9993	2407.54	-0.38	
S43	27/10/24	0	0	0.51	0.49	0.36	0.03	0.61	0.9993	2013.37	-1.52	
S44	27/10/24	0	0	0	1	0.44	0.01	0.54	0.9997	3787.43	-0.4	
S45	27/10/24	0	0	0.1	0.9	0.51	0.05	0.44	0.9993	1312.87	0.55	
S46	27/10/24	0	0	0.1	0.9	0.58	0.04	0.38	0.9995	3115.62	0.86	
S47	27/10/24	0	0	0.25	0.75	0.47	0.04	0.49	0.9994	1127.16	-0.19	
S48	27/10/24	0	0	0.85	0.15	0.27	0.02	0.71	0.9992	1393.86	-4.18	
S49	27/10/24	0	0	0.1	0.9	0.58	0.02	0.39	0.9994	2468.73	0.58	
S50	27/10/24	0	0	0.2	0.8	0.42	0.09	0.49	0.9994	2971.81	0.45	

Table D: Accuracy Assessment Results of Land Cover Map Validation

Analysis - Accuracy assessment results																	
Thematic map:	Land cover map																
Response design state:	600/600 samples labeled																
1) Error matrix:																	
		Validation															
		1 (Built up)	2 (Artificial sealed surface)	3 (Rail network)	4 (Waterbodies)	5 (Fish pond with water)	6 (Fish pond without water)	7 (Broadleaved trees)	8 (Herbaceous cover)	9 (Crop without vegetation)	10 (Crop with vegetation)	11 (Swamp)	12 (Bare soil)	Total	User's accuracy	Total class area (m²)	Wi
Thematic map	1	130	0	0	0	0	0	0	0	0	0	0	0	130	1.0	8607441.0	0.21944
	2	0	23	0	0	0	0	1	0	0	0	0	0	24	0.95833	1535689.0	0.03915
	3	0	0	3	0	0	0	0	0	0	0	0	0	3	1.0	171386.25	0.00437
	4	0	0	0	11	1	0	0	0	0	0	0	0	12	0.91667	788894.0	0.02011
	5	0	0	0	0	66	0	0	0	0	0	0	0	66	1.0	4302817.0	0.1097
	6	0	0	0	0	1	24	0	0	0	0	0	0	25	0.96	1637056.0	0.04174
	7	0	0	0	0	0	0	49	1	0	3	0	0	53	0.92453	3436924.0	0.08762
	8	4	3	0	0	0	0	2	166	0	0	0	0	175	0.94857	11415147.75	0.29102
	9	0	0	0	0	0	0	0	0	12	0	0	0	12	1.0	773283.5	0.01971
	10	0	0	0	0	0	0	0	1	0	58	0	2	61	0.95082	3977707.25	0.10141
	11	0	0	0	0	0	0	0	0	0	0	24	0	24	1.0	1565922.5	0.03992
	12	0	0	0	0	0	0	0	0	0	0	0	15	15	1.0	1012308.5	0.02581
	total	134	26	3	11	68	24	52	168	12	61	24	17	600		39224576.75	
	Producer's accuracy	0.97058	0.88264	1.0	1.0	0.97041	1.0	0.94233	0.98813	1.0	0.95108	1.0	0.88587		0.96846		

2b) Accuracy matrix of estimated area proportion:																	
User:																	
		Validation															
		1 (Built up)	2 (Artificial sealed surface)	3 (Rail network)	4 (Waterbodies)	5 (Fish pond with water)	6 (Fish pond without water)	7 (Broadleaved trees)	8 (Herbaceous cover)	9 (Crop without vegetation)	10 (Crop with vegetation)	11 (Swamp)	12 (Bare soil)				
Thematic map	1	1.0	-	-	-	-	-	-	-	-	-	-	-				
	2	-	0.95833	-	-	-	-	0.04167	-	-	-	-	-				
	3	-	-	1.0	-	-	-	-	-	-	-	-	-				
	4	-	-	-	0.91667	0.08333	-	-	-	-	-	-	-				
	5	-	-	-	-	1.0	-	-	-	-	-	-	-				
	6	-	-	-	-	0.04	0.96	-	-	-	-	-	-				
	7	-	-	-	-	-	-	0.92453	0.01887	-	0.0566	-	-				
	8	0.02286	0.01714	-	-	-	-	0.01143	0.94857	-	-	-	-				
	9	-	-	-	-	-	-	-	-	1.0	-	-	-				
	10	-	-	-	-	-	-	-	0.01639	-	0.95082	-	0.03279				
	11	-	-	-	-	-	-	-	-	-	-	1.0	-				
	12	-	-	-	-	-	-	-	-	-	-	-	1.0				

2) Accuracy:		
Overall:		
	Overall Accuracy	Standard deviation
	0.96846	0.00709
User:		
	User's Accuracy	Standard deviation
1 (Built up)	1.0	0.0
2 (Artificial sealed surface)	0.95833	0.04167
3 (Rail network)	1.0	0.0
4 (Waterbodies)	0.91667	0.08333
5 (Fish pond with water)	1.0	0.0
6 (Fish pond without water)	0.96	0.04
7 (Broadleaved trees)	0.92453	0.03663
8 (Herbaceous cover)	0.94857	0.01674
9 (Crop without vegetation)	1.0	0.0
10 (Crop with vegetation)	0.95082	0.02792
11 (Swamp)	1.0	0.0
12 (Bare soil)	1.0	0.0
Producer:		
	Producer's Accuracy	Standard deviation
1 (Built up)	0.97058	0.0141
2 (Artificial sealed surface)	0.88264	0.05659
3 (Rail network)	1.0	0.0
4 (Waterbodies)	1.0	0.0
5 (Fish pond with water)	0.97041	0.02082

6 (Fish pond without water)	1.0	0.0
7 (Broadleaved trees)	0.94233	0.03122
8 (Herbaceous cover)	0.98813	0.00834
9 (Crop without vegetation)	1.0	0.0
10 (Crop with vegetation)	0.95108	0.02648
11 (Swamp)	1.0	0.0
12 (Bare soil)	0.88587	0.06771

2b) Accuracy matrix of estimated area proportion:

Producer:

		Validation												
		1 (Built up)	2 (Artificial sealed surface)	3 (Rail network)	4 (Waterbodies)	5 (Fish pond with water)	6 (Fish pond without water)	7 (Broadleaved trees)	8 (Herbaceous cover)	9 (Crop without vegetation)	10 (Crop with vegetation)	11 (Swamp)	12 (Bare soil)	
Thematic map	1	0.97058	-	-	-	-	-	-	-	-	-	-	-	
	2	-	0.88264	-	-	-	-	0.01898	-	-	-	-	-	
	3	-	-	1.0	-	-	-	-	-	-	-	-	-	
	4	-	-	-	1.0	0.01483	-	-	-	-	-	-	-	
	5	-	-	-	-	0.97041	-	-	-	-	-	-	-	
	6	-	-	-	-	0.01477	1.0	-	-	-	-	-	-	
	7	-	-	-	-	-	-	0.94233	0.00592	-	0.04892	-	-	
	8	0.02942	0.11736	-	-	-	-	0.03869	0.98813	-	-	-	-	
	9	-	-	-	-	-	-	-	-	1.0	-	-	-	
	10	-	-	-	-	-	-	-	0.00595	-	0.95108	-	0.11413	
	11	-	-	-	-	-	-	-	-	-	-	1.0	-	
	12	-	-	-	-	-	-	-	-	-	-	-	0.88587	

3) Error matrix of estimated area proportion:

		Validation												
		1 (Built up)	2 (Artificial sealed surface)	3 (Rail network)	4 (Waterbodies)	5 (Fish pond with water)	6 (Fish pond without water)	7 (Broadleaved trees)	8 (Herbaceous cover)	9 (Crop without vegetation)	10 (Crop with vegetation)	11 (Swamp)	12 (Bare soil)	Wi
Thematic map	1	0.21944	-	-	-	-	-	-	-	-	-	-	-	0.21944
	2	-	0.03752	-	-	-	-	0.00163	-	-	-	-	-	0.03915
	3	-	-	0.00437	-	-	-	-	-	-	-	-	-	0.00437
	4	-	-	-	0.01844	0.00168	-	-	-	-	-	-	-	0.02011
	5	-	-	-	-	0.1097	-	-	-	-	-	-	-	0.1097
	6	-	-	-	-	0.00167	0.04007	-	-	-	-	-	-	0.04174
	7	-	-	-	-	-	-	0.08101	0.00165	-	0.00496	-	-	0.08762
	8	0.00665	0.00499	-	-	-	-	0.00333	0.27605	-	-	-	-	0.29102
	9	-	-	-	-	-	-	-	-	0.01971	-	-	-	0.01971
	10	-	-	-	-	-	-	-	0.00166	-	0.09642	-	0.00332	0.10141
	11	-	-	-	-	-	-	-	-	-	-	0.03992	-	0.03992
	12	-	-	-	-	-	-	-	-	-	-	-	0.02581	0.02581
	total	0.22609	0.04251	0.00437	0.01844	0.11304	0.04007	0.08597	0.27937	0.01971	0.10138	0.03992	0.02913	

4) Quadratic error matrix of estimated area proportion:

		Validation												
		1 (Built up)	2 (Artificial sealed surface)	3 (Rail network)	4 (Waterbodies)	5 (Fish pond with water)	6 (Fish pond without water)	7 (Broadleaved trees)	8 (Herbaceous cover)	9 (Crop without vegetation)	10 (Crop with vegetation)	11 (Swamp)	12 (Bare soil)	
Thematic map	1	-	-	-	-	-	-	-	-	-	-	-	-	
	2	-	0.0	-	-	-	-	0.0	-	-	-	-	-	
	3	-	-	-	-	-	-	-	-	-	-	-	-	
	4	-	-	-	0.0	0.0	-	-	-	-	-	-	-	

	5	-	-	-	-	-	-	-	-	-	-	-	-	
	6	-	-	-	-	0.0	0.0	-	-	-	-	-	-	
	7	-	-	-	-	-	-	1E-05	0.0	-	1E-05	-	-	
	8	1E-05	1E-05	-	-	-	-	1E-05	2E-05	-	-	-	-	
	9	-	-	-	-	-	-	-	-	-	-	-	-	
	10	-	-	-	-	-	-	-	0.0	-	1E-05	-	1E-05	
	11	-	-	-	-	-	-	-	-	-	-	-	-	
	12	-	-	-	-	-	-	-	-	-	-	-	-	
	total	0.0033	0.0033	0.0	0.00168	0.00237	0.00167	0.0043	0.00541	0.0	0.00399	0.0	0.00233	
5) Class area adjusted:														
	Area adjusted (m²)	Error	Lower limit	Upper limit	Coefficient of variation	Uncertainty								
1 (Built up)	8868358.66286	129329.29648	8614873.24176	9121844.08395	1.46 %	0.02858								
2 (Artificial sealed surface)	1667390.20548	129275.87416	1414009.49213	1920770.91883	7.75 %	0.15196								
3 (Rail network)	171386.25	0.0	171386.25	171386.25	0.0 %	0.0								
4 (Waterbodies)	723152.83333	65741.16667	594300.14667	852005.52	9.09 %	0.17818								
5 (Fish pond with water)	4434040.40667	92789.14134	4252173.68965	4615907.12369	2.09 %	0.04102								
6 (Fish pond without water)	1571573.76	65482.24	1443228.5696	1699918.9504	4.17 %	0.08167								
7 (Broadleaved trees)	3371979.38253	168539.64173	3041641.68475	3702317.08031	5.0 %	0.09797								
8 (Herbaceous cover)	10958138.94679	212109.85368	10542403.63357	11373874.26	1.94 %	0.03794								
9 (Crop without vegetation)	773283.5	0.0	773283.5	773283.5	0.0 %	0.0								

10 (Crop with vegetation)	3976625.1712	156402.00218	3670077.24693	4283173.09548	3.93 %	0.07709								
11 (Swamp)	1565922.5	0.0	1565922.5	1565922.5	0.0 %	0.0								
12 (Bare soil)	1142725.13115	91446.7679	963489.46606	1321960.79623	8.0 %	0.15685								
total	39224576.75													

Table E: Accuracy Assessment Results of Roofing Material Map Validation

Analysis - Accuracy assessment results									
Thematic map:	Roof Material Type Raster								
Response design state:	200/200 samples labeled								
1) Error matrix:									
		Validation							
		1 (Concrete)	2 (Metal)	3 (Tile/Clay)	4 (Unplasticized Polyvinyl Chloride (uPVC))	Total	User's accuracy	Total class area (m^2)	Wi
Thematic map	1	3	0	0	0	3	1.0	21376.75	0.00248
	2	0	27	6	0	33	0.81818	1472344.0	0.17106
	3	0	5	156	0	161	0.96894	7065710.75	0.82092
	4	0	0	0	3	3	1.0	47656.5	0.00554
	total	3	32	162	3	200		8607088.0	

	Producer's accuracy	1.0	0.84591	0.96237	1.0		0.9434		
2) Accuracy:									
Overall:									
	Overall Accuracy	Standard deviation							
	0.9434	0.01621							
User:									
	User's Accuracy	Standard deviation							
1 (Concrete)	1.0	0.0							
2 (Metal)	0.81818	0.06818							
3 (Tile/Clay)	0.96894	0.01371							
4 (Unplasticized Polyvinyl Chloride (uPVC))	1.0	0.0							
Producer:									
	Producer's Accuracy	Standard deviation							
1 (Concrete)	1.0	0.0							
2 (Metal)	0.84591	0.0548							
3 (Tile/Clay)	0.96237	0.01474							
4 (Unplasticized Polyvinyl Chloride (uPVC))	1.0	0.0							
2b) Accuracy matrix of estimated area proportion:									
User:									

		Validation							
		1 (Concrete)	2 (Metal)	3 (Tile/Clay)	4 (Unplasticized Polyvinyl Chloride (uPVC))				
Thematic map	1	1.0	-	-	-				
	2	-	0.81818	0.18182	-				
	3	-	0.03106	0.96894	-				
	4	-	-	-	1.0				
Producer:									
		Validation							
		1 (Concrete)	2 (Metal)	3 (Tile/Clay)	4 (Unplasticized Polyvinyl Chloride (uPVC))				
Thematic map	1	1.0	-	-	-				
	2	-	0.84591	0.03763	-				
	3	-	0.15409	0.96237	-				
	4	-	-	-	1.0				
3) Error matrix of estimated area proportion:									
		Validation							
		1 (Concrete)	2 (Metal)	3 (Tile/Clay)	4 (Unplasticized Polyvinyl Chloride (uPVC))	Wi			
Thematic map	1	0.00248	-	-	-	0.00248			
	2	-	0.13996	0.0311	-	0.17106			
	3	-	0.02549	0.79542	-	0.82092			
	4	-	-	-	0.00554	0.00554			
	total	0.00248	0.16545	0.82653	0.00554				

4) Quadratic error matrix of estimated area proportion:									
		Validation							
		1 (Concrete)	2 (Metal)	3 (Tile/Clay)	4 (Unplasticized Polyvinyl Chloride (uPVC))				
Thematic map	1	-	-	-	-				
	2	-	0.00014	0.00014	-				
	3	-	0.00013	0.00013	-				
	4	-	-	-	-				
	total	0.0	0.01621	0.01621	0.0				
5) Class area adjusted:									
	Area adjusted (m^2)	Error	Lower limit	Upper limit	Coefficient of variation	Uncertainty			
1 (Concrete)	21376.75	0.0	21376.75	21376.75	0.0 %	0.0			
2 (Metal)	1424077.10178	139523.824	1150610.40674	1697543.79682	9.8 %	0.19203			
3 (Tile/Clay)	7113977.64822	139523.824	6840510.95318	7387444.34326	1.96 %	0.03844			
4 (Unplasticized Polyvinyl Chloride (uPVC))	47656.5	0.0	47656.5	47656.5	0.0 %	0.0			
total	8607088.0								

Impact Assessment of Land Cover, Urban Morphology, and Roofing Materials on Surface Urban Heat Island Estimation Using Multi-Temporal Landsat Imagery in Tegal City, Indonesia by Azrina Farania

Abstract

This study evaluated the influence of land cover composition, Local Climate Zone (LCZ), and roofing material properties on the spatial distribution of land surface temperature and surface urban heat island (SUHI) pattern in a tropical coastal city. The research was conducted in Tegal City, Indonesia, using multi-temporal Landsat 8/9 thermal imagery across six heatwave dates (September 2023 to October 2024). The PSF convolution approach was used to homogenize land cover and LCZ composition at the pixel level by aligning them with the thermal resolution of the Landsat thermal sensors prior to regression modeling.

Urban surfaces were derived from Tegal City Government's land cover data (0.5m resolution) updated with Sentinel-2 spectral indices. Morphological analysis was performed by classifying land cover into LCZs based on form (e.g., compact, open, or vegetation) using rules, and by classifying urban surfaces based on their thermal characteristics using a Normalized Brightness Index approach. Land cover and LCZ-based models were constructed using linear regression and linear mixed-effect modeling, and the thermal effects of each surface class were determined and compared.

The land cover model achieved higher predictive performance (R^2 = 0.84, RMSE = 1.3459 °C) than the LCZ model (R^2 = 0.79, RMSE = 1.5309 °C), suggesting that fine-resolution land cover composition captures thermal variability more precisely than urban morphological classification alone. In land cover models, strong warming effects were observed from railway networks (+10.63 °C) and built-up area (+8.75 °C). Broadleaved trees (-7.11 °C) and fish ponds with water (-6.05 °C) yielded significant cooling. For LCZ models, stronger warming was recorded from urban LCZ 2-Compact medium-rise (+11.32 °C) and LCZ E-Bare rock or paved (+4.76 °C), with LCZ A-Dense trees (-8.10 °C) and LCZ G-Water (-5.58 °C) as the strongest coolers. Among urban morphological parameters, Pervious Surface Fraction (PvSF) showed the strongest correlation with LST anomaly (r = -0.647). Roofing material analysis revealed that tile/clay roofing was associated with higher LST anomalies, while metal roofing showed a cooling effect. A statistically significant but weak coastal cooling gradient was identified to have a negative correlation. Based on findings, practical recommendations can be provided for urban mitigation: to invest in cool roofing and minimum vegetation, limit building densities, and protect coastal areas. The methodology employed can also be used in other tropical coastal cities for heat-resilient urban planning.

Keywords: Surface Urban Heat Island, Land Surface Temperature, Local Climate Zones, Landsat, Urban Morphology, Tropical Cities

UNIVERSITÉ CATHOLIQUE DE LOUVAIN
Faculté des bioingénieurs
Croix du Sud, 2 bte L7.05.01, 1348 Louvain-la-Neuve, Belgique | **www.uclouvain.be/agro**